Interfacial Interaction Study of Proteins and Pollutants onto Inorganic Surfaces

A Dissertation Submitted in Partial Fulfillment for the Degree of

Doctor of Philosophy

by

Jiban Saikia

(Roll No. 09612220)

Department of Chemistry

Indian Institute of Technology Guwahati

March – 2014

Interfacial Interaction Study of Proteins and Pollutants onto Inorganic Surfaces

A Dissertation Submitted for Partial Fulfillment for the Degree of

Doctor of Philosophy

by

Jiban Saikia

(Roll No. 09612220)

Department of Chemistry

Indian Institute of Technology Guwahati

March – 2014

Dedicated to my Parents

INDIAN INSTITUTE OF TECHNOLOGY GUWAHATI

Department of Chemistry

STATEMENT

I do hereby declare that the matter embodied in this thesis is the result of investigations carried out by me in the Department of Chemistry, Indian Institute of Technology Guwahati, India, under the guidance of Dr. Gopal Das, Professor (Department of Chemistry), Indian Institute of Technology Guwahati, India.

In keeping with the general practice of reporting scientific observations, due acknowledgements have been made wherever this work is based on the findings of other investigators.

March, 2014 (**Jiban Saikia**)

IIT Guwahati

INDIAN INSTITUTE OF TECHNOLOGY GUWAHATI

Department of Chemistry

CERTIFICATE

This is to certify that Jiban Saikia has been working under my supervision since July, 2009 as a regular registered Ph. D. student. His thesis entitled **"Interfacial Interaction Study of Proteins and Pollutants onto Inorganic Surfaces"** is an authentic record of the results obtained from the research work carried out under my supervision in the Department of Chemistry, Indian Institute of Technology Guwahati, Assam, India. I am forwarding his thesis to submit for the award of degree of Doctor of Philosophy, from this institute. I certify that he has fulfilled all the requirements according to the rules of this institute regarding the investigations embodied in his thesis and this work has not been submitted elsewhere for a degree.

Dr. Gopal Das
(Thesis Supervisor)
Professor
Department of Chemistry
IIT Guwahati
Assam - 781 039, India

Acknowledgement

At the very onset, I would like to express my gratitude to my parents and family members. Their unconditional love and support made me reach this stage of my life. I also express my sincere gratitude towards my PhD supervisor, Dr. Gopal Das. His constant motivation and encouragement, his knowledge and personal guidance gave me the liberty to explore the domain of my work assembled in this thesis. His easy going nature inspired me a lot to do better and also encouraged to maintain a resourceful environment in the lab.

Besides my supervisor, I would also like to extend my heartiest thanks to the doctoral committee members, Dr. Manabendra Ray, Dr. Debasis Manna, Dr. Lal Mohan Kundu, for their periodic appraisal of my work and valuable suggestion. I also wish to thank other faculty members and staff members of chemistry department for their positive guidance. I would also thank Dr. BLD for the help he has rendered through these years. My sincere thanks to the Central Instruments facility, IIT Guwahati and to Chandan Borgohain, K. Senapati, M. Borah of Central Instruments facility, IIT Guwahati for their help and in hand guidance to several analytical instruments, required during my research work.

Alongside I would always be thankful to the wonderful lab-mates I have come across. Starting from the senior most Ballav da, Avijit da, Harajyoti da, Bimlu da, Sandeep da, Arghya, to Chiru, Md Najbull, Romen, Abhijit, Barun, Soham, Nilotpal. Without the frequent brainstorming tea breaks from the 'hectic' research work and 'relaxing' weekly parties with these people, it would never be possible for me to finish. I shall always be obliged to Dr. Bedabrata Saha for his unconditional continuous support and showing me the 'art of living' at hard times.

I also owe my obligations to my other seniors, batch mate and juniors of PhD fraternity of chemistry department for their help and support.

In context to the thesis work, I had the opportunity to mingle with the seniors and friends of the Center for Environment, IIT Guwahati. I owe my gratitude to Suresh da, Atreyi di, Naresh da, Aditi di, Anand da, Biju di, Bharti, Sushant, Bhaskar, Samarpita for their unconditional support and all the help they extended from time to time whenever required.

I take this opportunity to thank my friend Hiruj, Bore, Jadu, Santanu, Subrata, Dipunk, Dipen, Jon, Manoj, Pargu for being a source of encouragement and love throughout this time. I would also like to thank all M. Sc and B. Tech batches here in IIT Guwahati, and hostel mates,

Fesa, Kuntal, Rohitas, Manjeet, Viswa, Rohit da, I came across in these years. Also a big thanks to Sushil da for countless cups of tea he have supplied which helped a lot in fulfilling this thesis.

Hearty thanks to Sukanya, to bear with me for so long throughout this phase even in frustrating times, and for all the fun and fight I shared with her. I would also like offer my thanks to Dhan, Dhruba, Rupam, Popy, Subham and Gungun for their untiring smile and love for me throughout this phase.

Finally, no words would suffice to express my feelings for my teachers to whom I owe debt for their kindness and benevolence. Music sir and Art sir from my school whose love and support have so luxuriously continued to enrich my life. Manjit sir, Pannalal sir, Ganguly mam, SKB sir, PJD sir, many others from my college and university who gave me the direction and insightful informations to march forward in this field.

Still many names are missing whose contribution and help is worth mentioning.

Jiban

SYNOPSIS

The contents of this thesis entitled **"Interfacial interaction study of proteins and pollutants onto inorganic surfaces"** have been divided into six chapters based on the results of experimental work performed during the research period.

Chapter 1 comprises the significant properties of solid-liquid interface and it importance in interaction studies with an emphasis on protein and pollutant interaction. The solid liquid interafce has been a hotspot for innumerable physical, chemical and biological processes and has been studied extensively in last few decades due to emerging technical applications such as in remediation technologies, biotechnology, material sciences, nanotechnology etc. When constituents of the solid-liquid interface come in contact they tend to interact with one another. Liquid tends to accumulate on the solid surface due to attractive forces acting between them. This accumulation of liquid over the solid surface, which is the basis of most surface-chemical processes, is termed as "adsorption". The chemical and structural constitutions of solid phase surfaces highly govern the fate of phenomena occurring at solid-liquid interfaces. Different surfaces behave differently when introduced with different species in solution. Control over such interaction could be achieved by choosing the specific surface for specific interaction. This chapter gives an overview of such controlled interactions of different proteins and pollutants on specific inorganic surfaces. A detail insight into the protein-surface interaction would benefit nano-scale materials and bio-nano-assembly technologies. Moreover, the structure-function relationship of proteins and pollutants interaction with inorganic surfaces would cater some information about the mechanism of the system on the basis of which similar system can be constructed for better practical usability. This chapter also summarizes the importance of the specific surface properties on controlled interaction of proteins and pollutants. A thorough review of the contribution of important physicochemical phenomena of such surfaces in combination with the molecular and structural knowledge of such solid surface interface has been elaborated in this chapter.

Chapter 2 deals with the methodology followed to synthesize and characterize different inorganic surfaces. It also describes the general equipment and different experimental

setup used to study the interaction of different proteins and pollutants on various inorganic surfaces.

Chapter 3 describes the interaction study of protein with a basic 'hard' surface (according to Pearson's Hard-Soft Acid Base principle). ZnO nanoparticles (NPs) of different morphology have been synthesized from single precursor source and its interaction study with *β*-lactoglobulin has been presented in this chapter. In brief, control over the synthesis of morphologically different ZnO NPs, using same precursor aromatic organic acid as ligand for Zn^{2+} coordination, has been reported in this study. *2*, *3*-pyridinedicarboxylic acid (PDC) was used as a ligand to form Zn(II)-PDC precursor complexes of different architectures, which on further calcination at 600^{o}C produce ZnO NPs of different morphology. The monomer Zn(II)-PDC complex leads to disk-like ZnO NPs of ~30nm diameter; whereas the co-ordination polymer of Zn(II)-PDC when heated predominantly produce ZnO nano-rod of length ~100nm. These structurally different ZnO NPs were then characterized successively using PXRD, FTIR, UV, PL, BET, zeta (ζ) potential and TEM. Then we have investigated the bio-interaction of these ZnO NPs with *β*-lactoglobulin (BLG) adsorption study. Interestingly, these two morphologically different nanostructures (disk-like ZnO NPs and ZnO nano-rods) gave differential adsorption value with BLG. The probable reason behind this incongruity may lie in the difference of their BET surface area. As revealed from the BET surface area analysis, the surface area of the disk-like ZnO NPs (20.25 m^2/g) was much larger than the ZnO nanorods (6.60 m^2/g). The adsorption values with the ZnO nanorods were quite insignificant compared to the disk-like ZnO NPs, so we have further proceeded with the in-depth experiments with disk-like ZnO NPs only. The thorough analysis of the adsorption process has been performed by varying the factors such as protein and NP concentration, temperature, time, and pH. The protein interaction process was found to be pH dependent. The adsorption kinetics data was well fitted with the second order kinetics and the negative (ΔG^{o}) values of adsorption process reflect the thermodynamic favorability of the process. Moreover, in-depth structural analysis of the protein interacting with ZnO NPs has been done using spectroscopic techniques. Fluorescence emission and anisotropy analysis reveals a partial loss in tertiary structure of BLG upon binding on surface. However, the circular dichroism spectra show no significant change in the secondary component upon

adsorption. This indicates that the BLG is almost stabilized on ZnO NPs surface upon adsorption.

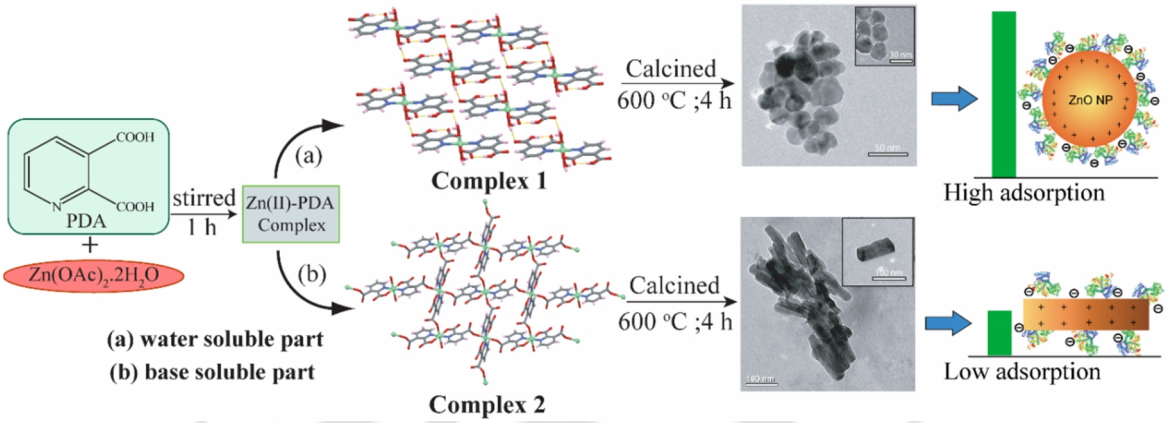

Figure S1. A comprehensive representation of the research work included in chapter 3.

Chapter 4 progresses towards the study of another inrganic surface for the interaction study. After the interaction study of a basic 'hard' surface in the previous chapter, this chapter deals with the interaction of proteins with an acidic 'soft' surface. It details the synthesis of ZnS nanoparticles from the Zn(II)-PDC complex and interaction study with two different proteins. The Zn(II)-complex was made soluble adding few drops of base, then H_2S gas was purged to give the white precipitates of ZnS NPs which were further characterized and used for the adsorption interaction study. The ZnS NPs were found to be spherical in sizes of ~100 nm from TEM analysis. Then we have undertaken the work to investigate the adsorption behavior of bovine serum albumin (BSA) and *β*-lactoglobulin (BLG) having near same IEP and differing in their conformational flexibility, onto the surface of ZnS NPs. BSA and BLG both have an IEP value around pH ~ 5. BSA is more prone to conformational deformation and considered "soft" while BLG holds the conformational rigidity and considered as "hard" protein. To ascertain the differences in surface coverage and conformation of the protein onto ZnS surface (PZC ~ 3.7), we have evaluated the adsorption profile at pH 7, where the entire surface behaves negatively. An integrated approach was taken by incorporating zeta (ζ) potential, fluorescence and CD for analyzing the adsorption process. In both systems, an increase in protein surface coverage was observed with the increase in free protein concentration in the solution and ζ values approaching that of native protein at high surface coverage. An alteration in the tertiary structure was observed for both BSA and

BLG. The CD spectra analysis reveals that the secondary structure of the BSA was more deviated from the native protein structure, accommodating the increased adsorption value. For BLG no such prominent structural alteration was observed. These findings help us to understand better, how adjustment of the protein adsorption amount can be achieved onto the surface of nanoparticles having like charges.

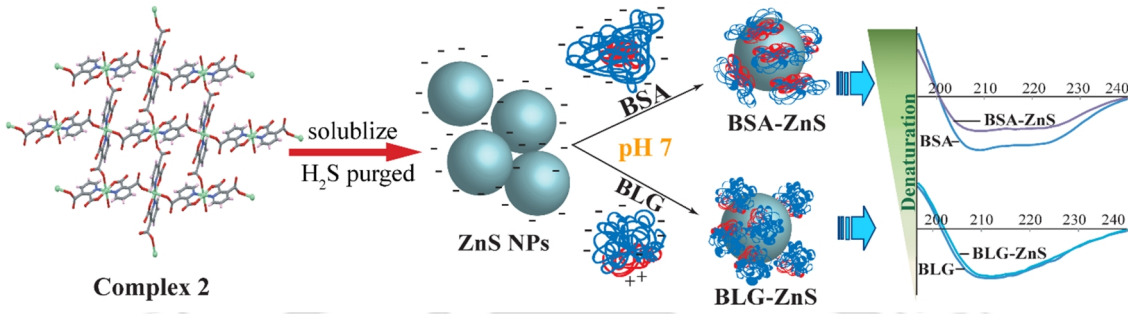

Figure S2. A comprehensive representation of the research work included in chapter 4.

Chapter 5. After studying the effect of 'hard' and 'soft' surfaces on protein interaction behavior this chapter advances to study the interaction of another 'basic' and 'hard' inorganic mineral surface with pollutants. Malachite or basic copper carbonate is a naturally occurring secondary copper mineral with the composition of $Cu_2(OH)_2CO_3$ has been used for the cause. Malachite NPs have been synthesized and utilized for the removal of pollutants from aqueous system. This chapter is further divided into two parts.

Part I deals with the removal of some inorganic pollutants using the Malachite NPs. Inorganic pollutants such as arsenate and chromate were used as model for the study. Malachite nanoparticles of 100-150 nm have been efficiently and for the first time used as an adsorbent for the removal of toxic arsenate and chromate. We report a high adsorption capacity for chromate and arsenate on malachite nanoparticle from both individual and mixed solution in pH ~4-5. However, the adsorption efficiency decreases with the increase of solution pH. Batch studies revealed that initial pH, temperature, malachite dose and initial concentration of chromate and arsenate were important parameters for the adsorption process. Thermodynamic analysis showed that adsorption of chromate and arsenate on malachite nanoparticles is endothermic and spontaneous. The adsorption of these anions has also been investigated quantitatively with the help of

adsorption kinetics, isotherm, and selectivity coefficient (k) analysis. The adsorption data for both chromate and arsenate were fitted well in Langmuir isotherm and preferentially followed the second order kinetics.

Part II describes the potential applicability of Malachite NPs for removal of organic pollutants. The ability of the Malachite NPs for differential adsorption of dyes (organic pollutants) with differential functionality was explored. Three different dyes viz: Fluorescein (with –COOH and–OH), Rhodamine B (with –COOH) and Rhodamine 6G each having same xanthene moiety but differing in their functionality was taken for the study. Fluorescein was found to adsorb more followed by Rhodamine B and Rhodamine 6G at pH ~ 7. Electrostatic interaction was sought to play a major role in the adsorption process. Batch studies were conducted to evaluate the effects of regulating parameters such as contact time, temperature, adsorbent dosage, and solution pH on the adsorption process. Experimental results showed that a steady state was achieved at ~ 6 hrs after which the adsorption seemed constant for all the three dyes. Temperature range of 10 ºC to 40 ºC was taken for the study and the adsorption was found to increase with the increase in temperature. The concentration of dye was varied from 10-500 mg L^{-1} and the maximum adsorption was obtained for Flu with q_e value ~29.54 (mg g^{-1}) followed by RB qe value ~20.74 (mg g^{-1}). R6G was least adsorbed with q_e value ~6.4 (mg g^{-1}).The experimental data were plotted using the Langmuir and Freundlich isotherm and found to follow the Langmuir isotherm preferably. The adsorption followed the second order kinetics. Furthermore effective desorption was carried out using 50% ethanol. Flu was desorbed to ~99.5% whereas complete extraction of RB and R6G were obtained. The muticycle efficiency was also investigated. Overall, the work detailed in this part substantiates the possible use of Malachite nanoparticles (NPs) as an effective adsorbent for removal of dyes from aqueous solution.

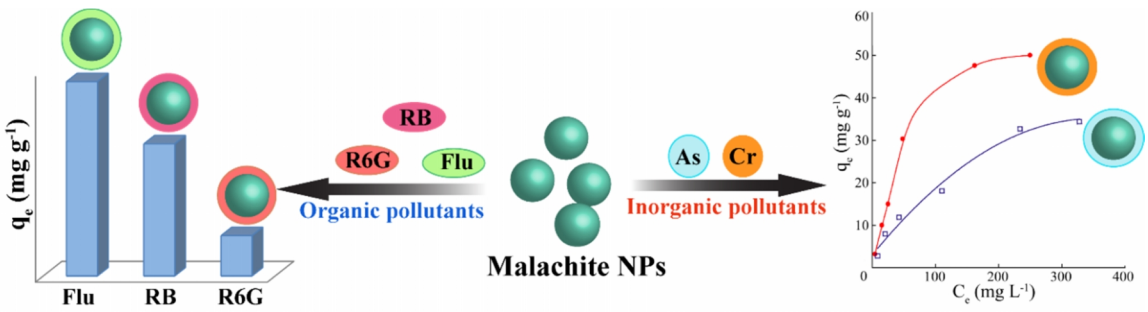

Figure S3. A comprehensive representation of the research work included in chapter 5.

Chapter 6 also elaborates the use of another basic 'hard' potential inorganic surface for pollutant removal from aqueous solution which is bio-compatible in nature. Vaterite, a polymorph of $CaCO_3$ mineral has been explored in this regard. Framboidal vaterite micro-particles were successfully synthesized and characterized accordingly. These particles were then subjected to the removal of organic/inorganic pollutants. This chapter is also divided into two parts.

Part I indicates the possible use of framboidal vaterite microspheres for anionic inorganic pollutant removal from aqueous medium. Another inorganic surface has been explored in this regard and was found to be effective in removing arsenate and chromate from aqueous solution. The adsorption phenomenon was governed by the pH of the medium. The adsorption was higher at pH 6-7, for both arsenate and chromate. The adsorption capacity increases with the increase in initial pollutant concentration. The kinetic of the adsorption followed the pseudo-second –order model. A good agreement between Langmuir isotherm and experimental data suggest monolayer coverage of arsenate and chromate upon adsorption onto the vaterite surface. The maximum adsorption capacity (Q_m) was calculated to be 154.1 and 156.3 mg g−1 for arsenate and chromate respectively. The pollutant adsorption has been found to be thermodynamically favorable. Desorption was efficiency was found to be moderately good.

Part II also reflects the potential applicability of vaterite microspheres in the removal of some organic pollutants (dyes) from aqueous solution. Vaterite, a relatively unstable polymorph of $CaCO_3$ and having high surface area was found to be efficient container for the loading of anionic dyes compared to the cationic dyes. EBT, CR was adsorbed more compared to the cationic dyes such as MB and R6G. The adsorption profile was highly pH dependent and was sought to be electrostatic in nature. The positive surface of the vaterite ($pH < PZC_{vaterite}$) and the negative functional groups of the EBT and CR ($pH > pK_a$) facilitates the requisite electrostatic interaction that leads to the increased adsorption of these dyes onto vaterite surface. Whereas the electrostatic repulsion of the cationic MB and R6G ($pH < pK_a$) with the positive ($pH < PZC_{vaterite}$) surface justifies the observed lower value of adsorption onto vaterite surface. The adsorption followed the second order kinetics for all the dyes with simultaneous occurrence of the intra particle diffusion of the dyes. Langmuir isotherm was preferably more matched with the obtained data for all the cases of the dye. The adsorption was spontaneous in nature. The desorption efficiency and the practical reusability of the vaterite-dye composite was

addressed efficiently. These findings together suggest the potential applicability of vaterite for waste water treatment.

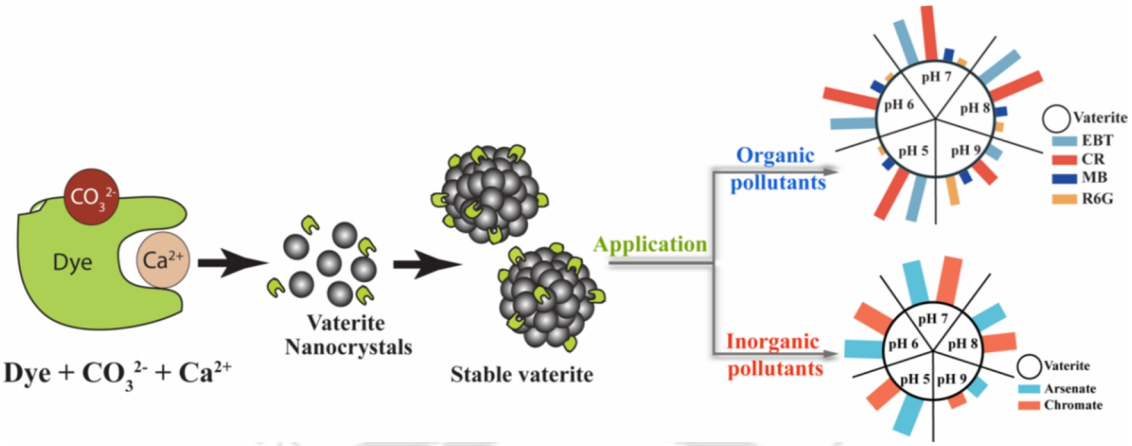

Figure S4. A comprehensive representation of the research work included in chapter 6.

At the end of the thesis an overall conclusion of the research carried out during the research period is presented and a discussion for the scope of future and further research in the area of interaction of proteins and environmental pollutants at different solid-liquid interfaces is provided.

Contents

Chapter 5 – Malachit-Protein interaction

Chapter 1

Introduction

Chapter 1

1.1 Interface

The surface forming a common boundary between two phases is defined as "*interface*". The interface has been a hotspot for innumerable physical, chemical and biological processes. Depending on the type of phases we can further classify these interfaces into liquid-gas, liquid-liquid, solid-gas and solid-liquid. Amongst these, the solid-liquid interface has been studied extensively in last few decades due to emerging technical applications such as in remediation technologies, biotechnology, material sciences, nanotechnology etc.[1.1] The chemical and structural constitutions of solid phase surfaces highly govern the fate of different phenomena occurring at solid-liquid interfaces.

1.2 Interfacial interaction and adsorption

When constituents of the solid-liquid interface come in contact they tend to interact with one another. Liquid tends to accumulate on the solid surface due to attractive forces acting between them. This accumulation of liquid over the solid surface, which is the basis of most surface-chemical processes, is termed as "adsorption". Adsorption is a consequence of the surface energy. The molecules poses high surface energy at the interface compared to its bulk phase as the overall forces are not balanced at the interface. This unbalanced force component at the interface is accountable for adsorption process.

From the theoretical point of view, adsorption of molecules onto a surface is just a special case of general two particles interaction, whereas in real circumstances it is a very intricate process. This process is conceptually divided into several steps. In the first step the molecules in the liquid phase are transported close to the solid surface either by convective flow, diffusion or by help of external forces like gravity. The second step is the interaction with surface forces acting over different ranges. The interaction can lead to the deposition of these molecules on the solid surface, while some can detach back to the bulk solution, or they can interact among themselves and aggregate. The adsorption can also further lead to the restructuring of adsorbed molecular entity.[1.2]

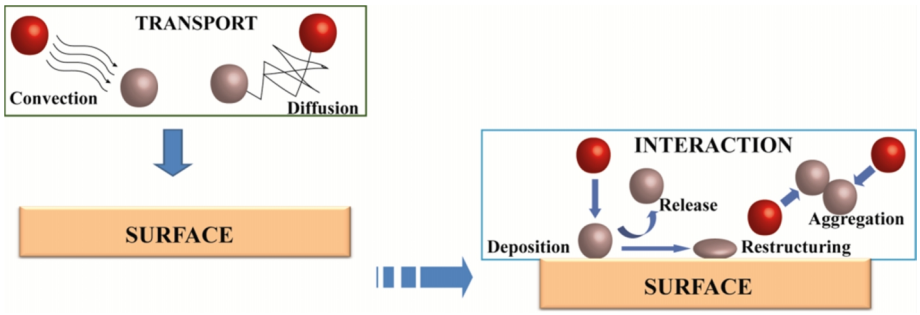

Figure 1.1. Schematic illustration of the fate of colloidal particles and processes taking place at a solid-liquid interface. (Adopted from reference 1.2)

1.3 Different forces and physico-chemical parameters influencing adsorption process

Molecules interact with surfaces involves forces originating either from the "physical" Van der Waals interaction or from the "chemical" hybridization of their orbitals with those of the atoms of the substrate. The one which originates from the involvement of the weaker interaction such as Van der Waals interaction is termed as physisorption. The other types of interaction arises due to the formation of chemical bonds between the surface and the interacting molecules and termed as chemisorption.[1.3,1.4] Adsorption mechanisms represent probably the most important interaction phenomena exerted by solid surfaces at a solid-liquid interface.[1.5] The physico-chemical nature of the solute, the sorbent and the solvent governs the full understanding of the adsorption process.[1.6] There are several factors which affects the adsorption mechanism at solid-liquid interface which includes –

- Interfacial tension – of solute molecules at solid-liquid interface
- pH of the system
- Temperature of the system
- Colloidal stability at interface and solute concentration
- Functional groups of the adsorbate and adsorbent interacting with each other

We can get further information of the adsorption process of any molecules on solid surfaces by studying the adsorption kinetics, thermodynamics and adsorption equilibrium which can be analyzed by controlling the parameters such as adsorption time, temperature and concentration of the analyte molecules and available surface area respectively.

1.4 Surfaces for adsorption

Surface interaction leads to adsorption and therefore it is fundamentally important for a good adsorbent to poses high porosity and larger surface area.[1.7] Innumerable solid

surfaces are widely used for the adsorption of various molecules from the solution. Different solids have different surface properties which in turn show different adsorption behavior. Adsorption interaction of molecules, inorganic ions, metals etc. and biomolecules like proteins, DNA etc. has been extensively studied on various adsorbent ranging from large mica surface to very small the nano-structured material. Amongst all the surfaces practiced, the properties of the inorganic micro-nano particles have been able to form a niche in various potential applications. The micro-nano structured materials are a major tool in controlled/selective adsorption of different molecules. Throughout the past decade, there has been increasing interest in using nanotechnology to solve problems in several emerging fields likely, environmental remediation, drug delivery, medicine, sensor designing etc.[1.8] Ease of synthesis with potential robustness, and variable physiochemical surface properties make these inorganic materials a suitable choice for adsorption interaction studies with different molecules.

1.5 Inorganic surfaces for adsorption

1.5.1. Adsorption of proteins on inorganic solid surfaces

Protein adsorption on a surface and its interaction are major concerns in a number of fields, such as biology, medicine, biotechnology, and food processing and sometimes play an important role in a system's performance. [1.9] Therefore, it is very crucial to get an in-depth understanding of the protein adsorption process on solid surfaces. As known from literature, protein adsorption is a complex process involving Van der Waals, hydrophobic and electrostatic interactions, and hydrogen bonding.[1.10] A lot of factors together play the role in controlling protein adsorption. Some of the external parameters such as temperature, pH, ionic strength, and buffer composition have a prominent role in the adsorption process. The equilibrium state and the kinetics of protein adsorption are dependent in the temperature of the medium. The pH determines the electrostatic state of the protein which in turn determines the electrostatic interaction with the solid surface. The size, composition and structural stability of proteins regulate its interfacial adsorption to a great extent. Structural reorientation (both secondary and tertiary) is accompanied by the adsorption for most of the protein whilst some appears to resist significant conformational change.[1.11] This sort of conformational flexibility and conformation rigidity of proteins classified them into class of “soft” and “hard” proteins. Proteins that have a tendency to undergo major surface-induced conformational change are termed as “soft” and those less vulnerable to conformational change are coined as “hard” protein.[1.12]

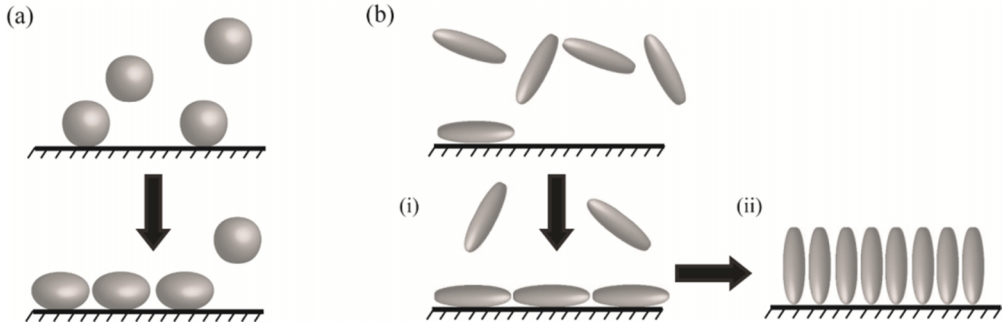

Figure 1.2. An illustration showing adsorption of (a) a globular protein (e.g. BSA) whose conformation may become distorted on interaction with the surface and (b) a rod-like protein that undergoes a multistage adsorption process where (i) initially the protein adsorbs with its long axis parallel to the surface and then (ii) rearrangement occurs to increase protein-protein interaction and surface concentration of protein.(Adopted from reference 1.13)

A lot of work has been reported in the literature for the use of inorganic surfaces for adsorption and interaction of proteins. For *e.g.* Rezwan *et al*. demonstrated the adsorption of bovine serum albumin (BSA) onto colloidal Al_2O_3 particles. [1.14] They have observed that BSA adsorbs on aluminium oxide surface as a monolayer by using 30-36% of its total negative charge favoring the electrostatic interaction and that additional BSA molecules from the medium bind onto this monolayer as dimers.

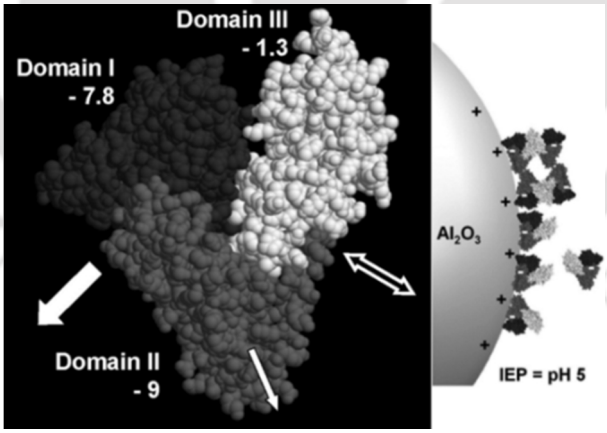

Figure 1.3. (right) The three domains of BSA including the calculated net charges present at pH 7. The double head arrow indicates the dimer forming region, the broad arrow *side on* and thin arrow *end on* forming region. (left) Adsorption of BSA onto alumina surface by *side-on* adsorption mode and subsequent dimer formation. (Adopted from reference 1.14)

Bardhan *et al*. have studied the interaction of BSA with ZnO NPs where the spectroscopic investigation of zinc oxide (ZnO-NP) interaction with BSA showed no significant perturbation to its overall structure, however, minor conformational change was

reported.[1.15] Similarly, an irreversible conformational change in the secondary structure of the protein transferrin was observed upon interaction with super magnetic iron oxide nanoparticles.[1.16] Shang *et al.* detailed the unfolding of ribonuclease A on silica nanoparticle surfaces and showed in details how the size and curvature of nanoparticle can alter the conformation of proteins upon adsorption.[1.17] Recently, Turci *et al.* have investigated the adsorption of four proteins BSA, lysozyme, ribonuclease A and lacto-peroxidase, characterized by different net charge or charge density at physiological pH and different resistance to deformation onto two different SiO_2 (having different silanol density) surfaces.[1.18] Structure and activity of lysozyme on binding to ZnO NPs was elaborated by Chakraborti et al. who showed that lysozyme, when bound to ZnO NPs of 7 nm diameter at pH 7.4, takes on a more regular structure in comparison to its free form.[1.19] A similar study on surface topography and curvature depended adsorption of two proteins serum albumin and fibrinogen (differing in size and shape) on different sized hydrophilic and hydrophobic silica nanoparticles was later illustrated by Roach et al. They reported that, albumin is increasingly less ordered on larger particles, while fibrinogen, in contrast, loses secondary structure to a greater extent when adsorbing onto smaller particles (high surface curvature).[1.20] Kandori *et al.* have done micro calorimetric study of protein adsorption onto calcium hydroxyapatites [$Ca_{10}(PO_4)_6(OH)_2$]. They have considered three proteins of different IEP namely BSA (~5), myoglobin (~7) and lysozyme (~11) and found that BSA showed the highest adsorption value on calcium hydroxyapatites surfaces.[1.21] Another example of surface dependent adsorption was carried out by Gauckler *et al*. They have done a systematic investigation of the protein adsorption on various ceramic particles with a special focus on the influence of the particle surface charge and the adsorbed amount of proteins. Positively charged lysozyme (LSZ) and negatively charged bovine serum albumin (BSA) were adsorbed to alumina, silica, titania, and zirconia colloidal particles with diameters ranging from 73 to 271 nm. The electrostatic interaction seems to govern protein adsorption for the cases where the protein and the materials surfaces are very hydrophilic (alumina, silica, and titania). For for slightly less hydrophilic (zirconia) material surface, hydrophobic interaction seems to play an important role in the adsorption process as well and can even overcome electrostatic repulsion.[1.22] Patch-controlled electrostatic attraction of Cry1Ab protein onto negatively charged quartz (SiO_2) and positively charged poly-L-lysine (PLL) was investigated by Madliger *et al*.[1.23] Cry1Ab was found to be adsorbed via positively and negatively charged surface patches to quartz (SiO_2) and PLL, respectively. This patch

controlled electrostatic attraction explains the observed increase in Cry1Ab adsorption to sorbents that carried the same net charge as the protein.

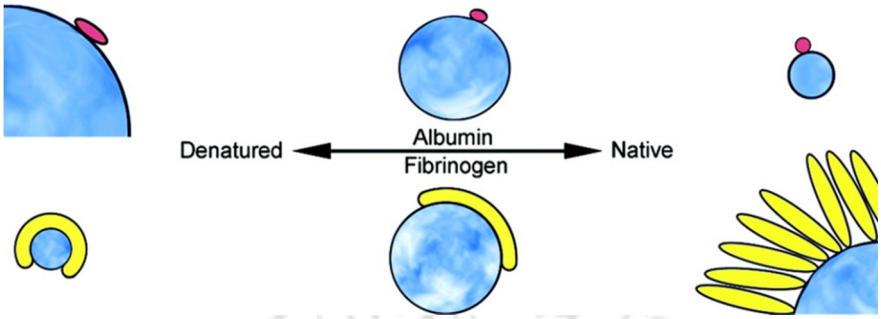

Figure 1.4. Schematic representation of the control of surface curvature over the conormation and orientation of proteins. (Adopted from reference 1.19)

These above mentioned examples indicate the broad applicability of inorganic surfaces for adsorption interaction of proteins. It also signifies how the physiochemical properties, morphological differences of the surfaces and the protein properties govern the adsorption phenomena.

1.5.2. Adsorption of pollutants (Organic and Inorganic) on inorganic solid surfaces

Various anthropogenic factors have led to a serious depletion of the environment. Different pollutants are being constantly added to the atmosphere leading serious health issues. Among the various types of pollution, water pollution has attracted the attention of various researchers and scientists around the world. The removal of pollutants from water bodies has become the need of the hour. Heavy metals, dyes, phenols (including other organic compounds), inorganic anions, and pesticides (which are toxic to many living life forms and organisms) are being introduced into the water bodies which contaminate the whole water system. Many industrial activities such as dyeing, printing, mining and metallurgical engineering, electroplating, nuclear power operations, semiconductor, aerospace, and battery manufacturing processes are some of the examples that discharge pollutants into the water stream.[1.24] One of the major classes of aquatic pollutants that have spread in global waters and caused large-scale health and environmental problems is the anionic pollutants. Anionic pollutants such as nitrate, fluoride, phosphate, perchlorate, chromate, bromate and arsenate have been found responsible in contaminating the water

resources.[1.25] Organic pollutants such as dyes are also equally responsible for the deterioration of the water bodies.

These pollutants whether organic or inorganic, are posing a serious threat to humanity and its subsequent removal from these water bodies has become utmost importance. During the last few decades, various treatment technologies including precipitation, coagulation , reverse osmosis, electrodialysis, adsorption and biological methods have been incorporated for the removal of pollutants from wastewater.[1.26] It has always been a challenge in the part of researchers to come up with the best process that is efficient, cost-effective and draws less energy for its operation for the removal of these pollutants from water. Among the above mentioned processes, adsorption is one of the widely used processes that have been employed for a wide variety of aquatic pollutants. The adsorption of pollutant species at the solid–liquid interface and its effect on the fate and mobility of pollutants in the environment is directly controlled by diverse properties of the pollutant and the adsorbent. The interaction of these pollutants with various surfaces could be exploited for the removal of these pollutants from waste water sources.

Numerous adsorbents, possessing variable properties, have been utilized for the interaction and removal of different pollutants from wastewater. Anionic pollutants have been successfully separated out from the solution using various adsorbents. For *e.g*, the feasibility of nano-alumina for nitrate removal from aqueous solutions was evaluated by Bhatnagar *et al*.[1.27] Similarly the uptake of anionic pollutant bromate by amorphous aluminium hydroxide was studied by Chitrakar *et al*.[1.28] Phosphate interaction and removal study onto the surfaces of kaolinite and alumina was carried out by Chen e*t al*.[1.29] Similarly, lot of work has been reported for the interaction and adsorption studies of dyes onto various surfaces. For instance, Chu *et al.* studied the adsorption of Rhodamine B from aqueous solution using silica fume (SF) and coal fly ash (CFA).[1.30] Ai *et al*. have synthesized a hierarchical porous NiO architecture and utilized for the effective removal of organic dye from aqueous solution. The NiO architectures with the hierarchical porous structure can be used as recyclable adsorbents for the rapid and efficient removal of Congo red (CR) from aqueous solution. They have reported existence of the electrostatic attraction between NiO architectures and CR, which is responsible for the high performance of the NiO architectures.[1.31]

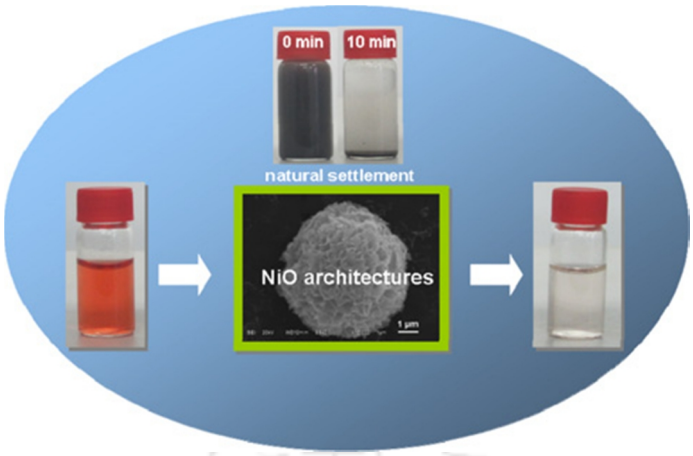

Figure 1.5. Hierarchical porous NiO architectures as highly recyclable adsorbents for effective removal of organic dye from aqueous solution. (Adopted from reference 1.31)

$FeTiO_3$ nanoparticles have been used for the removal of methylene blue.[1.32] Kim *et al*. reported the adsorption of Fluorescein using magnetic mesoporous materials.[1.33] Adsorption of Rhodamine 6G onto negative colloidal particles were reported by Leng *et al*.[1.34] On the basis of previously reported literature; it is well established that nanoparticles having high surface area and specific surface active groups provide high adsorption efficiency. Sharma *et al*. have used graphene oxide nanosheet for the removal of methy green dye from aqueous source. The results obtained from this study concludes that the adsorption process is governed by physical adsorption which is mainly due to electrostatic interaction of oppositely charged adsorbate−adsorbent species along with the π–π interaction.[1.35]

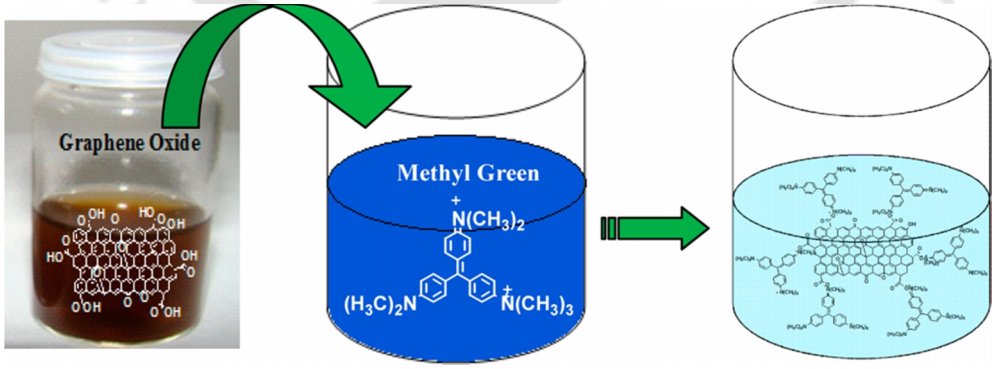

Figure 1.6. Removal of a cationic dye (methyl green) from aqueous solution using grapheme oxide nanosheets. (Adopted from reference 1.36)

Saha *et al*. have efficiently used iron oxide nanoparticles for the selective interaction and removal of dyes. They have reported a preferable and enhanced adsorption phenomena of the dyes containing hydroxyl (-OH) groups on iron oxide nanoparticles. They have

considered dyes Eriochrome black T (EBT), Bromophenol blue (BPB), Bromocresol green (BCG), and Fluorescein (FLU) which were adsorbed in much higher amounts as compared to Methyl red (MR), Methyl blue (MB), and Methy orange (MO). Results have suggested the reason behind such preferential adsorption phenomena, which could attributed to the presence of -OH groups present in those selective dyes, which can bind easily with the surface hydroxyl groups of magnetite nanoparticles.[1.36]

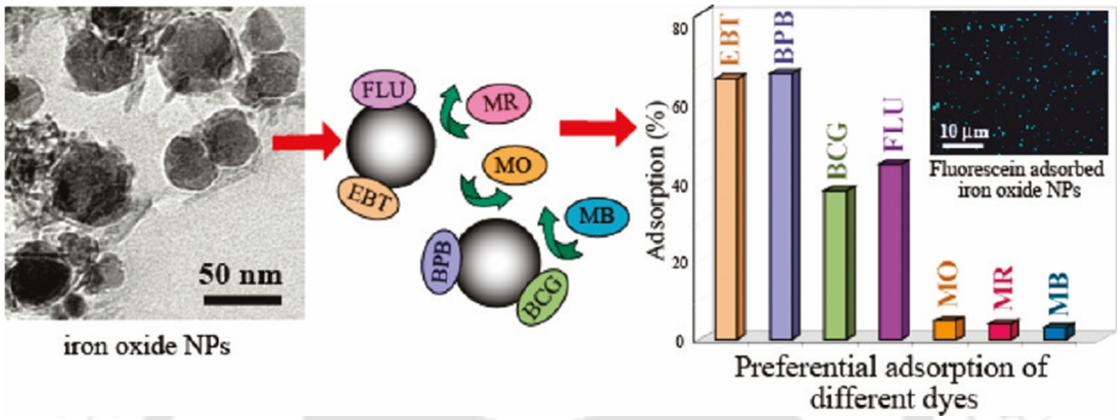

Figure 1.7. Preferential and enhanced removal or dyes containing hydroxyl groups using iron oxide nanoparticles**.** (Adopted from reference 1.37)

Overall these studied provide better understanding of the adsorption phenomena and indicated the potential usefulness of inorganic surface for adsorption interaction study.

1.6 Objective of thesis work

Based on the extensive literature survey, this thesis aimed to study the influence of inorganic surface properties on the interaction of different proteins and ionic pollutants at solid-liquid interface. Broadly, various inorganic mineral based micro-to-nano particles have been prepared and used for these interaction studies. Effort has been made to understand the in-depth interaction phenomenon of proteins and pollutants with proper understanding of the physiochemical phenomena, in terms of physico-chemical properties, kinetics, adsorption equilibrium and conformational analysis of proteins and pollutants with theses inorganic surfaces. Interaction process has been studied in terms of different regulating parameters such as pH, temperature, analyte concentration etc., to analyze the kinetic, thermodynamic and equilibrium properties of the adsorption processes. Further, the surface chemistry of different inorganic surfaces has been exploited to achieve a control over the interaction with protein and pollutants. Various

analytical techniques have been employed to quantify the adsorbed amount of the analytes and to characterize protein conformation at different solid-liquid interfaces. Finally, the influence of significant parameters and surface properties of analyte adsorption process on these inorganic materials are analyzed together, towards achieving a control over such interaction processes.

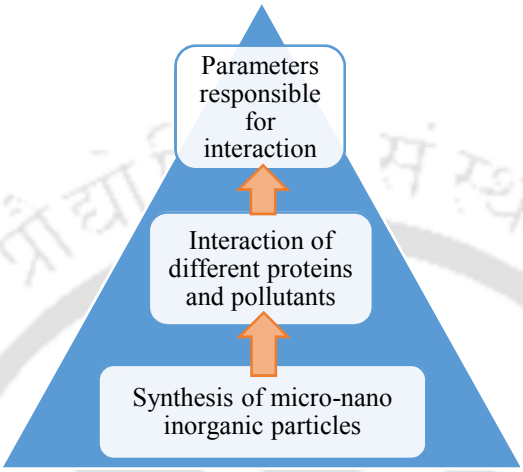

References

[1.1] (a) A. Bhaduri, K. P. Das, J. Dispersion Sci. Technol. 20 (1999) 1097- 1123. (b) K. Nakanishi, T. Sakiyama, K. Imamura, J. Biosci. Bioeng. 91 (2001) 233-244.

[1.2] M. Kroslak, Investigation of deposition and adsorption on solid-liquid interfaces through optical waveguide light mode spectroscopy, http://dx.doi.org/10.3929/ethz-a-005244118.

[1.3] J. Lyklema, Fundamentals of Interface and Colloid Science II: Solid-Liquid Interfaces, 1995, Academic Press, San Diego.

[1.4] (a) R. J. Hunter, Foundations of Colloid Science, 2001, 2nd ed., Oxford University Press, Oxford. (b) A. Dabrowski, Adv. Colloid Interface Sci. 93 (2001) 135-224.

[1.5] (a) W. Stumm, J. J. Morgan, Aquatic chemistry 1981, 2nd ed.Wiley. (b) W. Schlebaum, G. Schraa, W. H. van Riemsdijk, Environ. Sci. Technol. 33 (1999) 1413-1417. (c) G. Xia, W. B. Ball, Environ. Sci. Technol. 33 (1999) 262-269.

[1.6] J. Westall, Adsorption Mechanisms in Aquatic Surface Chemistry, Aquatic Surface Chemistry, W. Stumm, Ed., 1987, John Wiley and Sons, New York.

[1.7] (a) B. G. Linsen, Physical and chemical aspects of adsorbents and catalysts, Academic press, London, 1970. (b) R. T. Yang, Adsorbets; Fundamentals and Applications, 2003, John Wiley & Sons, Inc, New York,

[1.8] (a) N. L. Rosi, D. A. Giljohann, C. S. Thaxton, A. K. R. Lytton-Jean, M. S. Han, C. A. Mirkin, Science, 312 (2006) 1027-1030. (b) X. Michalet, F. F.Pinaud, L. A. Bentolila, J. M. Tsay, S. Doose, J. J. Li, G. Sundaresan, A. M. Wu, S. S. Gambhir, S. Weiss, Science, 307 (2005) 538-544. (c) M. A. Dobrovolskaia, S. E. McNeil, Nat. Nanotechnol. 2 (2007) 469-478.

[1.9] K. Nakanishi, T. Sakiyama, K. Imamura, J. Biosci. Bioeng. 91 (2001) 233-244.

[1.10] (a) W. G. Pitt, S. L. Cooper, J. Biomed. Mater. Res. 22(1988) 359-382. (b) M. Taborelli, L. Eng, P. Descouts, J. P. Ranieri, R. Bellamkonda, P. Aebischer, J. Biomed. Mater. Res. 29 (1995) 707-714. (c) T. J. Lenk, T. A. Horbett, B. D. Ratner, K. K. Chittur, Langmuir, 7 (1991) 1755-1764. (d) G. B. Sigal, M. Mrksich, G. M. Whitesides, J. Am. Chem. Soc. 120 (1998) 3464-3473. (e) T. C. Ta, M. T. McDermott, Anal. Chem. 72 (2000) 2627-2634.

[1.11] (a) J. Buijs, W. Norde, J. W. T. Lichtenbelt, Langmuir 12 (1996) 1605-1613. (b) J. C. Froberg, T. Arnebrant, J. McGuire, P. M. Claesson, Langmuir 14 (1998) 456-462.

[1.12] (a) W. Norde, Clin. Mater. 11 (1992) 85-91. (b) A. V. Elgersma, R. L. J. Zsom, W. Norde, J. Lyklema, Colloids Surf. 54 (1991) 89-101.

[1.13] P. Roach, D. Farrar, C. C. Perry, J. Am. Chem. Soc. 127 (2005) 8168-8173.

[1.14] K. Rezwan , L. P. Meier , M. Rezwan , J. Vörös , M. Textor , L. J. Gauckler, Langmuir, 20 (2004) 10055–10061.

[1.15] M. Bardhan, G. Mandal, T. Ganguly, J. Appl. Phys. 106 (2009) 034701-034705.

[1.16] M. Mahmoudi, M. A. Shokrgozar, S. Sardari, M. K. Moghadam, H. Vali, S. Laurent, P. Stroeve, Nanoscale, 3 (2011) 1127-1138.

[1.17] W. Shang, J. H. Nuffer, J. S. Dordick, R. W. Siege Nano Lett. 7 (2007) 1991–1995.

[1.18] F. Turci, E. Ghibaudi, M. Colonna, B. Boscolo, I. Fenoglio, B. Fubini, Langmuir, 26 (2010) 8336–8346 .

[1.19] S. Chakraborti, T. Chatterjee, P. Joshi, A. Poddar, B. Bhattacharyya, S. P. Singh, V. Gupta, P. Chakrabarti, Langmuir, 26 (2010) 3506–3513.

[1.20] P. Roach, D. Farrar, C. C. Perry, J. Am. Chem. Soc.128 (2006) 3939-3945.

[1.21] K. Kandori, K. Murata, T. Ishikawa, Langmuir, 23 (2007) 2064-2070.

[1.22] K. Rezwan , A. R. Studart, J. Vörös , L. J. Gauckler, J. Phys. Chem. B, 109 (2005) 14469-14474.

[1.23] M . Madliger, M. Sander, R. P. Schwarzenbach, Environ. Sci. Technol. 44 (2010) 8877–8883.

[1.24] (a) Y. Wang, W. Chu, Ind. Eng. Chem. Res. 50 (2011) 8734-8741. (b) M.M. Hassan, Health Policy, 74 (2005) 247-260. (c) J. Iqbal, H. J. Kim, J. S. Yang, K. Baek, J. W. Yang, Chemosphere. 66 (2007) 970-976. (d) H. Gecol, E. Ergican and A. Fuchs, J. Membr. Sci. 241 (2004) 105-119. (e) M. Costa, Toxicol. Appl. Pharmacol. 188 (2003) 1-5.

[1.25] (a) J. DeZuane, Handbook of Drinking Water Quality, John Wiley & Sons, New York, 1997. (b) A. H. Smith, P. A. Lopipero, M. N. Bates, C. M. Steinmaus, Science 296 (2002) 2145–2146. (c) M. Petrovic, S. Gonzalez, D. Barceló, Trends Anal. Chem. 22 (2003) 685–696.

[1.26] (a) J. Duan, J. Gregory, Adv. Colloid Interface Sci. 100–102 (2003) 475–502. (b) P. Lito, J. S. Aniceto, C. Silva, Water Air Soil Pollut. 223 (2012) 6133–6155. (c) N. Kabay, Ö. Arar, S. Samatya, Ü. Yüksel, M. Yüksel, J. Hazard. Mater. 153 (2008) 107–113.

[1.27] A. Bhatnagar, E. Kumar, M. Sillanpää, Chem. Eng. J. 171 (2011) 811–840.

[1.28] R. Chitrakar, K. Mizobuchi, A. Sonoda, T. Hirotsu, Ind. Eng. Chem. Res. 49 (2010) 8726–8732.

[1.29] Y. S. R. Chen, J. N. Butler, W. Stumm, J. Colloid Interface Sci. 43 (1973) 421–436.

[1.30] Y. Wang, W. Chu, Ind. Eng. Chem. Res. 50 (2011) 8734-8741.

[1.31] L. Ai, Y. Zeng, Chem. Eng. J, 215-216 (2013) 269–278.

[1.32] Y. H. Chen, J. Non-Cryst. Solids, 357 (2011) 136-139.

[1.33] B. C. Kim, J. Lee, W. Um, J. Kim, J. Joo, J. H. Lee, J. H. Kwak, J. H. Kim, C. Lee, H. Lee, R. S. Addleman, T. Hyeon, M. B. Gui, J. Kim, J. Hazard. Mater. 192 (2011) 1140-1147.

[1.34] X. Leng, K. Starchev, J. Buffle, Langmuir, 18 (2002) 7602-7608.

[1.35] P.Sharma, M. R. Das, J. Chem. Eng. Data, 58 (2013) 151−158.

[1.36] B. Saha, S. Das, J. Saikia, G. Das, J. Phys. Chem. C, 115 (2011) 8024–8033.

Chapter 2

Experimental Section

Chapter 2

This chapter describes the generalized materials and methodology followed for the synthesis and characterization of different micro- to nano-scale solid surfaces. It also describe es the general equipment and different experimental set ups/calculations used in studying the interaction of different proteins and pollutants on various inorganic surfaces.

2.1. Materials

All the chemicals used here are of analytical grade quality and were used without further purification unless otherwise specified. Pyridine-2, 3-dicarboxylic was obtained from Sigma-Aldrich Chemicals, USA. Zinc acetate dihydrate; $Zn(OAc)_2.2H_2O$, Copper sulfate; $CuSO_4 \cdot 5H_2O$, Sodium bicarbonate; Na_2CO_3, Potassium dichromate; $K_2Cr_2O_7$, Sodium arsenate; $Na_2HAsO_4.7H_2O$ and aniline of analytical grade were procured *Merck India Ltd*. Sodium chloride; ($NaCl_2$), salicylic acid, Eriochrome Black T (EBT), Methylene Blue and Rhodamine B were purchased from *Loba Chemie Pvt. Ltd.*, India. Fluorescein, Rhodamine 6G and Congo Red dyes were also purchased from Sigma-Aldrich Chemicals, USA. Different proteins like (BSA; A2153 ~96%) and β-lactoglobulin (BLG; L0130 ~90%) were also obtained from *Sigma Chemicals*, USA. Other general chemicals used for different purpose for *e.g.* buffer preparation etc. were purchased from *Merck India Ltd*. and *CDH analytical reagent*, India. All the solvents used for spectroscopic studies were of spectroscopy grade and the distilled water and deionized water (Milli-Q system at 18.2 MΩ, Millipore, USA) was used in all experiments.

2.2. Different calculations used for quantification of adsorption process at solid-liquid interface

2.2.1. Adsorption capacity

Adsorption capacity is defined as the amount of solute adsorbed on the surface per unit amount or surface area of the adsorbent. Adsorption capacity generally denotes as q_e (mg g^{-1}) and can be calculated using the following equation:

$$q_e\ (mg\ g^{-1}) = \frac{C_0\ (mg\ L^{-1}) - C_e\ (mg\ L^{-1})}{D\ (g\ L^{-1})} \qquad (2.1)$$

Where, C_0 is the initial solute concentration (mg L^{-1}), C_e is the steady state solute concentration (mg L^{-1}), and D is the adsorbent concentration (g L^{-1}). The adsorption capacity can also be determined in term of per unit surface area of the adsorbent (q_e value, mg m^{-2}) from the steady state mass balance and specific surface area of the adsorbent.

2.2.2. Adsorption kinetics

The kinetics of adsorption process can be validated with the different kinetic models. The surface kinetics can be evaluated with first order and second order kinetic model.[2.1, 2.2] The linearized first order kinetics model is expressed as,

$$\log\ (q_e\ -\ q_t)\ =\ \log\ (q_e)\ -\ \frac{1}{2.303}k_1 t \qquad (2.2)$$

And the linearized second order kinetic is expressed as,

$$(\frac{t}{q_t})\ =\ (\frac{1}{q_e^2 k_2})\ +\ (\frac{t}{q_e}) \qquad (2.3)$$

Where, q_t and q_e (mg g^{-1} or mg m^{-2}) are the adsorption capacities at time t and at steady state respectively. The k_1 and k_2 are the first and second order rate constant respectively. Another empirically established functional relationship proposed by Weber and Morris,[2.3] the intraparticle diffusion model is also being used to fit the kinetic experimental results. The root time dependent equation is given by,

$$q_t = K_w t^{1/2} + C \qquad (2.4)$$

Where K_w(mg g^{-1} $min^{-0.5}$) is an intraparticle diffusion rate constant and C (mg g^{-1}) is the intercept. The slope in the linearized fitted curve using intraparticle model characterizes the rate parameter corresponding to the intraparticle diffusion, whereas the intercept of this portion is proportional to the boundary layer thickness.

2.2.3. Adsorption isotherm

Adsorption isotherm of different process is evaluated from the fitting with different isotherm models. Most widely used adsorption isotherms models *viz.* Langmuir and Freundlich isotherm were utilized for adsorption processes.[2.4, 2.5] The main consideration of Langmuir isotherm is sorption takes place at specific homogeneous sites within the adsorbent, indicating a monolayer adsorption (constant heat of adsorption for all sites). Langmuir isotherm is expressed as,

$$\frac{C_e}{q_e} = \frac{1}{Q_m\, b} + \frac{1}{Q_m} C_e \qquad (2.5)$$

Where, Q_m is the maximum monolayer uptake by the adsorbent (mg g^{-1}), and b is the energy (heat) constant of the adsorption. Now a constant separation factor as described by Hall *et al.* (1966),[2.6] called "constant separation factor" or "equilibrium parameter", R_L is defined as

$$R_L = (\frac{1}{1+bC_0}) \qquad (2.6)$$

R_L informs about the favorability of the sorption process. For a favorable reaction process, $0< R_L<1$; whereas $R_L=0$ for the irreversible case, $R_L=1$ for the linear case and $R_L>1$ for unfavorable reaction. The Freundlich adsorption isotherm is generally based on multilayer adsorption on heterogeneous surface this holds the assumption that the adsorption sites are distributed exponentially with respect to heat of adsorption. Freundlich isotherm is given as,

$$q_e = K_f C_e^{1/n} \qquad (2.7)$$

Where, K_f in the equation denotes the Freundlich's uptake factor and n denotes Freundlich's intensity factor. The value of n in the range of 1 to 10 denotes favourable adsorption, could be find out from the linearized form of Freundlich isotherm plot.

2.2.4. Thermodynamic analysis

The standard Gibbs free energy change (ΔG^0) of an adsorption process indicates its thermodynamic favorability ($\Delta G^0 < 0$ for a favorable process). The standard Gibbs free energy change (ΔG^o) was calculated from

$$\Delta G^0 = -RT\ \ln(k_c) \qquad (2.8)$$

Where R is the universal gas constant (8.314 J mol^{-1} K^{-1}) and T is temperature in Kelvin. k_c is the equilibrium stability constant, which was calculated at each temperature using the relation,

$$k_c = (\frac{C_s}{C_e}) \qquad (2.9)$$

Where, C_s and C_e is the equilibrium solute concentration on adsorbent (mmol g^{-1}) and aqueous phase (mmol mL^{-1}) respectively. Moreover, the average standard enthalpy change (ΔH^0) and entropy change (ΔS^0) can be determined from Van't Hoff equation[2.7],

$$\ln(k_c) = (\frac{\Delta S^0}{R}) - (\frac{\Delta H^0}{R})\frac{1}{T} \quad (2.10)$$

ΔH^0 and ΔS^0 were calculated from the slope and intercept of plot between $\ln(k_c)$ vs (1/T).

2.3. Particulars of Instruments/Equipments used for different types of studies

2.3.1. Atomic absorption spectra

The initial and residual metal ion concentrations after adsorption and desorption were measured by *AA240* atomic absorption spectrometer (*Varian Inc.*) in each case using different cathode lamp.

2.3.2. Single crystal X-Ray diffraction

A crystal of suitable size was selected from the mother liquor and immersed in silicone oil, then mounted on the tip of a glass fibre and cemented using epoxy resin. Intensity data for the crystals were collected using Mo-Kα radiation (λ = 0.71073Å) at 298(2) K, with increasing ω (width of 0.3o per frame) at a scan speed of 6 s/frame on a Bruker SMART APEX diffractometer equipped with CCD area detector.

2.3.3. Scanning electron microscope

Scanning electron micrograph (SEM) images of each samples glued on an aluminum stub and gold sputtered were obtained by means of a *LEO-1430 VP* electron microscope.

2.3.4. Transmission electron microscope

Samples were characterized by transmission electron micrograph (TEM) in a *JEOL 2100* UHR-TEM instrument. An amount of 5 μL of dispersion solution was drop-cast on carbon-coated copper grids and subsequently air-dried before TEM analysis.

2.3.5. Powder X-ray diffraction

Powder X-ray diffraction (PXRD) data were recorded with Seifert powder X-ray diffractometer (XRD 3003TT) with Cu K_α source (λ =1.54 Å) on a glass surface of an air-dried sample. The average crystallite size of the particles was estimated using the Debye−Scherrer equation.[2.8]

2.3.6. FT-IR spectra

FT-IR spectra were recorded at 4 cm^{-1} resolution with required scans with a *Perkin-Elmer* Spectrum One FT-IR spectrometer from 4000 to 450 cm^{-1}.

2.3.7. Steady state fluorescence spectra

The steady state fluorescence spectra of different samples were recorded on a steady state spectrophotometer *Horiba Fluoromax 4* (JOBIN VYON) using 10 mm path length quartz cuvettes.

Steady-state anisotropy measurement was also performed in *Horiba Fluoromax 4* (JOBIN VYON). Steady-state anisotropy (r) was defined by

$$r = \frac{I_{VV} - GI_{VH}}{I_{VV} + 2GI_{VH}} \qquad (2.11)$$

where, I_{VV} and I_{VH} are the intensities obtained with the excitation polarizer orientated vertically and the emission polarizer oriented vertically and horizontally, respectively. The *G* factor is defined as,

$$G = \frac{I_{HV}}{I_{HH}} \qquad (2.12)$$

The "*I*" terms refer to the parameters similar to those mentioned above for the horizontal position of the excitation polarizer and vertical and horizontal position of the emission polarizer, respectively.

2.3.8. Absorption spectra

UV-Visible spectra of the samples were recorded, on a *Perkin Elmer Lambda 25* UV-Visible spectrophotometer using 10 mm path length quartz cuvettes.

2.3.9. Circular dichroism spectra

The secondary conformational characteristics of proteins were investigated by far-UV CD spectra in a *J-810* (*JASCO*, Japan) spectropolarimeter. Spectra were analyzed for secondary structure content by a curve-fitting method described by Yang *et al.*[2.9] CONTIN in the Dichroweb online analysis was also used for the secondary structural analysis in some cases. An average molar mass of 105 and 115 Da per amino acid residue was used for calculating the molar ellipticity, [θ].

2.3.10. Specific surface area measurement

Specific surface area and pore volume of particle were determined using a *Beckman Coulter SA3100* surface area analyzer by measuring N_2 adsorption and adopting the well-known BET procedure.[2.10]

2.3.11. Thermo-gravimetric analysis

The thermo-gravimetric analysis (TGA) of materials was performed by using an SDTA 851 e TGA thermal analyzer (*Mettler Toledo*) with a heating rate of 2 °C/min in a N_2 atmosphere.

2.3.12. Surface charge analysis

Zeta potential (ζ-potential), which indicates the surface charge of the material at different pH was measured using a ζ-potential analyzer (model *1200 Micromeritics*) at room temperature.

2.3.13. pH measurement and sonication

pH of the different solutions were measured and adjusted with a *Varian* digital pH meter. Sonication of the samples was performed in a *Cyberlab* (model. 405) water bath ultra-sonicator.

References

[2.1] S. Lagergren, Handlingar, 24 (1898) 1-39.

[2.2] Y. S. Ho, G. McKay, Process Biochem. 34 (1999) 451-465.

[2.3] W. J. Weber, J. C. Morris, J. Sanit. Eng. Div. Am. Soc. Civ. Eng, 89 (1963) 31-60.

[2.4] I. Langmuir, J. Am. Chem. Soc. 38 (1916) 2221-2295.

[2.5] H. M. F. Freundlich, Z. Phys. Chem. 57 (1906) 385–470.

[2.6] K. R. Hall, L. C. Eagleton, A. Acrivos, T. Vermeulen, Ind. Eng. Chem. Fund. 5 (1966) 212-223.

[2.7] M. H. Kalavathy, T. Karthikeyan, S. Rajgopal, L. R. Miranda, J. Colloid Interface Sci. 292 (2005) 354-362.

[2.8] C. H. Yu, A. Al-Saadi, S. J. Shih, L. Qiu, K. Y. Tam, S. C. Tsang, J. Phys. Chem. C, 113 (2009) 537-543.

[2.9] J. T. Yang, C. S. C. Wu, H. M. Martinez, Methods Enzymol. 130 (1986) 208-269.

[2.10] S. P. Brunauer, P. H. Emmet, E. Teller, J. Am. Chem. Soc. 60 (1938) 309-319.

Chapter 3

ZnO-Protein interaction

Chapter 3

3.1. Introduction

In order to investigate the interaction of proteins with inorganic surfaces, this chapter describes the interaction study of protein with a basic 'hard' surface (according to Pearson's Hard-Soft Acid Base principle). ZnO nanoparticles (NPs) of different morphology have been synthesized from single precursor source and its interaction study with a model protein (β-lactoglobulin) has been presented in this chapter.

Inorganic nanoparticles have been a hot topic for research in recent years due to their novel physical and chemical properties, which add to the advantage for its various practical applications.[3.1,3.2] Among these inorganic nanoparticles, zinc oxide (ZnO), a semiconductor metal oxide, has emerged as a potential nanomaterial of choice. ZnO has a wide band gap (3.3 eV) and high excitonic binding energy (60 MeV) at room temperature, which makes it suitable for its extended use in a wide variety of applications such as catalysis, piezoelectric devices, gas-sensors, dye sensitized solar cells etc.[3.3,3.4,3.5] In addition, ZnO (NPs) have also emerged as useful biomaterial for biomedical applications due to their biocompatibility and high excitonic band gap.[3.6,3.7] However, the interaction of ZnO NPs with different biomolecules in above mentioned applications largely depend on its size and morphology; which in turn controlled by synthesis procedures. Various synthesis schemes play the pivotal role for the formation of ZnO of different size and morphology, such as nanospheres, nanorods, nanotubes, nanowires, multipods etc.[3.8] Numerous physical and chemical methods have been successfully utilized to fabricate ZnO of various size and morphology. Some examples are, pulsed laser deposition (PLD), chemical vapor deposition, spray pyrolysis, thermal evaporation, wet-chemical route, solid state transformation etc.[3.9] However, all these studies reported the requirement of distinct synthesis procedure for differentiation in morphology of ZnO nanoparticles. In this regard, a facile synthesis procedure with fine tuning in intermediate step would have been potential for controlling the morphology of ZnO which in turn would show different interfacial interactions.

3.2. Synthesis and characterization of morphologically different ZnO NPs from single precursor source

Control over the synthesis of morphologically different ZnO NPs, using same precursor aromatic organic acid as ligand for Zn^{2+} coordination, has been reported in this study. Pyridine-2,3-dicarboxylic acid (PDC) was used as a ligand to form Zn(II)-PDC precursor complexes of different architectures, which on further calcination at 600 ^{o}C produce ZnO NPs of different morphology. In an usual synthesis procedure, aqueous solution of PDC (5.6 mmol, 0.954 gm) was added drop wise to the aqueous solution of $Zn(OAc)_2.2H_2O$ (2.8 mmol, 0.626 gm) with constant stirring at room temperature for a period of 6 hrs. White precipitate was formed which was filtered, washed with water and dried in vacuum prior to characterization. The precipitate was partially soluble in water when heated to 80 ^{o}C. The soluble filtrate was kept for crystallization. The insoluble portion was dissolved by adding few drops of base (aniline) and also kept for crystallization. Two different complexes of Zn(II)-PDC were obtained (as resolved by single crystal XRD analysis). The water soluble portion gave a monomer Complex **1** and the later gave a co-ordination polymer Complex **2**. Finally, both the precursor complexes were calcined at 600 ^{o}C for 4 hrs to get the ZnO NPs. The monomer Complex **1** was heated to give disk-like ZnO NPs of ~30 nm whereas the co-ordination polymer Complex **2** was calcined to get the ZnO nanorods of ~ 100 nm.

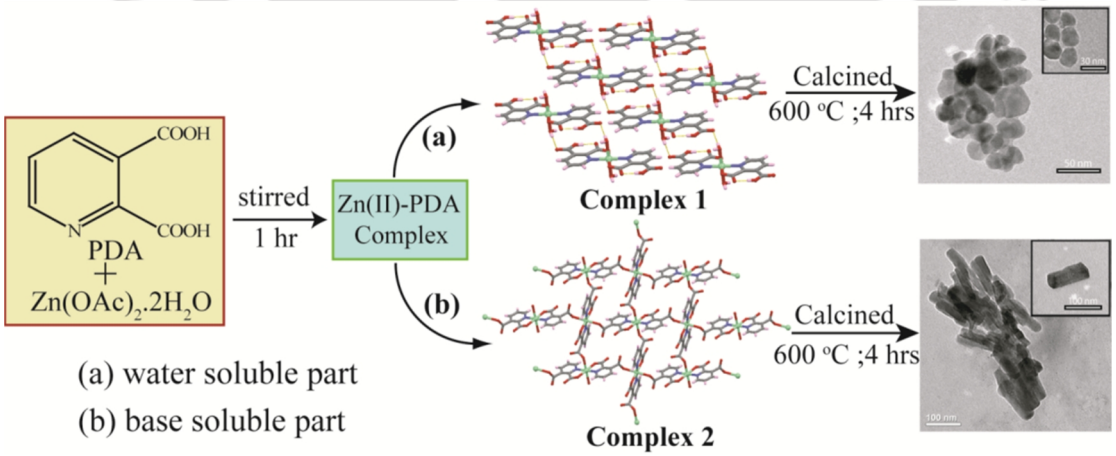

Scheme 3.1. Schematic representation of the synthesis of morphologically different ZnO nanoparticles from single precursor source.

The synthesized Zn-PDC complexes and the ZnO NPs were characterized accordingly by several techniques. The crystals obtained by the aforesaid technique were solved and the crystallographic data and details of data collection parameters are provided in the

Appendix section. The crystals formed from the water soluble part were monomer Complex **1,** whereas the crystals obtained from the base soluble part was a co-ordination polymer Complex **2** (Figure 3.1). The FT-IR spectra of these complexes clearly show the change in the monomer and co-ordination polymer complex (Appendix, Figure A3.1).

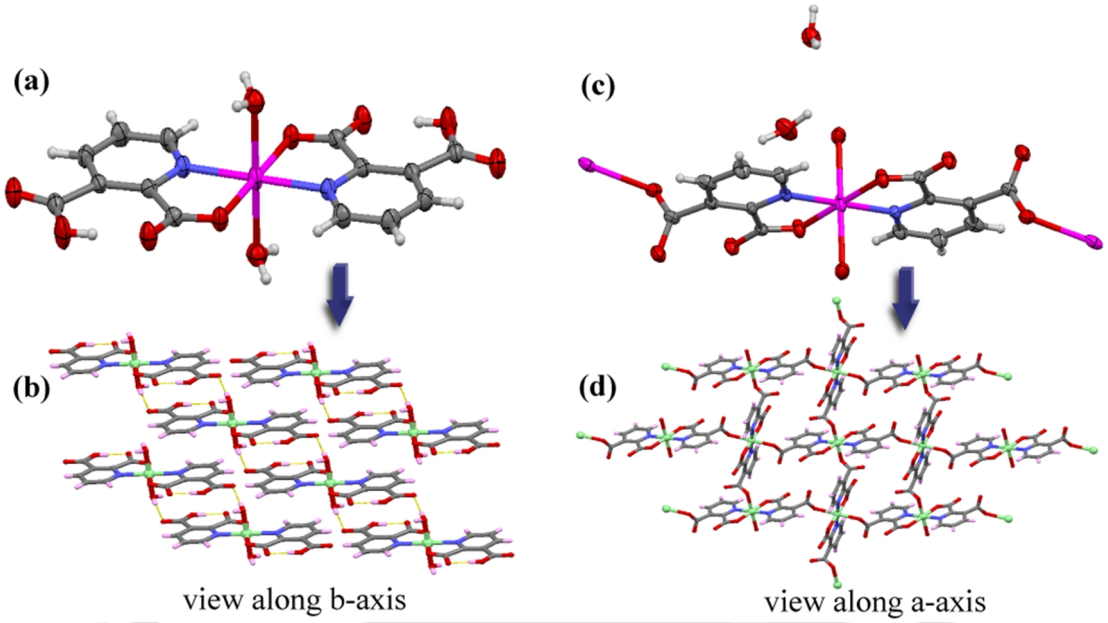

Figure 3.1. Ellipsoid plot and packing diagram of **Complex 1** (a,b) and **Complex 2** (c,d) respectively.

The TEM micrograph (Figure 3.2) reflects the formation of ZnO NPs after calcination of these complexes. Figure 3.2a shows that disk-like ZnO nanopowders obtained from the calcination of the monomer Complex **1**, whereas Figure 3.2b shows the formation of nanorods formed from the co-ordination polymer Complex **2**. The FT-IR spectra support the formation of the nanoparticles (inset of Figure 3.2c and 3.2d). In the infrared region, ZnO usually shows distinct absorption bands around wave numbers of 464 cm^{-1} and this maximum broadens and splits into two maxima if the particle morphology changes from spherical to a needle like shape.[3.10,3.11] The nanopowder shows a distinct peak at around ~480 cm^{-1}. Whereas in case of the nanorods the characteristic Zn-O peak shifts to ~520 cm^{-1} followed by a broad peak in the region beyond 450 cm^{-1} (which cannot be detected by this instrument of study). The peaks at ca. 3450 and 1620 cm^{-1} should be derived from the -OH group of adsorbed water on the ZnO surfaces which are present in both the cases.[3.12,3.13] Figure 3.2c and Figure 3.2d shows the Powder X-ray diffraction (PXRD) pattern of the ZnO NPs formed. The crystallinity of the NPs is good

as indicated by the narrow and strong diffraction peaks. All the spectrum peaks in both the cases can be easily assigned to pure ZnO, which are in good agreement with the JCPDS card of wurtzite ZnO (JCPDS No. 65-3411). No characteristic peaks from other impurities are detected. From the PXRD pattern it was observed that the (002) peak of the sample prepared by calcinations from the Zn(II)-coordination polymer showed higher intensity than of (100), indicating the preferred orientation along *c*-axis. The PZC (point of zero charge) values were found to be around pH~9.32 and pH~9.24 for disk-like ZnO and ZnO nanorod, respectively (Appendix, Figure A3.2). The UV-Vis and the PL spectra for both the ZnO NPs are given in the supporting section (Appendix, Figure A3.3 and A3.4). The N_2 adsorption isotherm of the BET analysis reveals that the disk-like ZnO NPs have a higher specific surface area of 20.25 m^2 g^{-1} compared to the ZnO nanorods with 6.60 m^2 g^{-1} (Appendix, Figure A3.5).

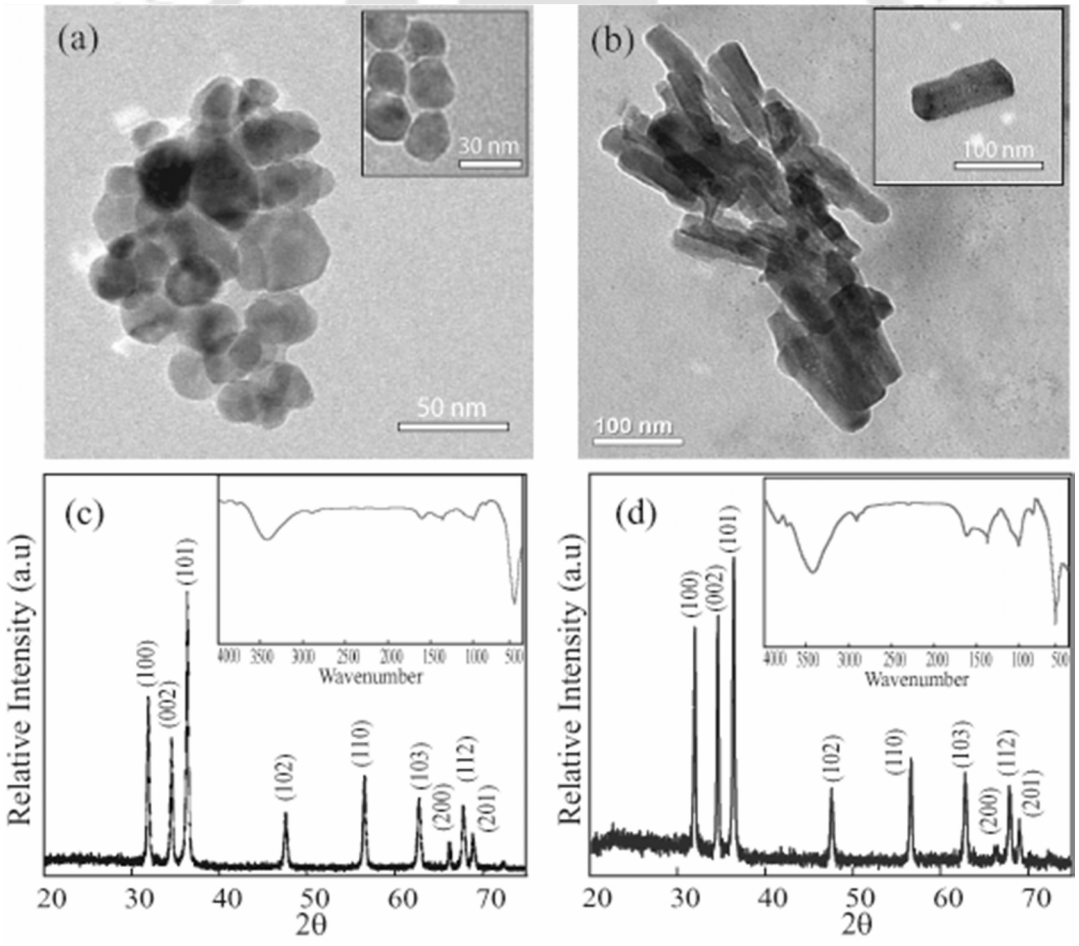

Figure 3.2. TEM image of (a) disk-like ZnO NPs and (b) ZnO nanorod; Powder XRD of (c) disk-like ZnO NPs and (b) ZnO nanorod (inset: FT-IR of (c) disk-like ZnO NPs and (b) ZnO nanorod).

3.3 Interaction study with protein

3.3.1 Background

Interaction of biomolecules such as proteins with different types of solid surface is the fundamental phenomenon in several biomaterial and biomedical applications.[3.14] When the protein comes in contact with nanoparticles, an alteration in the protein conformation might take place which could expose new epitopes on the protein surface, or perturb the normal protein function, which can be important in various biotechnological application.[3.15] Different proteins behave differently when exposed to a given surface and the process is very complicated. Utilising various spectroscopic techniques one can evaluate these interactions and try to get a better understanding of the process which governs the overall protein interaction. After all the control over the interaction of proteins and its structure-function relationship is the most significant tool which can control the overall application.

Different inorganic mineral oxides have been extensively used for the interaction study with different biomolecules. Amongst these inorganic minerals, ZnO NPs, due to its potential biomedical application have been used widely for the study of adsorption of various proteins and enzymes. Chakraborti *et al*. have reported the study of adsorption of lysozyme onto ZnO NPs.[3.16] Zhang *et al*. have done a detailed investigation of the interaction of ZnO NPs with glucose oxidase.[3.17] BSA binding study with colloidal ZnO NPs have been reported by A. Kathiravan *et al*.[3.18] A comparative study of native ZnO and ZnO NPs for the immobilization of β-galactosidase via simple adsorption mechanism has been reported by Q. Husain *et al*.[3.19] All these studies aim towards the better understanding of protein-ZnO constructs. However, critical literature survey reveals that so far no such attempt was made to investigate the in-depth and differential interaction of β-lactoglobulin with ZnO NPs. β-lactoglobulin is a major protein of the whey fraction of cow's milk with the concentration of β-lactoglobulin in milk of about 0.2 g/100 ml, next to casein (2.9 g/100 ml).[3.20] β-lactoglobulin forms a dimer, at physiological conditions, with each monomer consisting of 162 amino acids. Below pH 3, the dimer dissociates into monomers which preserve their native conformation.[3.21] In this section, the interaction of β-lactoglobulin with ZnO NPs was investigated. We have determined the adsorption co-efficient (q_e) as a function of protein concentration, pH, temperature, time and ZnO NPs dose. Change in secondary and tertiary structure of the protein upon adsorption was also studied using CD and fluorescence spectroscopy. The

overall kinetics of adsorption process and Gibbs free energy of the adsorption has also been estimated. Overall, efforts were given to gain control over the β-lactoglobulin-ZnO interaction and its structure-functional relationship.

3.3.2 Materials and methods

Protein. Prior to each adsorption experiment, fresh aqueous protein solutions of different concentrations with Milli-Q water (18.2 MΩ) were prepared. The concentration of the stock solution of the protein was 1 mg ml^{-1}. The concentration of the protein was varied from 50-500 μg ml^{-1} and ZnO NPs concentration was kept constant at 0.5 mg ml^{-1}.

Adsorption of β−lactoglobulin. Adsorption experiments of β-lactoglobulin onto ZnO NPs were carried out in batch mode. The adsorption studies were carried out in small centrifuging tubes. ZnO NPs were added to the protein solution in the centrifuging tubes and allowed to shake to reach equilibrium. Adsorption kinetics was studied by withdrawing the samples at regular interval and subsequent centrifugation to obtain suitable aliquots for analysis of protein concentration. Preliminary studies showed that this period of time is sufficient to ensure steady state. After equilibrium is reached the nanoparticles were separated from the solution in a 15000 rpm centrifuge. The supernatant solution was then analyzed for the remaining protein concentration using the Bradford assay measuring the absorbance at 595 nm. To ascertain the thermodynamic facet of the adsorption the temperature of the system was varied from 10 to 40 ^{o}C.

Fluorescence Emission Spectroscopy. The excitation wavelength at 290 nm was chosen because almost all the fluorescence emission signal excited at this wavelength is derived from tryptophan. The tryptophan emission fluorescence spectrum was collected in the wavelength range of 320−500 nm. The emission spectra of protein samples containing ZnO NPs were corrected using the baseline acquired from suspension of the same concentration of ZnO NPs without protein. Steady-state anisotropy measurement was also performed in all the cases.

Circular Dichroism. CD spectra of native and adsorbed protein were measured to evaluate the secondary structural change. Three different concentration of ZnO was taken for CD spectral analysis.

3.3.3 Adsorption interaction

3.3.3.1 Preliminary observation

The interaction of proteins with inorganic mineral nanoparticles and nanoparticle-based materials is a fundamental phenomenon which has broad and emerging fields of applications like biomaterials, bio-separation technology, and bio-nanotechnology. Moreover, in nanotechnology, protein surface interactions are crucial for assembly of interfacial protein constructs, such as sensors and activators. ZnO being one of the biocompatible inorganic materials we proceed to investigate the interaction of a protein (β-lactoglobulin) and its fate after adsorption on these NPs.

From our preliminary investigation we found that the disk-like ZnO NPs showed much higher adsorption co-efficient value (q_e) as compared to the nanorods (values summarized in Table 3.1). The probable reason behind this incongruity may lie in the difference of their BET surface area. As revealed from the BET surface area analysis, the surface area of the disk-like ZnO NPs was much larger than the ZnO nanorods (see Table 3.1). The adsorption values with the ZnO nanorods were quite insignificant compared to the disk-like ZnO NPs, so we have further proceeded with the in-depth experiments with disk-like ZnO NPs only. Furthermore during our study, ZnO NPs are more or less positively charged under all experimental conditions (in the range pH 5-9), although the surface charge density would be different at different experimental condition. Prior to carry out the protein adsorption study, prolonged sonication of ZnO NPs was done to get a mono-disperse colloidal solution in each case. We have done detail adsorption studies varying various parameters as discussed below.

Table 3.1. Comparison of disk like ZnO NPs and ZnO nanorods.

	Particle size (nm)	BET surface area (m^2/g)	Adsorption capacity, q_e (mg g^{-1})		
			pH~5	pH ~7	pH~ 9
ZnO disk-like	~30	20.25	348	331.3	69.45
ZnO nanorod	~100	6.60	91.2	78.5	45.9

3.3.3.2 Influence of nanoparticle concentration

The interaction of protein-ZnO was studied under different ZnO NPs concentration. The protein concentration was kept constant (300 μg ml^{-1}) whereas the ZnO NPs concentration was varied from 0.2 to 0.8 mg ml^{-1}. As the concentration of ZnO NPs was increased the adsorption coefficient (q_e) was decreased (Fig. 3.3). With the ratio of protein to ZnO NPs concentration decrease from 1.5 to 0.375, the corresponding (qe) value also decreases form 370.16 to 198.32 mg g^{-1}. Although, the total removal efficiency is increased with the increase in nanoparticles concentration, the total surface area and in turns the number of active adsorption sites increases but the amount of protein adsorbed per unit mass/area of adsorbent decreases, resulting in reduction of the adsorption capacity (q_e).

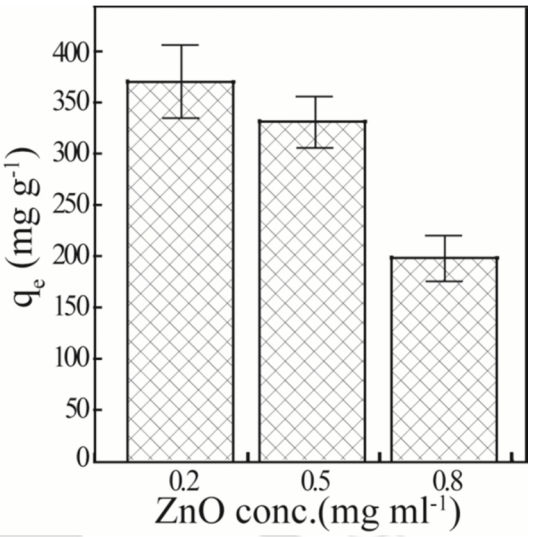

Figure 3.3. Concentration variation of ZnO NPs from 0.2 to 0.8 mg ml^{-1} where protein concentration was 300 μg ml^{-1}.

3.3.3.3 Influence of pH

To see the effect of pH on the adsorption processes, adsorption experiment was carried out at three different pH (5, 7 and 9). The adsorbed amount of β-lactoglobulin was highest at pH ~5.0, given by the steady state adsorption capacity (q_e) value of ~348 mg g^{-1}. This was followed by pH~7.0 with a q_e value of ~331.3 mg g^{-1} and at pH~9 the adsorption decreased to a value of ~69.45 mg g^{-1} (Figure 3.4). All transitions that take place between pH 2.0 and pH 9.0 do not cause any appreciable changes in the native like β-barrel conformation of β-lactoglobulin.[3.22] By contrast, above pH 9.0, β-lactoglobulin undergoes an irreversible, base-induced unfolding transition with global disruption of both secondary and tertiary structures.[3.23] On a hydrophilic solid surface like ZnO, electrostatic attraction between a charged surface and an oppositely charged protein molecule is often the driving force for adsorption from solution on to the solid surface. Other factor such as protein-protein lateral electrostatic interaction also plays a

major role in the adsorption process. At pH ~5.0 the ZnO NPs surface is more positively charged and the protein is more in neutralized condition to slightly negatively charged ($IEP_{\beta\text{-}LG}$~5); hence the binding capacity of the protein on disk-like ZnO NPs was very high. Moreover, being neutral to less negatively charged molecules, the lateral repulsion force between the protein molecules also negligible, which give rise to a high surface coverage on ZnO NPs at this pH (Figure 3.5). With the increase of the pH, though the electrostatic attraction between ZnO and lactoglobulin molecules remains, but the ZnO surface become less positively charged and importantly the lateral protein-protein repulsion at solid-liquid interface increases. This results in less adsorption capacity at higher pH. Thus, at pH ~9.0, binding capacity of lactoglobulin on ZnO surface reduces to many folds majorly due to the high lateral repulsion and partial base induced denaturation of β-lactoglobulin at ZnO interface. Moreover, as the PZC (point of zero charge) of ZnO approaches, the ZnO surface becomes more neutralized compared to that of at acidic pH. This change in surface charge also affects the electrostatic interaction between protein and ZnO NPs surface and in turn reduce the binding of the protein as obtained in experiments.

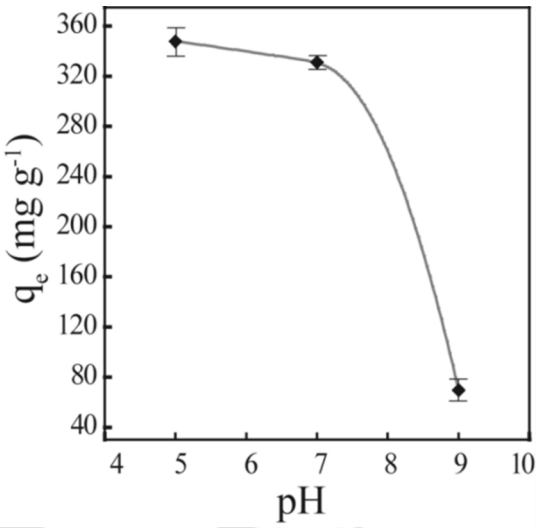

Figure 3.4. Adsorption capacity (q_e) with varying pH, where protein concentration was 300 μg ml^{-1} and NPs concentration 0.5 mg ml^{-1}.

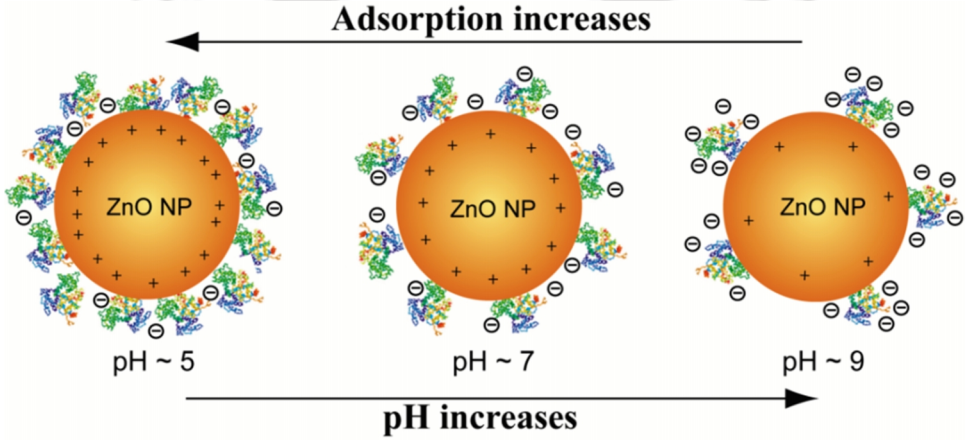

Figure 3.5. Schematic representation of adsorption of β-lactoglobulin onto ZnO surface with pH variation.

3.3.3.4 Adsorption equilibrium and kinetic model analysis

The equilibrium time for any adsorption process is controlled by the rate of uptake of the proteins onto the nanoparticles which is the kinetics of the adsorption process. The kinetics of adsorption determines the optimum operating conditions for the full-scale batch process and gives important information for designing and modeling the processes.[3.24] Thus, the effect of contact time was analyzed from the kinetic point of view. For equilibrium study, ZnO NPs and β-lactoglobulin solution, having a concentration of 0.5 mg ml^{-1} and 300 μg ml^{-1} was taken, respectively. Aliquots of sample (0.5 ml) was collected at an interval of 15 min and centrifuged at 15000 rpm. The supernatant was measured for the protein concentration. The optimum time was found to be 2 hrs for the adsorption process (Figure 3.6).

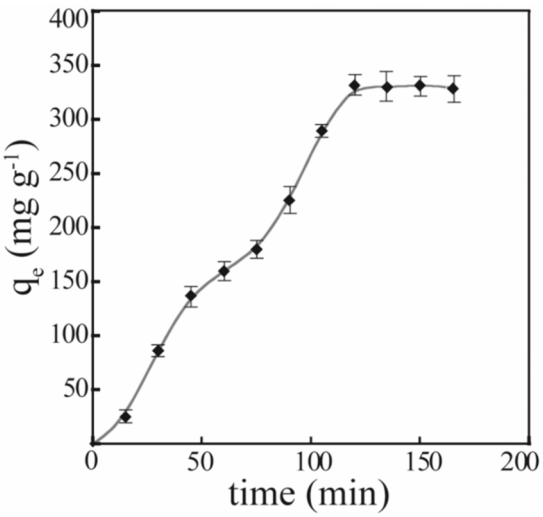

Figure 3.6. Adsorption capacity (q_e) with time (minutes), where protein concentration was 300 μg ml^{-1} and NPs concentration 0.5 mg ml^{-1}.

The adsorption kinetics of β-lactoglobulin onto ZnO NPs was studied with respect to Lagergren first order (Eq. 3.1a) and second order kinetic model (Eq. 3.1b).[3.25]

$$\log(q_e - q_t) = \log q_e - (1 / 2.303)\, k_1 t \qquad (3.1a)$$

$$(t / q_t) = (1/ q_e^2 k_2) + (t / q_e) \qquad (3.1b)$$

Where, the q_t and q_e (mg g^{-1}) are total adsorption capacity at time t and at equilibrium respectively. k_1 and k_2 are first and second order rate constant respectively. Table 3.2 shows all the kinetic constant values. The value of k_1 was found to be 0.0123 and the first order rate equation showed correlation coefficient of 0.988; while the second order correlation coefficient was 0.990 and k_2 was found to be 2.7×10^{-5}. Therefore the adsorption process for β-lactoglobulin onto ZnO can be better described by the second order reaction kinetics, which is mainly due to the actual heterogeneous distribution at NPs surface.

Table 3.2. Comparison of rate constants calculated based on first-order and second-order kinetic models.

	First order kinetics		Second order kinetics	
	k_1 (L min^{-1})	R	k_2 (g mg^{-1} min^{-1})	R
β-lactoglobulin	0.0123	0.988	$2.7x10^{-5}$	0.990

3.3.3.5 Effect of temperature and thermodynamic analysis

The thermodynamic favorability of a process can be obtained from the analysis of temperature of the system. To study the effect of temperature we have performed the interaction study at elevated temperature from 10 to 40°C. With the increase in temperature the adsorption capacity decreased. The adsorption was highest at 10°C with the qe value of ~355.10 mg g^{-1} and gradually decreased to ~310.22 mg g^{-1} as the temperature was increased to 40°C (Figure 3.7). The decrease in the adsorption with the increases in temperature might be due to the partial unfolding of the protein structure when heated. As the unfolding of β-lactoglobulin leads to the exposure of the hydrophobic patches to the solution, it can in turn affect the interaction with hydrophilic ZnO surface. This can results in the reduced adsorption affinity of the protein on ZnO surface at higher temperature. Moreover, the standard Gibbs free energy change (ΔG°) of the adsorption process was calculated from the following equation (Eq. 3.2a),

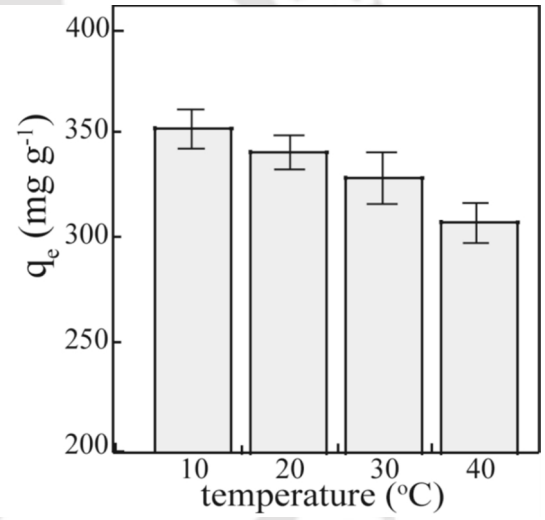

Figure 3.7. Adsorption capacity (q_e) with temperature (°C), where protein concentration was 300 µg ml^{-1} and NPs concentration 0.5 mg ml^{-1}.

$$\Delta G^o = - RT \ln(k_c) \quad (3.2a)$$

Where R is the universal gas constant (8.314 J mol-1 K-1) and T is temperature in Kelvin. The term k_c is the equilibrium stability constant, which was calculated at each temperature using the relation (Eq. 3.2b),

$$k_c = C_s/C_e \quad (3.2b)$$

Where, Cs and Ce are the equilibrium protein concentration on the adsorbent and aqueous phase respectively. The Gibbs free energy changes (ΔG^o) in this temperature range were calculated from Eq. 3.2a. The ΔG^o value of β-lactoglobulin adsorption was -0.874 KJ mol^{-1} at 10°C which increases to -0.177 KJ mol^{-1} with the increase in temperature to 40°C. (Appendix, Figure A3.7c). The negative values of ΔG^o suggest that the adsorption process is spontaneous and thermodynamically favorable.[3.27]

3.3.3.6 Protein tertiary structure analysis by intrinsic tryptophan fluorescence

To study the change in tertiary structure of β-lactoglobulin upon adsorption the intrinsic fluorescence intensity of the protein was analyzed. Fluorescence emission spectra of protein were taken with an addition of increasing NP concentrations. Figure 3.8 shows a steady decrease in the fluorescence intensity upon addition of ZnO NPs in solution. The quenching of fluorescence intensity is due to the alteration in the native structure upon adsorption. β-lactoglobulin contains two tryptophan residues, (Trp19 and Trp61). The Trp19 is buried in the hydrophobic core whereas the latter is exposed to the solvent.[3.28] The characteristic emission maximum of β-lactoglobulin in native solution is at ~343 nm, indicates that the Trp61 is fully exposed to aqueous solvent. The change in intensity can be explained on the basis that strong tryptophan quenching groups such as cysteine are present which rearrange themselves in close spatial proximity upon adsorption.[3.29] However it has been reported that ZnO NPs and Trp moiety forms a ground state complex and the quenching of the fluorescence of β-lactoglobulin is quite likely to result from a complex formation between the β-lactoglobulin and the ZnO NPs.[3.30]

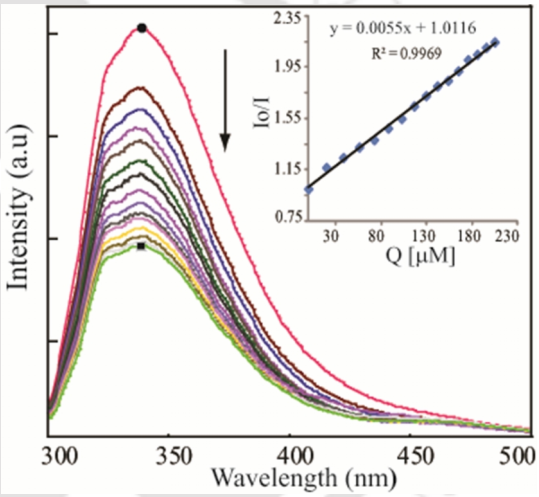

Figure 3.8. Fluorescence quenching spectra of *β*-lactoglobulin upon addition of ZnO NPs (●-blank protein concentration 100 μg ml^{-1} ; 20 μl successive addition of 50 μg ml^{-1} ZnO NPs into 0.6 ml of protein solution ; ■-240 μl addition of ZnO).

3.3.3.7 Fluorescence anisotropy measurement and thermal stability

To ascertain the binding of β-lactoglobulin with ZnO NPs, we measured the fluorescence anisotropy of β-lactoglobulin at different experimental conditions. The fluorescence anisotropy of native β-lactoglobulin free in solution was measured 0.043, which represents a free rotational motion of the fluorophore in the protein molecule. However, upon adding of ZnO NPs the fluorescence anisotropy of β-lactoglobulin increases to 0.135, suggesting the increased rigidity of the surrounding environment of the fluorophore (tryptophan) upon binding on the nanoparticles surface (Figure 3.9). This could be explained on the basis that adsorption of the protein on to the nanoparticles surface implies an imposed motional restriction on the fluorophore (tryptophan) moiety in the protein microenvironment. The anisotropy value almost saturates with further increase in the ZnO concentration, indicates a steady state surface coverage with a fixed alteration in protein conformation.

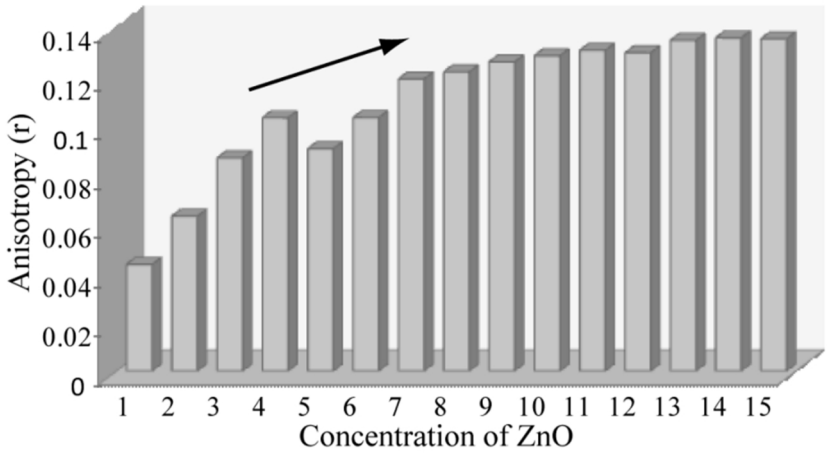

Figure 3.9. Fluorescence Anisotropy plot of β-lactoglobulin upon addition of ZnO NPs (1- blank; 20 μl successive addition of 50 μg ml^{-1} ZnO NPs).

In order to study the changes in the adsorbed protein structure at different temperature we utilized the fluorescence emission spectroscopy to analyze the protein tertiary conformation changes occurring and the ability of the nano-composite to withstand different harsh condition. In this regard, we have monitored the in-situ structural features of native and adsorbed trypsin in a temperature range of 25°C to 70°C under a continuous heating condition. The higher range of temperature (70°C) was chosen in such a way that it does not affect the native protein denaturation in solution, as above 70°C the protein undergoes irreversible conformation changes.[3.31] The emission spectra

of native and adsorbed β-lactoglobulin on ZnO surface under an increasing temperature are shown in Figure 3.10. Similar changes in emission spectra were observed in both the cases, where the emission spectra quenched with a red shift with the increase in temperature from 25°C to 70°C. This indicates a similar partial unfolding behavior of β-lactoglobulin at higher temperature, in both solution and on ZnO surface. These results reveals a more native like structure (less denaturation) of β-lactoglobulin on ZnO surface which directs the suitability of these ZnO nanoparticles as a potential protein carriers. However, in case of emission spectra of the adsorbed β-lactoglobulin an initial steep quench was observed. This might be due to the actual heterogeneous nature of the system due to the presence of nanoparticles, and also considering the fact that the adsorbed protein undergoes a small partial unfolding quickly on the surface of ZnO nanoparticles.

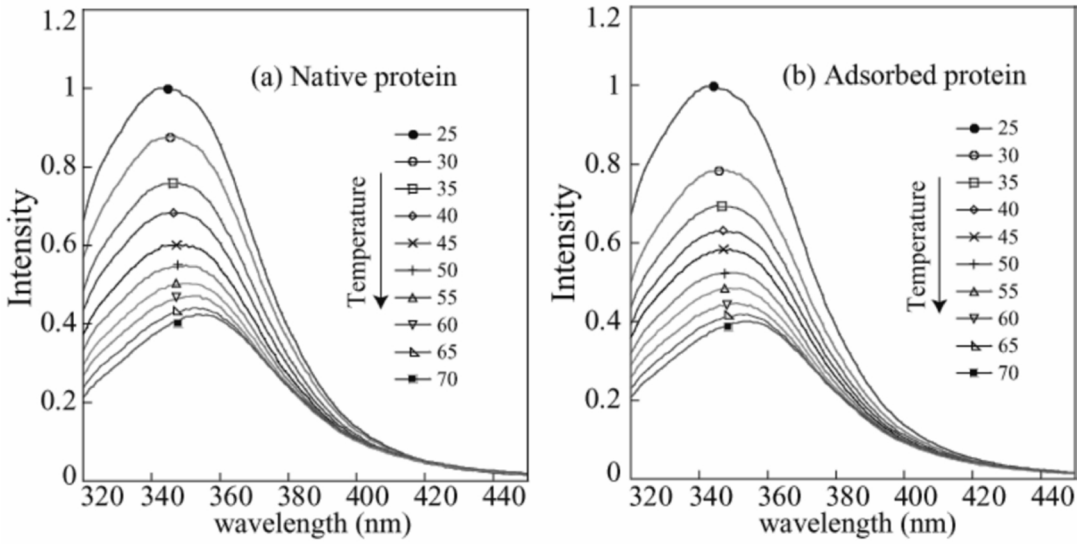

Figure 3.10. Temperature dependent study of native and adsorbed protein from temperature range 25°C to 70°C at 5°C interval.

3.3.3.8 Secondary structure analysis by circular dichroism (CD)

CD spectra of β-lactoglobulin interacting with ZnO NPs were taken in different protein-nanoparticle concentration. Figure 3.11 shows the CD spectra of β-lactoglobulin which are in good agreement with the data reported previously by Wu *et al.*[3.32] The protein exhibits a wide minimum around 218 nm which is a characteristic of β-rich proteins. CD spectra of β-lactoglobulin in solution with those of protein adsorbed on the

nanoparticle surface have been compared in Figure 3.11. Analysis of the CD data was done to calculate the secondary structural elements of the protein. The CD data shows the relative amounts of α-helical, β-sheet and unordered secondary structural elements of the protein in native state and upon adsorption. The obtained values for the secondary structural elements from the CD analysis are summarized in Table 3.3. The (%) value change of α-helical and β-sheet of the native and adsorbed protein reveals that β-lactoglobulin retained its secondary structure almost intact upon adsorption to the nanoparticle surface at even different nanoparticle concentration. This indicates that the β-lactoglobulin was almost stabilized on ZnO surface as obtained. Similar observation was also reported for the behavior of other proteins adsorbed on flat surfaces by previous investigators.[3.33,3.34]

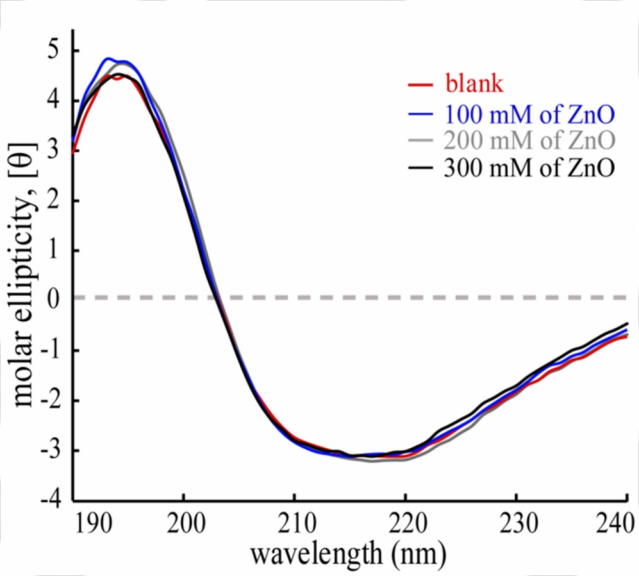

Figure 3.11. CD spectra of β-lactoglobulin, blank and upon addition of ZnO NPs.

Table 3.3. Secondary structural elements of β-lactoglobulin; blank and upon addition of ZnO NPs.

	α helix (%)	**β sheet (%)**	**Others (%)**
Blank protein	13.7	32.4	53.9
100 μM ZnO	13.4	32.6	54.0
200 μM ZnO	13.6	32.3	54.1
300 μM ZnO	13.8	32.1	54.1

3.3.4 Summary

In this work we have demonstrated the morphological selectivity for the fabrication of ZnO NPs using calcination reconstruction of crystalline precursor complex. Solid state transformation of architecturally different Zn(II)-PDC complexes directs to disk-like and rod shaped nanoparticles. The morphology and crystallinity of the as synthesized ZnO NPs have been characterized by various analytical tools. This method has been found to be facile and efficient in discriminating the morphological evolution of ZnO NPs. Furthermore the synthesized ZnO NPs has been found to have differential interaction phenomena with protein β-lactoglobulin. The adsorption capacity (q_e) was high and highly pH dependent. The adsorption kinetics data was well fitted with the second order kinetics and the negative (ΔG^o) values of adsorption process reflect the thermodynamic favorability of the process. Moreover, the conformational analysis reveals a partial unfolding of protein at interface with almost intact secondary structural elements. Thus the facile process of morphologically controlled synthesis of nano-materials and in-depth of differential protein interaction could be a very useful tool in several directions of bio-nanotechnology, biomedical engineering and nano-scale constructs.

Reference

[3.1] S. V. N. T. Kuchibhatla, A. S. Karakoti, D. Bera, S. Seal, Prog. Mater. Sci. 52 (2007) 699-913.

[3.2] Z. L. Wang, Annu. Rev. Phys. Chem. 55 (2004) 159-196.

[3.3] A. D. Goncalves, M. R. Davolos, N. Masaki, S. Yanagida, A. Morandeira, J. R. Durrant, J. N. Freitas, A. F. Nogueira, Dalton Trans. (2008) 1487-1491.

[3.4] M. Law, L. E. Greene, J. C. Johnson, R. Saykally, P. D. Yang, Nat. Mater. 4 (2005) 455-459.

[3.5] C. S. Rout, A. R. Raju, A. Govindaraj, C. N. R. Rao, J. Nanosci. Nanotechnol. 7 (2007) 1923-1929.

[3.6] Y. L. Wu, C. S. Lim, S. Fu, A. I. K. Tok, H. M. Lau, F. Y. C. Boey, X. T. Zeng, Nanotechnology, 18 (2007) 215604-215613.

[3.7] Y. L. Wu, S. Fu, A. I. K. Tok, X. T. Zeng, C. S. Lim, L. C. Kwek, F. Y. C. Boey, Nanotechnology, 19 (2008) 345605-345614.

[3.8] (a) M. L. Kahn, M. Monge, V. Colliere, F. Senocq, A. Maisonnat, B. Chaudret, Adv. Funct. Mater. 15 (2005) 458-468. (b) B. Liu, H. C. Zeng, J. Am. Chem. Soc. 127 (2005) 18262-18268. (c) P. X. Gao, W. J. Mai, Z. L. Wang, Nano Lett. 6 (2006) 2536-2543. (d) P. X. Gao, C. S. Lao, Y. Ding, Z. L. Wang,

Adv. Funct. Mater. 16 (2006) 53-62. (e) C.X. Xu, X. W. Sun, Z. L. Dong, Y. P. Cui, B. P. Wang, Cryst. Growth. Des. 7 (2007) 541-544.

[3.9] (a) T. K. Subramanyam, B. S. Naidum, S. Uthanna, 35 (2000) 1193-1202. (b) X. Zhang, S. Y. Xie, Z. Y. Jiang, X. Zhnag, Z. Q. Tian, Z. X. Xie, R. B. Huang, L. S. Zheng, J. Phys. Chem. B, 107 (2003) 10114-10118. (c) J. Wienke, A. S. Booij, Thin Solid Films, 516 (2008) 4508-4512. (d) A. Umar, S. H. Kim, J. H. Kim, Y. B. Hahn, Mater. Lett. 62 (2008) 167-171. (e) P. Jiang, J. J. Zhou, H. F. Fang, Mater. Lett. 60 (2006) 2516-2521. (f) A. M. Spokoyny, D. Kim, A. Sumrein, C. A. Mirkin, Chem. Soc. Rev. 38 (2009) 1218-1227.

[3.10] H. Kleinwechter, C. Janzen, J. Knipping, H. Wiggers, P. Roth, J. Mater. Sci. 37 (2002) 4349-4360.

[3.11] X. Wu, G. Narsimhan, Langmuir, 24 (2008) 4989-4998.

[3.12] A. J. Reddy, M. K. Kokila, H. Nagabhushana, J. L. Rao, C. Shivakumara, B. M. Nagabhushana, R. P. S. Chakradhar, Spectrochimica Acta Part A, 81 (2011) 53-58.

[3.13] H. Noei, H. Qiu, Y. Wang, E. Löffler, C. Wöll, M. Muhler, Phys. Chem. Chem. Phys. 10 (2008) 7092-7097.

[3.14] L. S. Wong, F. Khan, J. Micklefield, Chem. Rev. 109 (2009) 4025–4053.

[3.15] I. Lynch, K. A. Dawson, S. Linse, Sci. STKE 14 (2006) p.pe 14.

[3.16] S. Chakraborti, T. Chatterjee, P. Joshi, A. Poddar, B. Bhattacharyya, S. P. Singh, V. Gupta, P. Chakrabarti, Langmuir, 26 (2010) 3506-3513.

[3.17] Y. Zhai, S. Zhai, G. Chen, K. Zhang, Q. Yue, L. Wang, J. Liu, J. Jia, J. Electroanal. Chem. 656 (2011) 198-205.

[3.18] A. Kathiravan, G. Paramaguru, R. Renganathan, J. Mol. Struct. 934 (2009) 129-137.

[3.19] Q. Husain, S. A. Ansari, F. Alam, A. Azam, Int. J. Biol. Macromol. 49 (2011) 37-43.

[3.20] J. Cerbulis, H. M. Jr.Farrell, J. Dairy Sci. 58 (1975) 817-827.

[3.21] K. Kuwata, M. Hoshino, V. Forge, S. Era, C. A. Batt, Y. Goto, Protein Sci. 8 (1999) 2541-2545.

[3.22] E. W. Blanch, L. Hecht, L. D. Barron, Protein Sci. 8 (1999) 1362-1367.

[3.23] C. Tanford, L. G. Bunville, Y. Nozaki, J. Am. Chem. Soc. 81 (1959) 4032-4036.

[3.24] M. H. Kalavathy, T. Karthikeyan, S. Rajgopal, L. R. Miranda, J. Colloid Interface Sci. 292 (2005) 354-362.

[3.25] S. Lagergren, Handlingar, 24 (1898) 1-39.

[3.26] J. Wen, X. Han, H. Lin, Ying. Zheng, W. Chu, Chem. Eng. J. 164 (2010) 29-36.

[3.27] S. Chen, Q. Yue, B. Gao, X. Xu, J. Colloid Interface Sci. 349 (2010) 256-264.

[3.28] K. Sakurai, T. Konuma, M. Yagi, Y. Goto, Biochimica et Biophysica Acta. 1790 (2009) 527-537.

[3.29] B. M. Borah, B. Saha, S. K. Dey, G. Das, J. Colloid Interface Sci. 349 (2010) 114-121.

[3.30] G. Mondal, S. Bhattacharya, T. Ganguly, Chem. Phys. Lett. 472 (2009) 128-133.

[3.31] D. Fessas, S. Iametti, A. Schiraldi, F. Bonomi, Eur. J. Biochem. 268 (2001) 5439-5448.

[3.32] L. Wu, Y. Wu, W. Lu, Physica E, 28 (2005) 76–82.

[3.33] P. Billsten, P. O. Freskgard, U. Carlsson, B. H. Jonsson, H. Elwing, FEBS Lett. 402 (1997) 67-72.

[3.34] A. A. Vertegel, R. W. Siegel, J. S. Dordick, Langmuir, 20 (2004) 6800-6808.

Appendix

A3.1 Experimental details for solving the crystal.

In each case, a crystal of suitable size was selected from the mother liquor and immersed in silicone oil, then mounted on the tip of a glass fibre and cemented using epoxy resin. Intensity data for the crystals were collected Mo-Kα radiation (λ = 0.71073Å) at 298(2) K, with increasing ω (width of 0.3° per frame) at a scan speed of 6 s/frame on a Bruker SMART APEX diffractometer equipped with CCD area detector. The data integration and reduction were processed with SAINT software.[A3.1] An empirical absorption correction was applied to the collected reflections with SADABS (SADABS 1999).[A3.2] The structures were solved by direct methods using SHELXTL and were refined on F^2 by the full-matrix least-squares technique using the SHELXL-97 program package.[A3.3, A3.4] Graphics were generated using MERCURY 2.3.[A3.5] In all cases, non-hydrogen atoms are treated anisotropically and hydrogen atoms attached to all carbons are geometrically fixed and refined isotropically.

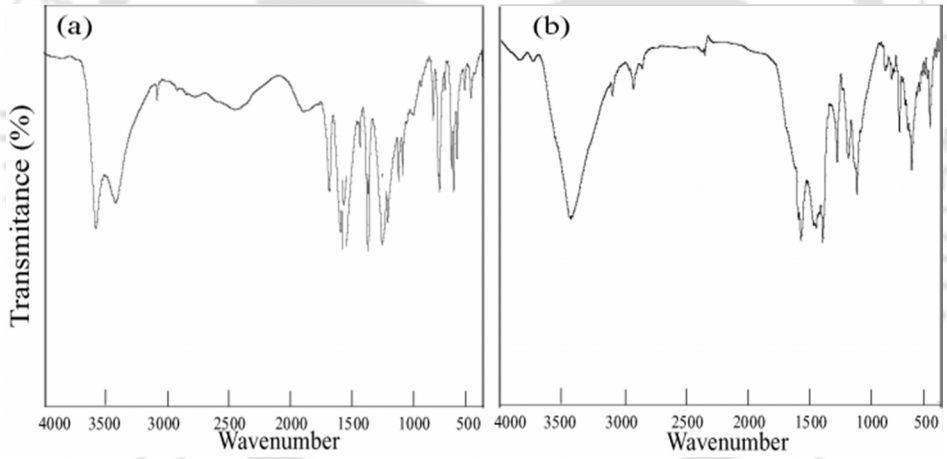

Figure A3.1. IR-plot of (a) Complex **1** and (b) Complex **2**.

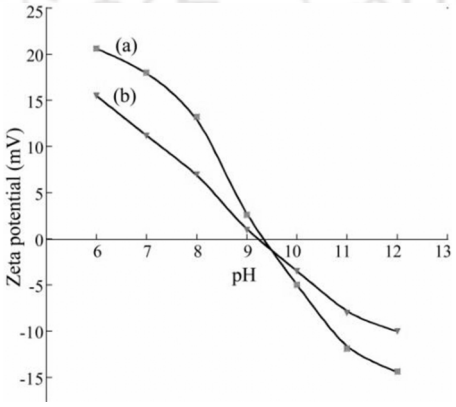

Figure A3.2. ζ-Potential measurement of (a) disk-like ZnO and (b) ZnO nanorods.

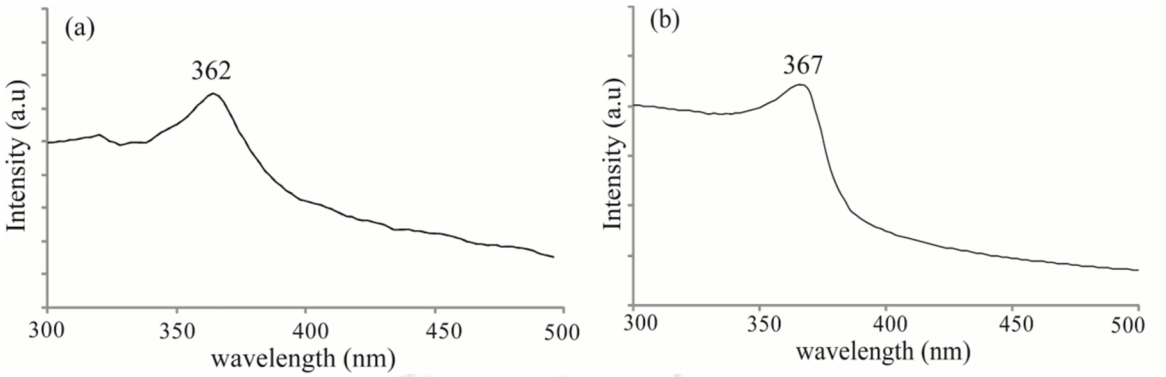

Figure A3.3. UV-Vis spectra of ZnO nanoparticles (a) disk-like and (b) nanorods.

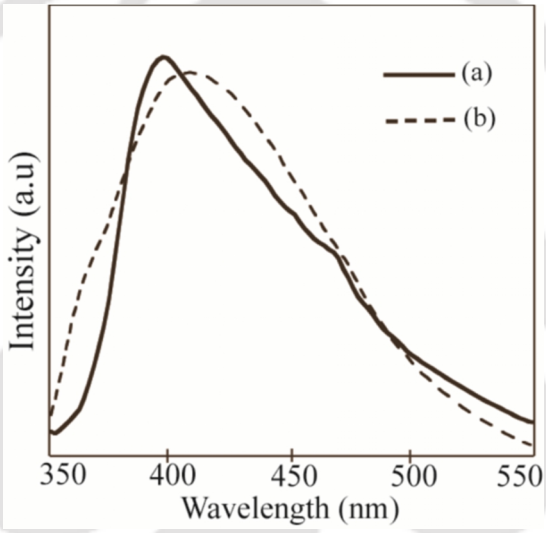

Figure A3.4. PL spectra of ZnO nanoparticles (a) disk-like and (b) nanorods.

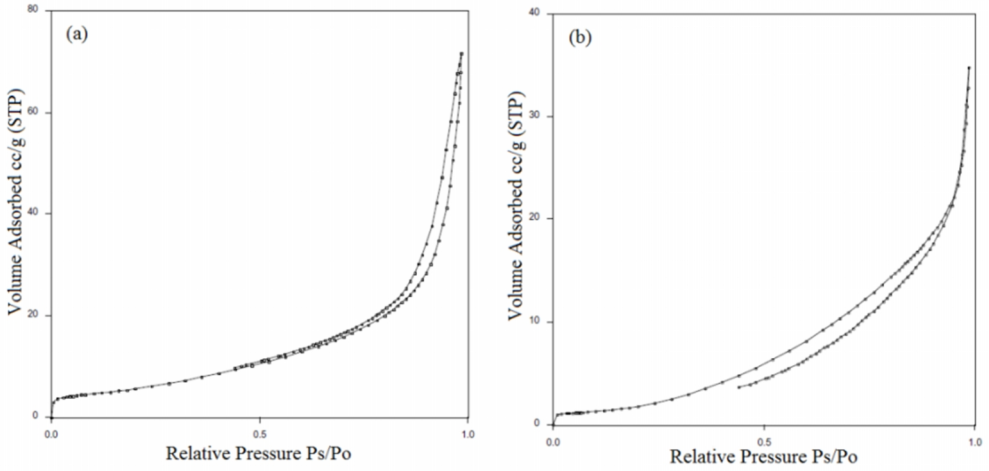

Figure A3.5. Nitrogen adsorption plot for BET surface area measurement (a) disk –like ZnO and (b) ZnO nanorods.

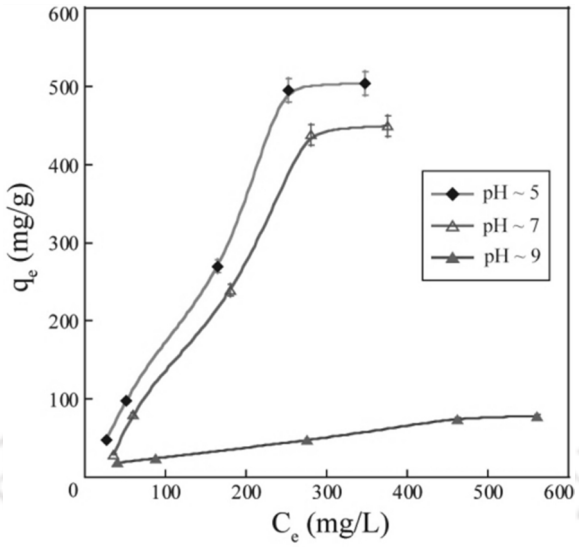

Figure A3.6. Adsorption isotherm plot at different pH.

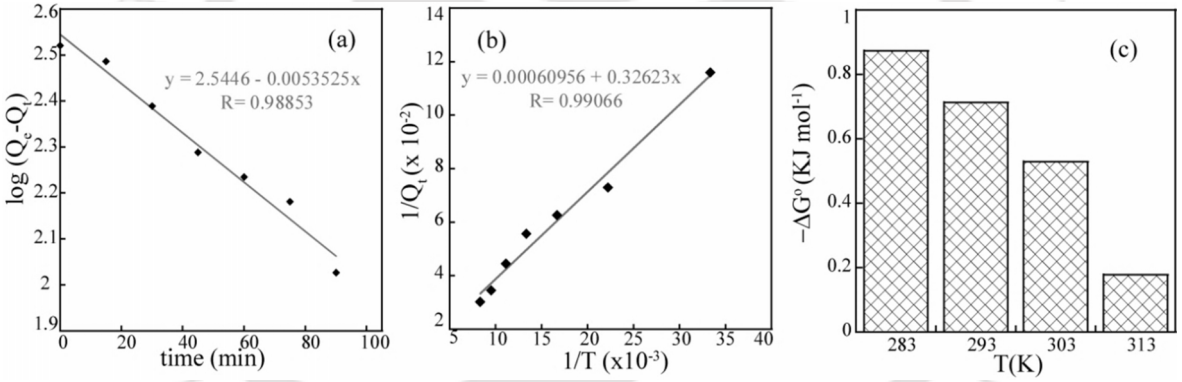

Figure A3.7. (a) 1st order kinetic model plot; (b) 2nd order kinetic model plot and (c) Gibb's free energy change (ΔG^o) vs temperature plot.

References

[A 3.1] Mercury 2.3, Supplied with Cambridge Structural Databse; CCDC: Cambridge, U,K,.

[A 3.2] Sheldrick, G. M. SADABS: Software for Empirical Absorption Correction; University of Gottingen, Institute fur Anorganische Chemieder Universitat: Gottingen, Germany, 1999-2003.

[A 3.3] Sheldrick, G.M. SHELXS-97;University of Gottingen: Germany,1997.

[A 3.4] Sheldrick, G. M. SHELXL-97: Program for Crystal Structure Refinement; University of Gottingen, Gottingen, Germany, 1997.

[A 3.5] SMART, SAINT and XPREP; Siemens Analytical X-ray Instruments Inc.: Madison, WI, 1995.

Chapter 4

ZnS-Protein interaction

Chapter 4

4.1 Introduction

Progressing from the interaction study of protein with a basic 'hard' surface in the previous chapter, this chapter deals with the interaction study of proteins with an acidic 'soft' surface. Nanoparticles of Zinc Sulfide (ZnS), an acidic 'soft' sulfide mineral have been extensively used for the interfacial interaction study of two proteins, bovine serum albumin (BSA) and β-lactoglobulin (BLG). A detailed comparative study of interaction of both the proteins upon adsorption onto ZnS surface has been reported here.

4.2 Synthesis and characterization of ZnS nanoparticles

A simple precursor mediated synthesis has been used for the synthesis of ZnS NPs. In a usual synthesis procedure, aqueous solution of PDC (5.6 mmol, 0.954 gm) was added drop-wise to the aqueous solution of $Zn(OAc)_2.2H_2O$ (2.8 mmol, 0.626 gm) with constant stirring at room temperature for a period of 6 hrs. White precipitate thus formed was filtered, washed with water and dried in vacuum. The complex was made soluble adding few drops of aniline. H_2S gas was purged through the solution to give a white colloidal suspension which on centrifugation yielded white precipitates of ZnS NPs. The precipitate was washed with methanol, water and vacuum dried prior to characterization.

ZnS NPs synthesized were characterized by several techniques. The TEM image in Figure 4.1a confirms the formation of nearly mono-dispersed nanospheres of sizes~100 nm in copious quantity. The X-ray powder diffraction of ZnS NPs (Figure 4.1b) showing reflections from (111), (220) and (311) planes are in agreement with the formation of zinc blende (cubic, β-ZnS) structure (JCPDS No. 01-0792). The FTIR spectra also support the formation of ZnS nanoparticles (Appendix, Figure A4.1). The BET surface area analysis from the N_2 adsorption desorption isotherm reveals the high surface area of the synthesized ZnS nanoparticles to be 141.69 m^2/g (Appendix, Figure A4.2). From the zeta potential data it reveals that the PZC (point of zero charge) of the ZnS to be around pH~3.7 (Figure 4.1c). The emission spectra of ZnS NPs has also been given in the Appendix section (Appendix, A4.3).

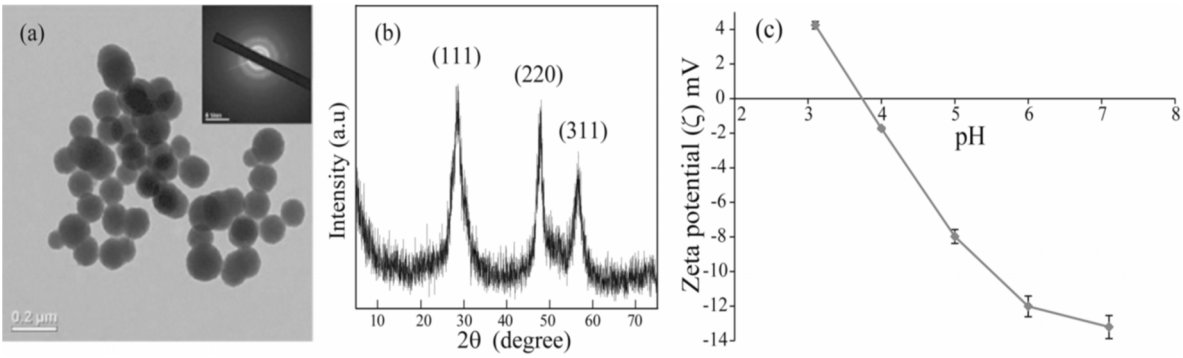

Figure 4.1. (a) TEM, (b) PXRD and Zeta potential (ζ) plots of ZnS nanoparticles.

4.3 Interaction study with protein

4.3.1 Background

Protein adsorption is the *prima facie* credibility in the construct of bio-nano composite for implication in various fields. It is a complex process involving various factors such as van der Waals, hydrophobic and electrostatic interactions, and hydrogen bonding.[4.1] On the other hand, different proteins act differently with the introduced surface in the adsorption process depending on their physio-chemical and structural stability. Structural reorientation (both secondary and tertiary) is always accompanied by the adsorption for most of the protein whilst some appears to resist significant conformational change.[4.2,4.3] This sort of conformational flexibility and conformation rigidity of proteins classified them into class of "soft" and "hard" proteins. Proteins that have a tendency to undergo major surface-induced conformational change are termed as "soft" and those less vulnerable to conformational change are coined as "hard" protein.[4.4,4.5] Based on this property of protein, different proteins ("soft" and "hard") are likely to show different adsorption behavior after adsorption onto same surface. A lot of studies have been made to understand how "soft" and "hard" proteins interact with different surface. Norde *et al*. investigated the structural perturbation of lysozyme (hard) and α–lactalbumin (soft) on negatively charged polystyrene latex (PS^-) and variably charged hematite (α-Fe_2O_3) surfaces.[4.6] Norde *et al*. also studied the change in secondary structural component of BSA (soft) and lysozyme (hard) upon adsorption onto finely dispersed silica particle.[4.7] Turci *et al*. elaborated the consequence of adsorption of four proteins:BSA (soft), lysozyme (hard), bovine pancreatic ribonuclease (hard) and bovine lactoperoxidase (soft), onto two amorphous pyrogenic silica

nanoparticles.[4.8] Further, Wertz *et al*. substantiated that lysozyme, despite its recognized "hardness" on hydrophilic surfaces, compromises its structural integrity upon adsorption onto hydrophobic surfaces.[4.9] Cole *et al*. found the well-structured molecule of collagen undergoes structural perturbations when interacting with the hydrophilic SiO_2 surface, but it weakly interacts with a hydrophobic derivative of the same surface, which may be explained by its rigid molecular structure.[4.10] From the above observation it could be concluded that the consequences of adsorption is a very complex phenomenon and is very difficult to predict how a "soft" or "hard" protein would behave to a given surface.

To quench our inquisitiveness of knowing the adsorption process better, we have taken two different protein having near same isoelectric point (IEP) but different structural stability for the adsorption interaction study. Two globular, highly abundant proteins, Bovine serum albumin (BSA) and *β*-lactoglobulin (BLG) were taken as model protein for the study. The main properties of the two proteins are summarized in Table 4.1 to get a brief idea about the proteins. Serum albumin is the most abundant protein in mammalian plasma and BSA (Bovine Serum Albumin) is the most studied serum protein due to its wide availability, low cost and high structural resemblance with HSA (Human Serum Albumin).[4.13] BSA is a water-soluble monomeric protein of single polypeptide chain with 583 amino acid residues and a molar mass of 66.4kDa.[4.14] BLG is also one of the most extensively studied proteins due to its high abundance in cow's milk.[4.15] At neutral pH BLG exists as a non-covalent dimer consisting of two identical monomers of molecular mass 18.3 kDa. Table 4.1 summarizes the physio-chemical properties of the two proteins.

In continuation to our previous work of protein nanoparticle interaction study in Chapter 3, herein we focus to see the effect of the adsorption of the two proteins (BSA and BLG) on to the surface of ZnS nanoparticle (NPs). ZnS NPs of size ~100 nm and having a high specific surface area of 141.69 m^2 g^{-1} was taken as the substrate for the adsorption at pH 7. ZnS having PZC (point of zero charge) value around pH~3.7, retains a negative surface at the study regime, likewise the proteins also possess a net negative charge at this pH point. We have incorporated various experimental approaches such as zeta (ζ) potential, fluorescence and CD for analyzing the adsorption process. From the experimental results and based on the physio-chemical nature of the proteins and ZnS NPs, we have tried to draw a plausible conclusion of the adsorption system.

Table 4.1. Properties of the proteins BSA and BLG taken for the study.[4.11,4.12]

Protein	Isoelectric point (IEP)	Molecular mass (Da)	Resistance to deformation (hard/soft)	Dimension (nm)	Net charge at pH 7	Zeta potential (ζ) mV
BSA	4.9	68,000	Low (soft)	9.0×6.0×5.0	Negative	-14.6
BLG	5.1	18,300	High (hard)	6.5×3.6×3.6	Negative	-19.5

4.3.2 Materials and methods

Protein. A buffer solution, consisting of 50 mM sodium phosphate at pH 7, was used in all the experiments. Adsorption experiments of protein onto ZnS NPs were carried out in batch mode. The concentration of the protein was varied from 10-500 μg ml^{-1} and ZnS NPs concentration was kept constant at 0.5 μg ml^{-1}.

Fluorescence emission spectroscopy. The protein was excited at 295 nm and tryptophan emission fluorescence spectra were collected from 300-500 nm. We have done the fluorescence titration of the protein with the continuous addition of aliquots of ZnS NPs into the protein solution. The ZnS NPs concentration varied from 3.3 μM to 31.1 μM whereas a 50 μg ml^{-1} concentration of protein was taken. Steady state anisotropy was also measured in the same instrument.

Circular Dichroism (CD). CD spectra of native and adsorbed protein were measured to evaluate the secondary structural change. Four different concentrations of ZnS were taken for CD spectral analysis. The concentration of protein was 50μg ml^{-1} and final ZnS NPs concentration was 10, 25, 50 and 100 μM respectively. Phosphate buffer concentration of 50 mM was used for this study.

Zeta potential. Zeta potential (ζ) analysis of ZnS NPs and interaction system of the two proteins with the nanoparticles were measured at different protein coverage. Samples were re-dispersed and diluted in 10 mM phosphate buffer and titrated with 0.1 M NaOH and 0.1 M HCl using the auto titrator, and circulated simultaneously in the analytical cell for zeta potential measurement. The temperature of the scattering cell was fixed at 25^{o}C.

4.3.3 Adsorption interaction study

4.3.3.1 Surface coverage and Adsorption Isotherm

The resulting measurements of protein surface coverage for BSA and BLG are shown in Figure 4.2. Substantial adsorption was found at pH 7 where both the surface and proteins were negatively charged. In both the cases of BSA and BLG, the surface coverage increased with an increase in protein concentration. The theoretical *"side-on"* monolayer was calculated considering the (RSA) random sequential adsorption model which considers 55% of the surface covering, to see the relative surface covering of the ZnS NPs surface. The theoretical *"side-on"* monolayer for BSA was calculated to be ~169 ng cm^{-2} and for BLG it was ~71.5 ng cm^{-2}. The surface coverage for BSA varied from a minimum of 7.19 ng cm^{-2} to maximum coverage of 251.8 ng cm^{-2} and that for BLG ranged from 2.47 to 103.2 ng cm^{-2}. This higher value of adsorption might be due to the porous nature of the ZnS NPs which can accommodate higher number of protein in its pore areas and also into the available surface area.

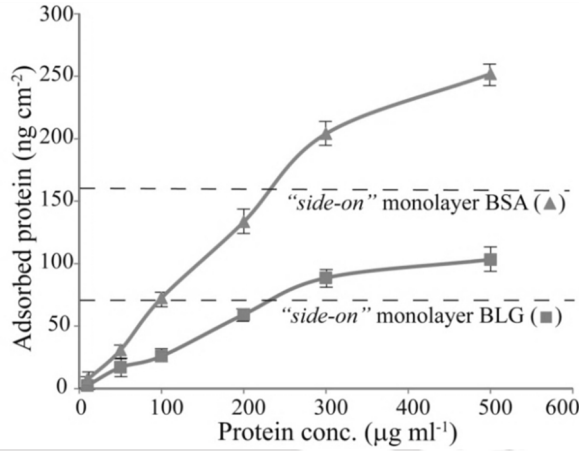

Figure 4.2. Protein adsorption isotherms plotted as a function of initial protein concentration at pH 7. The dotted horizontal lines indicate the calculated amount of proteins needed for "side-on" adsorption modes to cover the surface area with one monolayer**.**

4.3.3.2 Zeta potential (ζ) variation and protein coverage

The adsorption of the proteins onto the ZnS surface brings about a modification of the surface net charge which alters the ζ potential value.[4.16] Figure 4.3 depicts the profile of the change in the ζ potential value as a function of pH, at various protein surface coverage. For all the cases, the surface chemistry of the protein-nanoparticle composite changed with increasing surface coverage. With the extent of adsorption, the surface of ZnS NPs get masked by the proteins and the characteristic of the surface starts to deviate towards the IEP of the protein. This deviation was more prominent with the increase in protein concentration. The IEP of naked ZnS surface was around pH 3.7

whereas BSA and BLG have IEP values close to pH ~ 5 (~ 4.9 for BSA and ~ 5 for BLG see Appendix, Figure A4.4). The IEP of the conjugates (BSA/ZnS and BLG/ZnS) was found to be very near to the IEP of the corresponding proteins (but never overlapped). For BSA/ZnS composite the IEP was around pH 4.5 at a low surface coverage of 0.30 mg m^{-2} and increased to pH 4.78 at a higher surface coverage of 2.51 mg m^{-2}. Similar trend was observed for the BLG/ZnS conjugate with IEP of about pH 4.4 at a lower surface coverage of 0.16 mg m^{-2} and pH 4.81 at a higher surface coverage of 1.03 mg m^{-2}. The maximum adsorption values of both the proteins exceeded the theoretical *"side-on"* monolayer value for both the proteins whilst the zeta potential values never leveled to the IEP of the proteins. These two findings lead to a probable conclusion that the high porous nature of ZnS NPs accommodates a higher fraction of proteins into it. Thus increasing the adsorption value and the complete masking of the ZnS NPs surface never happened.

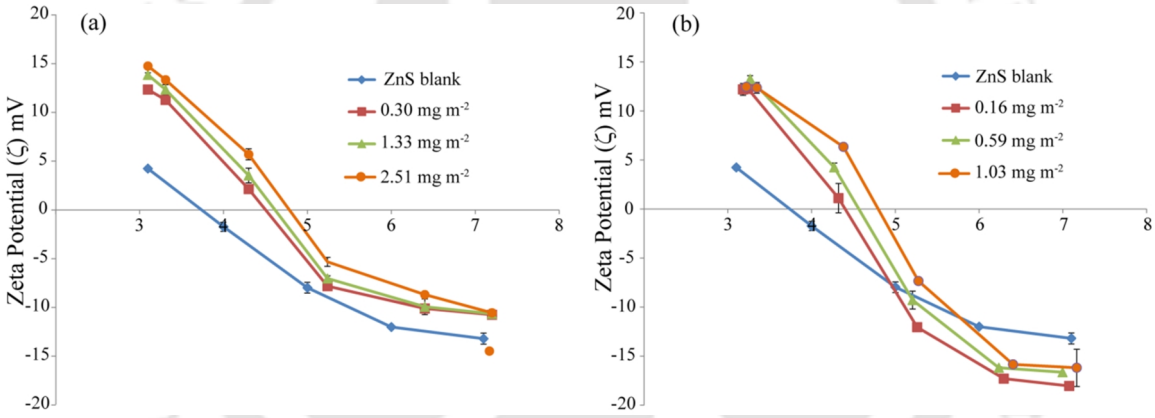

Figure 4.3. ζ Potential measurement of pure ZnS nanoparticles and protein coated ZnS nanoparticles at different surface coverage.

4.3.3.3 Tryptophan fluorescence quenching and anisotropy measurement

The quenching of fluorescence emission originates either from static or dynamic interaction of quencher with the fluorophore. In order to get an insight of the quenching mechanism of the proteins (BSA and BLG) with ZnS, we have monitored the emission of tryptophan residues in the protein solution at different concentrations of the quencher (ZnS). BSA has two Trp residues at positions 134 and 212 which are responsible for the intrinsic fluorescence. Trp212 residue is located in hydrophobic cavity, whereas Trp134 is located on the surface. The binding close to these can alter the fluorescence intensity of the species.[4.17] BLG also has two Trp unit (Trp19 and Trp61). The Trp19 is buried in the hydrophobic core whereas the latter is exposed to the solvent.[4.18] The fluorescence

intensity was found to decrease gradually with the increase in the quencher concentration and shown in Figure 4.4. We have further employed the classical Stern–Volmer equation for the fluorescence intensity data to calculate the Stern–Volmer constant.[4.19]

$$I_o/I = 1 + K_{sv}[Q] \quad (4.2)$$

where, I_o and I are the fluorescence intensities of protein in the absence and presence of the quencher, respectively. K_{sv} is the Stern–Volmer constant and [Q] is the concentration of the quencher (ZnS in this case). The K_{sv} values obtained from the equation are summarized in Table 4.2. Moreover, the di-molecular quenching equation is

$$K_{sv} = K_q \tau_0 \quad (4.3)$$

where, K_q represents the quenching rate constant and τ_0 is the average photoluminescence lifetime of protein (usually $\sim 10^{-8}$ to $\sim 10^{-9}$ for BSA and BLG respectively).[4.20,4.21] The K_q value lies in the range of $\sim 10^{12}$ to $\sim 10^{13}$ (L mol^{-1} s^{-1}) for both BSA and BLG, which is far greater compared with the value obtained for biological macromolecules due to the collision mechanism (2.0×10^{10} L mol^{-1} s^{-1}) implying the static nature of the quenching process.[4.22] Using the method described by Shao *et al*., one can calculate the number of binding sites (*n*), and the binding constant (K_b) using the equation

$$\log (I_0 - I)/I = \log K_b + n \log[Q] \quad (4.4)$$

where, I_0 and I are the fluorescence intensities of protein in the absence and presence of the quencher and [Q] is the concentration of the quencher. The binding constant values and number of binding sites are enlisted in the Table. 4.2.

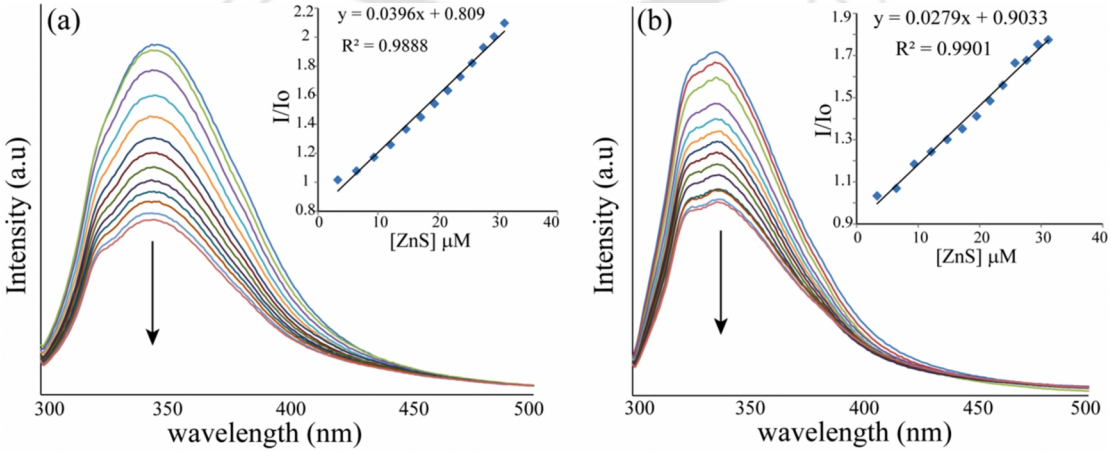

Figure 4.4. Fluorescence quenching spectra of tryptophan residues of (a) BSA and (b) BLG upon addition of ZnS nanoparticles at pH 7. (Inset: Stern-Volmer plot derived from the quenching data).

Fluorescence anisotropy measurement was incorporated to establish the relative binding of proteins with ZnS NPs. The fluorescence anisotropy of free native protein in solution represents a free rotational motion of the fluorophore in the protein molecule which was measured to be ~0.0502 and ~0.0817 for BSA and BLG respectively. However, upon adding of ZnS the fluorescence anisotropy of both the proteins increased (0.2331 for BSA and 0.1975 for BLG), suggesting the increased rigidity of the surrounding environment of the fluorophore (tryptophan) upon binding onto the ZnS surface (Appendix, Figure A4.5). Adsorption of the protein on to the ZnS surface implies an imposed motional restriction on the fluorophore (tryptophan) moiety in the protein microenvironment.

Table 4.2. Experimental observation of the parametrs of the proteins (BSA and BLG) upon interaction with ZnS NPs.

Proteins	Observations from fluorescence data				
	K_{sv}(L mol^{-1}) × 10^4	R^2	K_b(L mol^{-1}) × 10^6	n	R^2
BSA	3.96 ± 0.05	0.9888	7.90 ± 0.12	1.5 ± 0.003	0.999
BLG	2.79 ± 0.02	0.9901	0.32 ± 0.07	1.2 ± 0.01	0.993

4.3.3.4 Structural changes from Circular Dichroism (CD) spectral analysis

The adsorption of proteins onto solid surface is usually accompanied by the change in their secondary structure. The entropy gain of this conformational change may be the driving for the adsorption. To evaluate such secondary structural change in the adsorption of BSA and BLG onto ZnS NPs, we have incorporated CD analysis. CD is a very powerful and sensitive technique for evaluating conformational changes in protein, on binding to nanoparticles.[4.23] Different proteins have peak profiles which are the characteristics of secondary structural elements present in them. BSA contains predominantly α-helices as secondary structural elements, which shows strong negative signals at 208 and 222 nm, characteristics of α-helical structure. Any change in these bands will specify conformational change in the native structure of the protein.[4.24] Whereas, BLG is a β-rich protein exhibiting a wide minimum around 218 nm which is a characteristic of β-rich proteins.[4.25] Figure 4.5 depicts the CD profile of BSA and BLG upon the gradual addition of ZnS at pH 7.

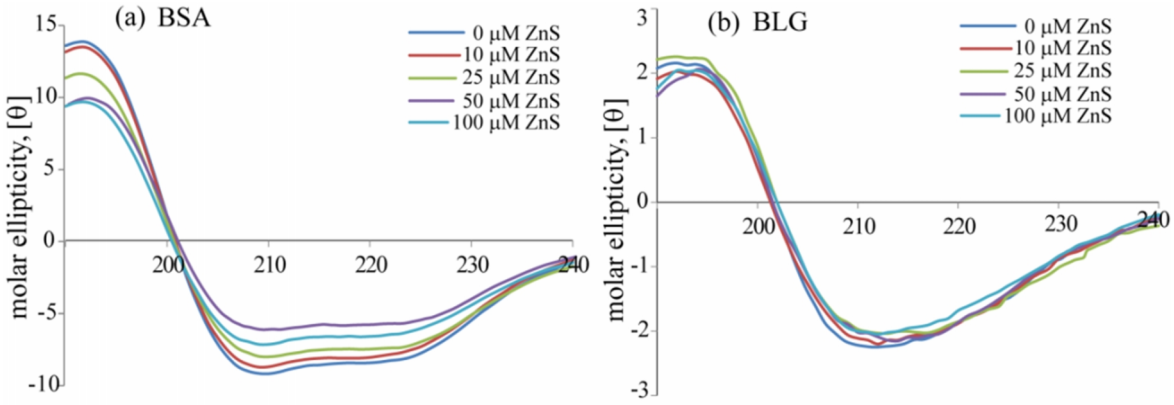

Figure 4.5. CD spectra of (a) BSA and (b) BLG upon addition of ZnS nanoparticles at pH 7.

The structural deviation was more pronounced in case of BSA upon the addition of ZnS, compared to BLG (data are summarized in Table 4.3). The α-helical content decreased for BSA at the expense of the increment in the β–strand and random (turns and unordered) fraction. A total of 9.6 % decrease in the α-helical content was observed for BSA upon addition of 100 μM ZnS NPs. A gradual decrease in the α-helical content and subsequent increase in the β–strand (~5.8%) and random fraction (~3.8%) content was observed upon increasing the concentration of ZnS NPs. On the other hand, the secondary structural elements for BLG were less altered upon the adsorption onto the ZnS NPs surface compared to the BSA. Although a subtle decrease in the α-helical content (of ~ 3%) was observed at the expense of the β–strand (~2.5% increment) but the random fraction was not induced much. These results are in agreement with the known susceptibility of BSA and BLG to conformational changes.

Table 4.3. CD spectra of (a) BSA and (b) BLG upon addition of ZnS NPs at pH 7.

(a)	*α–helix*	*β–strand*	*Random*
BSA	43.8	14.1	42.1
BSA+10 μM ZnS	40.8	14.3	42.9
BSA+25 μM ZnS	36.8	19.3	43.9
BSA+50 μM ZnS	35.7	19.0	45.3
BSA+100 μM ZnS	34.2	19.9	45.9

(b)	*α–helix*	*β–strand*	*Random*
BLG	14.3	32.4	53.3
BLG+10 μM ZnS	13.1	33.8	53.1
BLG+25 μM ZnS	12.6	33.5	53.8
BLG+50 μM ZnS	11.6	34.5	53.9
BLG+100 μM ZnS	11.3	34.9	53.8

4.3.3.5 Evaluating the reversibility of the adsorption

To evaluate the reversibility of the adsorption process we have incubated the ZnS-protein conjugate obtained after adsorption for 10 μg ml^{-1} and 0.5 mg ml^{-1} ZnS, in pure buffer solution. The obtained ZnS-protein conjugate was washed with buffer prior to the study. The availability of protein in the solution due to desorption of the protein from the ZnS NPs surface was monitored with time. Figure A4.6 (Appendix, Figure A4.6) gives the overview of the dynamics of desorption process for BSA and BLG from ZnS surface. Both BSA and BLG were irreversibly bound to the ZnS NPs surface. The increment in the solution protein concentration with time justifies this assumption. A small fraction of protein (BSA and BLG both) was irreversibly attached to the NPs surface and were not detached from the NPs surface within our study condition of 2h. BSA was desorbed slower compared to BLG. The structural rearrangements of BSA might be the cause behind this observation, although this fact could not be confirmed by the data obtained in the present study. The more deformation of the structure of BSA would have attenuated the desorption process.

4.3.4 Rationalization of observation

Substantial amount of adsorption was seen for BSA and BLG at pH 7, where both the proteins and the ZnS NPs surface were negatively charged and electrostatic repulsion was expected. The surface of protein contains different ionizable groups (carboxyl groups and the amino groups) which are ionized at different pH. The net charge the protein carries at a definite pH is governed by the number of ionized carboxyl or the amino groups they possess. These ionized groups form local positive and negative charge regimes within the protein molecule. These local positively and negatively charged regimes on the protein surface could be involved in the adsorption mechanism,

although the net charge suggests an electrostatic repulsion.[4.26] The zeta potential data also accounts for the substantial adsorption of BSA and BLG onto ZnS NPs surface. All the IEPs of the protein treated ZnS NPs suspensions were shifted towards the IEPs of the adsorbed proteins. Although the IEP of the protein-NPs composite never leveled to the IEP of the native proteins. From the calculation of the adsorption capacity it was also found that the maximum surface coverage value for BSA and BLG, was above the theoretical monolayer (*side-on*) calculation value. These two results combined together fetches the conclusion that the highly porous ZnS NPs can accommodate a high amount of proteins into its pores which in turn increases the adsorption value, while complete masking of the ZnS NPs surface do not happen in both cases of BSA and BLG adsorption, leaving to the exposure of ZnS patches and non-overlapping of the IEP values of protein and protein-NPs composite. Similar sort of heterogeneous distribution of protein on hydrophilic surface at pH where all the species were of same charge was reported by Rabe *et al*., even though they showed the co-operativity effect for the outcome.[4.27]

From fluorescence quenching at wavelength ~345 nm, it was established that the tertiary structure of both BSA and BLG was partially altered upon the adsorption onto ZnS NPs. An insight into the protein residual structure can throw some light upon the quenching mechanism of the two. BSA has two tryptophan moieties, Trp residues at positions 134 and 212. Trp212 residue is located in hydrophobic cavity, whereas Trp134 is located on the surface. The quenching could be attributed to both Trp134 and Trp212 interacting with the ZnS NPs. But from the secondary structural analysis (CD spectra) it was substantiated that BSA undergoes a significant structural reorientation. This could probably lead to the Trp212, residing in the hydrophobic pocket to bulge and significantly interact with the ZnS surface resulting the fluorescence quenching. The binding constant K_b was calculated to be 7.9×10^6 L mol^{-1} and number of the binding sites was ~1.5. This structural re-adjustment of BSA for maximizing the accommodation onto the ZnS surface could also justify the higher adsorption value. BLG also showed some tertiary structural change upon adsorption. The magnitude of the interaction of the tryptophan moiety with ZnS NPs was less compared to the BSA. BLG contains two tryptophan residues at 19 and 61. The Trp19 resides in the hydrophobic core and Trp61 protrudes into the surface and sits quite close to the Cys66 to Cys160 di-sulfide bridge. The Cysteine residues could be an effective Trp fluorescence quencher. Thus the intrinsic fluorescence of BLG is attributed to Trp19.[4.28]

The quenching of fluorescence could rise from the binding of Trp19 with the ZnS or the Trp61. Although Trp61 has some contribution but the Trp19 contribute more to the total seen quenching value. For the Trp19 to have an effective interaction it needs to come to the vicinity of the ZnS surface from the hydrophobic pocket. From the secondary structure analysis a very less structural change (~3% decrease in the α-helical content at the expense of ~2.5% increment in the β–strand) was observed. This subtle change in the structure could induce the Trp19 to interact efficiently resulting the quenching. Figure 4.6 is the cartoon representation of BSA and BLG showing the Trp residues. From the figure it is quite clear that, even though the Trp19 of BLG is in the hydrophobic cavity but it is more accessible than the Trp212 of the BSA. Hence with the less deformation a significant interaction could be achieved for BLG where BSA undergoes a high deformation for achieving the same. The anisotropy value also support the strong interaction of BSA over BLG onto ZnS NPs.

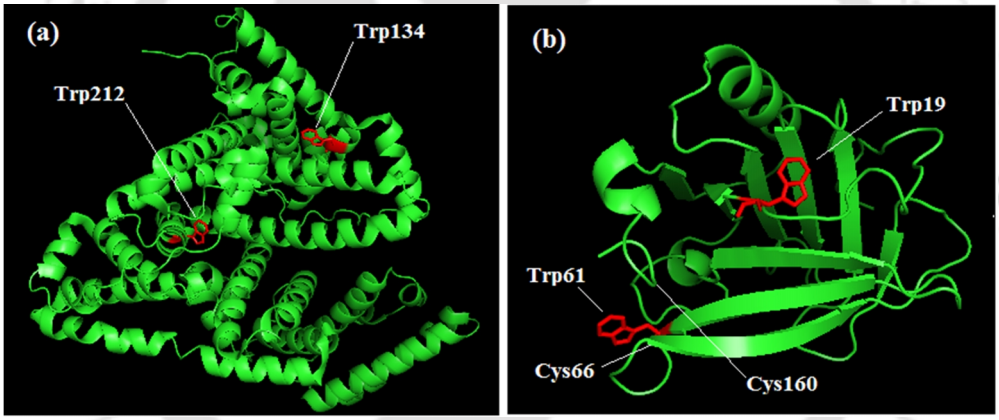

Figure 4.6. Cartoon representation of (a) BSA and (b) BLG showing the relative positioning tryptophan residues at pH 7. (BSA pdb code: 3V03 and BLG pdb code: 3BLG was used. The structure was made using pyMol).

Thus, compiling the results an assumption could be drawn to get the overview of the adsorption phenomenon. The chemical–physical characteristics of the ZnS surface and protein structure decide the relative predominance of the force responsible for the adsorption. At pH 7 the electrostatic attraction could be ruled out to some extent, as all the surfaces are negatively charge. Similar protein–particle adsorption under non-attractive electrostatic conditions were also found on hydrophobic surfaces and reported in the literature.[4.29,4.30] The hydrophobic nature of the ZnS NPs could induce some hydrophobic interaction for BSA and BLG adsorption. BSA showed higher adsorption compared to BLG. Higher adsorption of BSA despite electrostatic repulsion is attributed

to increase in entropy resulting from perturbations in the relatively ‘‘soft’’ α-helical structure of serum albumin.[4.31] On the other hand, BLG probably interacted with the negative surface of ZnS NPs with the positive patches on its surface. Similar sort of interaction of the positive and negative patches of the protein surface involving interaction are reported in the literature [27]. Also, proteins adsorbing at positively or negatively charged interfaces tend to expose oppositely charged regions to the surface although the overall charges of both the species are same.[4.32] Further supportive evidence in favor of the structural deformation and the basis of such deformation for BSA and BLG could be drawn from Figure 4.7. It (Figure 4.7) represents the surface potential of BSA and BLG at pH 7.[4.33] The surface of the BSA is predominantly negative and the positive patches are buried deep in the core of the protein are inaccessible without altering conformation of the protein. This also compels the alteration in the secondary component of BSA which facilitates the interaction. But from the Figure 4.7 it is apparent that the positive patches of BLG are not buried too deep into the core of the protein and are easily accessible. This might be the probable reason for the BLG with a very less alteration in the secondary structure could effectively assist the adsorption at pH 7.

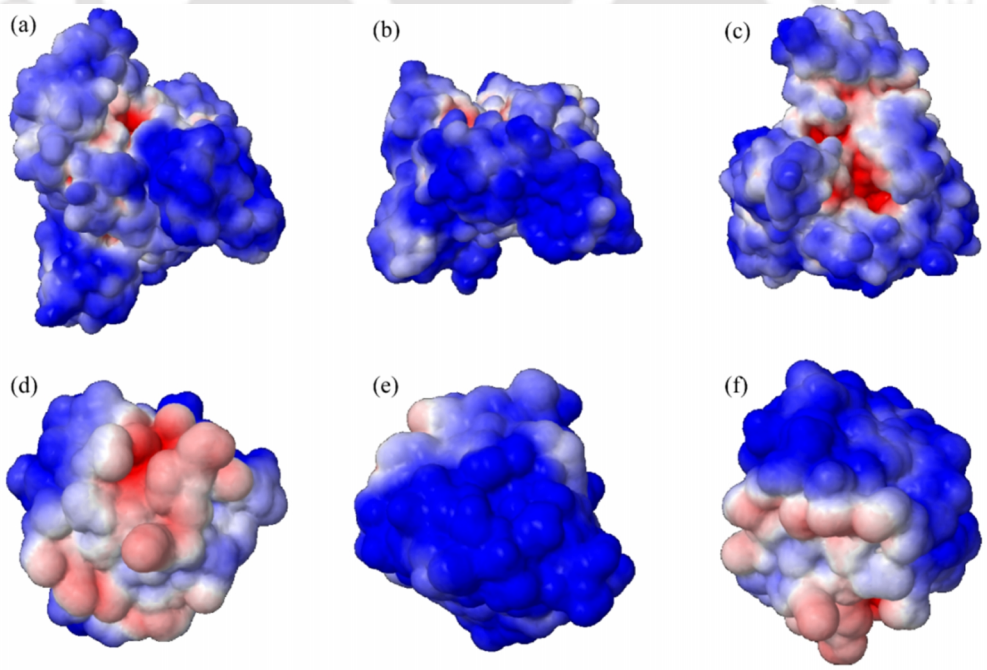

Figure 4.7. Schematic representation of the surface electrostatic potential of BSA (a, b, c) and BLG (d, e, f) at pH 7. The structures were calculated online at http://kryptonite.nbcr.net/pdb2pqr/ using the pdb code 3V03 for BSA and BLG pdb code 3BLG. The monomer fraction of BSA was taken for the purpose. (blue: negative potential, red: positive potential; range from −5 kBT/e to +5 kBT/e)

4.3.5 Summary

In conclusion, this work gives an overview of the adsorption consequence of two different proteins possessing net negative charge and different conformational flexibility, onto the negative surface of ZnS nanoparticle. The proteins undertaken are BSA and BLG, having near same IEP (~5) and differ in their conformational flexibility. BSA is considered "soft" while BLG holds the conformational rigidity and considered as "hard" protein. At pH ~7 the ZnS surface is negative (ZnS_{PZC} ~ 3.7), whereas the proteins also possess net negative charges. BSA was found to adsorb more compared to BLG. From the Fluorescence and CD conformational analysis it was revealed that BSA undergoes a prominent secondary structural change with the extent of adsorption, whereas BLG resist to such deformation. These results are in agreement with the known susceptibility of these proteins to conformational changes. In both systems, an increase in protein surface coverage was observed with the increase in free protein concentration in the solution and ζ values approaching that of native protein at high surface coverage. This findings could help us to understand better how proteins susceptible to conformation change, could structurally adjust themselves to maximize the adsorption onto surfaces having like charge. This aids to the designing and construct of different bio-nano composites where charge-factor shall seldom play a role.

References

[4.1] P. Roach, D. Farrar, C. C. Perry, J. Am. Chem. Soc. 127 (2005) 8169-8173.

[4.2] J. Buijs, W. Norde, J. W. T. Lichtenbelt, Langmuir 12 (1996) 1605-1613.

[4.3] J. C. Froberg, T. Arnebrant, J. McGuire, P. M. Claesson, Langmuir 14 (1998) 456-462.

[4.4] W. Norde, Clin. Mater. 11 (1992) 85-91.

[4.5] A. V. Elgersma, R. L. J. Zsom, W. Norde, J. Lyklema, Colloids Surf. 54 (1991) 89-101.

[4.6] C. A. Haynes, W. Norde, J. Colloid. Interf. Sci. 169 (1995) 313–328.

[4.7] W. Norde, J. P. Favier, Colloids Surf. 64 (1992) 87-93.

[4.8] F. Turci, E. Ghibaudi, M. Colonna, B. Boscolo, I. Fenoglio, B. Fubin, Langmuir 26 (2010) 8336-8346.

[4.9] C. F. Wertz, M. M. Santore, Langmuir 18 (2002) 1190-1199.

[4.10] D. J. Cole, M. C. Payne, L. C. Ciacchi, Phys. Chem. Chem. Phys. 11 (2009) 11395-11399.

[4.11] K. Rezwan, A. R. Studart, J. Vörös, L. J. Gauckler, J. Phys. Chem. B 109 (2005) 14469-14474.

[4.12] K. Kawasaki, M. Kambara, H. Matsumura, W. Norde, Colloids Surf., B 32 (2003) 321-334.

[4.13] K. Yamasaki, T. Maruyama, U. Kragh-Hansen, M. Otagiri, Biochim. Biophys. Acta 1295 (1996) 147-157.

[4.14] K. Hirayama, S. Akashi, M. Furuya, K. Fukuhara, Biochem. Biophys. Res. Commun. 173 (1990) 639-646.

[4.15] J. Cerbulis, H. M. Farrell Jr., J. Dairy Sci. 58 (1975) 817-827.

[4.16] J. Etheve, P. Dejardin, Langmuir 18 (2002) 1777-1785.

[4.17] S. Chakraborti, P. Joshi, D. Chakravarty, V. Shanker, Z. A. Ansari, S. P. Singh, P. Chakrabarti, Langmuir 28 (2012) 11142-11152.

[4.18] K. Sakurai, T. Konuma, M. Yagi, Y. Goto, Biochim. Biophys. Acta.1790 (2009) 527-537.

[4.19] J.R. Lakowicz, Principles of Fluorescence Spectroscopy, Third Ed., Plenum Press, New York, 2006.

[4.20] G. Z. Chen, X. Z. Huang, J. G. Xu, Z. Z. Zheng, Z. B. Wang, The Methods of Fluorescence Analysis, Second Ed., Beijing Science Press, Beijing, 1990.

[4.21] S.M. Andrade, T. I. Carvalho, M. I. Viseu, S. M. Costa. Eur. J. Biochem. 271 (2004) 734-744.

[4.22] D. Wu, Z. Chen, X. Liu, Spectrochim. Acta A 84 (2011) 178-183.

[4.23] S. Laera, G. Ceccone, F. Rossi, D. Gilliland, R. Hussain, G. Siligardi, L. Calzolai, Nano Lett. 11 (2011) 4480-4484.

[4.24] M. A. Tam, K. Hamad-Schifferli, Langmuir 21 (2005) 12080-12084.

[4.25] N. Taulier, T. V. Chalikian, J Mol Biol. 314 (2001) 73-89.

[4.26] (a) F. Meder, C. Brandes, L. Treccani, K. Rezwan, Acta Biomater. 9 (2013) 5780-5787. (b) R. A. Hartvig, M. van de Weert, J. Ostergaard, L. Jorgensen, H. Jensen, Langmuir 27 (2011) 2634-2643. (c) Z. Adamczyk, M. Nattich, M. Wasilewska, M. Zaucha, Adv. Colloid Interface Sci. 168 (2011) 3-28.

[4.27] M. Rabe, D. Verdes, J. Zimmermann, S. Seeger, J Phys Chem B, 112 (2008) 13971-13980.

[4.28] M. S. Andrade, M. B. Costa, Biophys. J. 82 (2002) 1607-1619.

[4.29] W. Norde, Colloids Surf. B 61 (2008) 1-9.

[4.30] S. Tenzer, D. Docter, S. Rosfa, A. Wlodarski, J. Kuharev, A. Rekik, S. K. Knauer, C. Bantz, T. Nawroth, C. Bier, J. Sirirattanapan, W. Mann, L. Treuel, R. Zellner, M. Maskos, H. Schild, R. H. Stauber, ACS Nano 5 (2011) 7155-7167.

[4.31] W. Norde, J. Lyklema, J. Colloid Interf. Sci. 66 (1978) 295-302.

[4.32] M. Rabe, D. Verdes, S. Seeger, Adv Colloid Interface Sci. 162 (2011) 87-106.

[4.33] T. J. Dolinsky, J. E. Nielsen, J. A. McCammon, N. A. Baker, Nucleic Acids Res. 32 (2004) 665-667.

Appendix

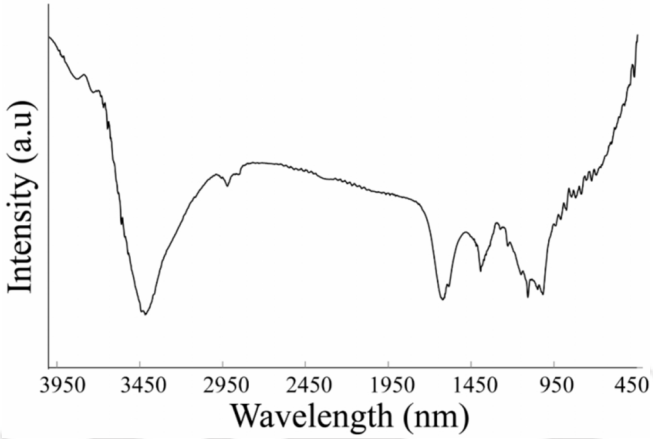

Figure A4.1. FTIR spectra of ZnS nanoparticles.

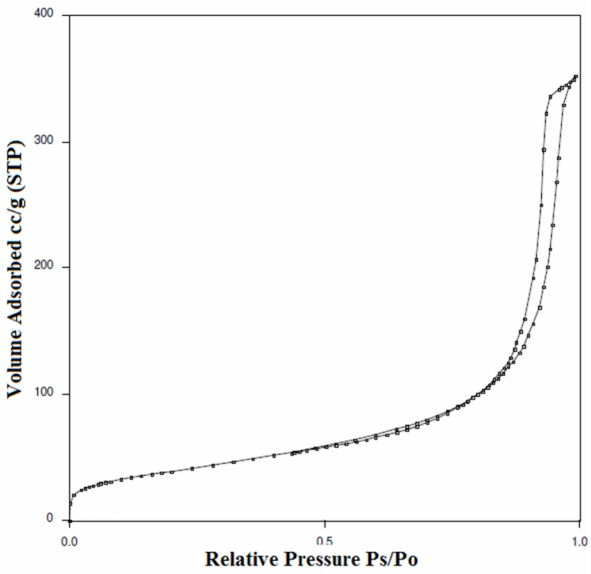

Figure A4.2. BET adsorption pattern of N_2 adsorption onto ZnS nanoparticles.

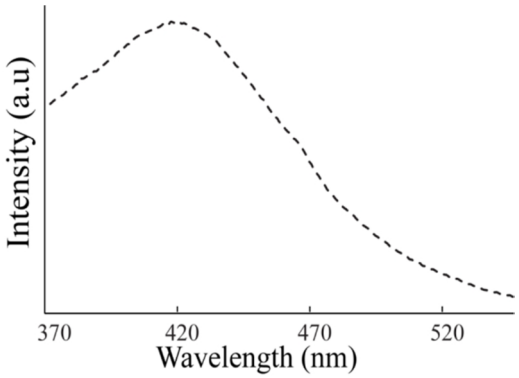

Figure A4.3. Emission spectra of ZnS NPs (excitation at 300 nm).

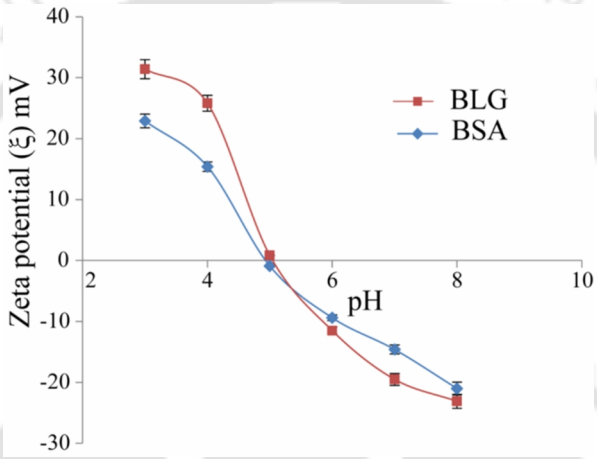

Figure A4.4. Zeta potential measurement of native BSA and BLG.

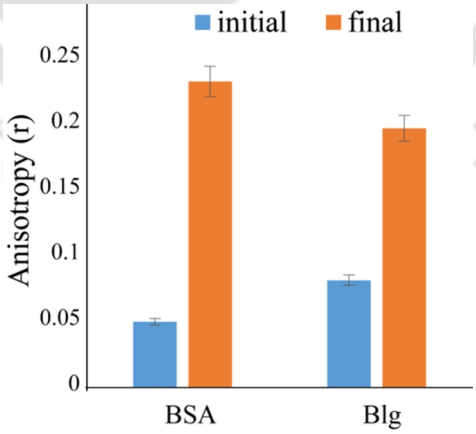

Figure A4.5. Anisotropy plot of BSA and BLG upon addition of ZnS nanoparticles.

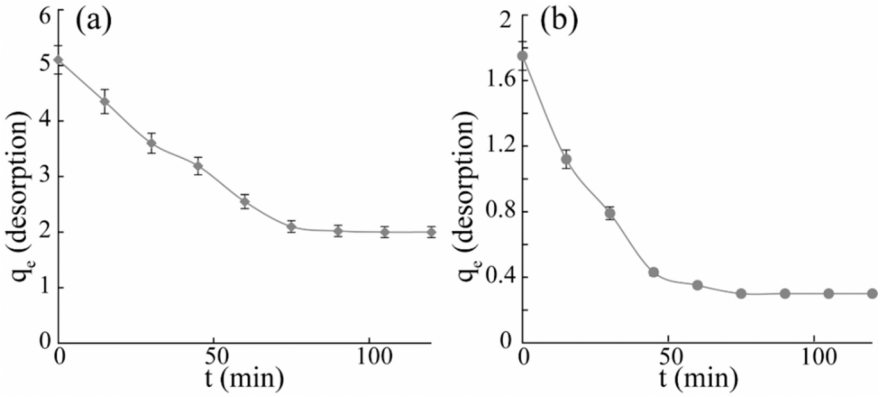

Figure A4.6 Desorption experiment of (a) BSA and (b) BLG; [Composite taken after adsorption of the 10 μg ml^{-1} protein on 0.5 mg ml-1 of ZnS NPs].

Table A4.1. Adsorption BJH pore size distribution profile of ZnS NPs.

Pore diameter Range(nm)	Pore Volume (ml/g)	Distribution %
Under 6	0.03422	6.53
6-8	0.01796	3.43
8-10	0.01818	3.47
10-12	0.02100	4.01
12-16	0.03094	5.90
16-20	0.03912	7.47
20-80	0.34142	65.17
Over 80	0.02108	4.02
BJH Total	**0.52392**	**100**

Chapter 5

Malachite-Pollutant interaction

Chapter 5

5.1 Introduction

After studying the effect of 'hard' and 'soft' surfaces on protein interaction behavior this chapter advances to study the interaction of another 'basic' and 'hard' inorganic mineral nanoparticle surface with pollutants. Malachite or basic copper carbonate is a naturally occurring secondary copper mineral with the composition of $Cu_2(OH)_2CO_3$. The presence of $-CO_3$ and $-OH$ groups on the surface of malachite makes it a surface of choice for pollutant to interact in aqueous solution. Previous literature reports the use of malachite as catalyst, fertilizer, antimicrobial agent, wood preservative, sensor development, and in fabricating electronic devices have been reported.[5.1] Molchan *et al.* has reported a polyol-mediated synthesis of malachite nanoparticle (NP) which involves the reaction in non-aqueous ethylene glycol media.[5.2] Herein in this section we describe the synthesis of hydrophilic malachite nanoparticles in aqueous medium and its interaction with various pollutants has been investigated in details.

5.2 Synthesis and characterization of malachite nanoparticles

Malachite nanoparticles with an average size of 100-150 nm have been synthesized and characterized as described previously.[5.3] 200 mg of $CuSO_4 \cdot 5H_2O$ was added to 100 mL of 4 mM aqueous solution of SDS in a 250 mL round-bottom flask with stirring for 30 min. After that, 10 mM Na_2CO_3 solution was added drop wise with constant stirring at room temperature for an additional 2h. This resulted in the formation of a green suspension which was stable as no sedimentation was observed for more than 24h. The reaction product was centrifuged at 15000 rpm. Two-step washing was undertaken; first the precipitate was re-suspended by sonication in distilled water several times to remove soluble impurity, followed by several times washing with ethanol. The final product was centrifuged and vacuum-dried for overnight.

The as synthesized malachite NPs were characterized using various techniques. The TEM images in Figure 5.1a reveals the spherical shape of malachite NPs which are fairly polydisperse in nature. The size distribution of the malachite varies in the range of 100-150 nm. The PXRD data (Figure 5.1b) shows the formation of crystalline malachite

mineral, and the peaks are matching well with malachite phases (JCPDS file no. 01-076-0660). The zeta potential analysis in Figure 5.1c showed that malachite NPs has a high positive charge (~15−20 mV) on their surface in the pH range of 5−7. The point of zero charge (PZC) of malachite NPs is around pH ~7.6 which confines well with the previously reported results by Gonzaletz and Laskowski.[5.4] The BET surface area analysis represented that malachite NPs have a specific surface area of 20.5 ± 0.2 m^2 g^{-1} and pore volume of 0.060 cm^3 g^{-1}. (Appendix. Figure A5.1). The FTIR spectra also favours the formation of the malachite mineral and are given in the Appendix section of this chapter (Appendix, Figure A5.2) The thermogravimetric analysis of the malachite NPs are also included in the Appendix section (Appendix, Figure A5.3).

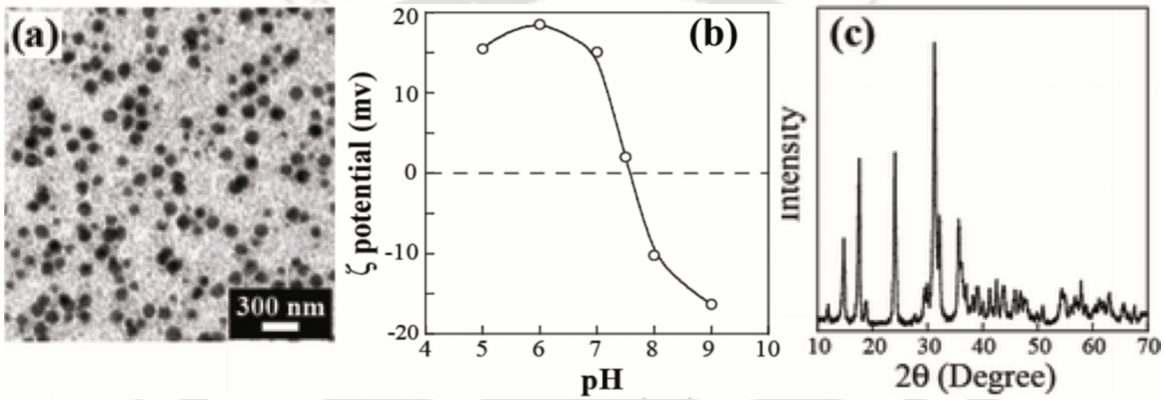

Figure 5.1. (a) TEM image showing the dispersed malachite nanoparticles, (b) ζ–potential measurement plot of malachite nanoparticles and (c) PXRD pattern of the malachite nanoparticles.

This chapter has been divided into two sections:

Part 1: Interaction and removal of inorganic pollutants using malachite nanoparticles.

Part 2: Interaction and removal of some organic pollutants using malachite nanoparticles.

Part 1

5.4 Interaction and removal of inorganic pollutants using malachite nanoparticles

5.4.1 Background

The recent environmental issues are receiving increasing attention for being contaminated by various pollutants due to their potentially hazardous risk to public

health and the environment. Inorganic pollutants are one of the major concerns for the environmental degradation. In the bigger scenario of inorganic pollutants, anionic pollutants like arsenate and chromate contributes a lot. These are toxic pollutants that contaminate the water system and enter the food chain causing fatal diseases in human.[5.5] These pollutants are introduced into the environment from a variety of processes such as, mineral weathering, mining, industrial applications including leather tanning, textile dyeing, metal finishing, electroplating, inorganic chemicals production etc.[5.6,5.7] Hexavalent chromium usually exists in wastewater as oxyanions such as chromate (CrO_4^{2-}) and dichromate ($Cr_2O_7^{2-}$) which are mostly toxic, carcinogenic and mutagenic and does not precipitate easily using conventional precipitation methods.[5.8,5.9] Similarly, the common forms of arsenate predominantly present are $H_2AsO_4^-$, $HAsO_4^{2-}$ and AsO_4^{3-} in oxygen rich aerobic waste sources are capable of imposing several health hazards in terms of skin, lung, and kidney cancer as well as pigmentation changes, neurological disorders, muscular weakness etc.[5.10-5.14] Therefore, the removal of these pollutants from the contaminated waste sources is critically important for the protection of human health and sustainable environment.

Numerous methods have been developed for the removal of such pollutants in wastewater, including adsorption, electrochemical precipitation, ion exchange, membrane ultra-filtration, reverse osmosis and reduction.[5.15,5.16] Emerging as one of the most promising techniques for removal of pollutants from industrial wastewaters, adsorption technology has been employed widely and established as an effective method in remediation technologies. Adsorption, when combined with appropriate desorption step, can also solves the problem of sludge disposal, which is a major concern in precipitation method.[5.17,5.18] Nowadays, nanoparticles are in high demand in environmental remediation technologies for their high surface to volume ratio. As discussed above, a nano-structured material having positive charge on its surface can be effective for adsorbing the anionic pollutants from waste sources. In this regard, malachite nanoparticles, a basic hydrophilic surface, can be a good choice for the removal of chromate and arsenate. Malachite or basic copper carbonate is a naturally occurring secondary copper mineral with the composition of $Cu_2(OH)_2CO_3$. Previous studies have reported that the malachite nanoparticles have the $-CO_3$ and $-OH$ groups on the surface, having a pH_{PZC} of ~7.5.[5.3,5.19] Therefore, the malachite surface would be positively charged in the broad pH range upto ~7.5, which in turn can be a potential surface for adsorption of anionic pollutants such as chromate and arsenate.

5.4.2 Materials and methods

Adsorption isotherms were studied with varying initial concentrations of pollutants (chromate and arsenate) ranging from 20-500 mg L^{-1}. The pollutants were stirred with defined 5 g L^{-1} of malachite nanoparticles. Solution pH of the adsorption experiments were varied (by 0.1 M HCl and NaOH) from 4.0 to 9.0 to check the adsorption efficiency of malachite nanoparticles for both chromate and arsenate. Kinetics experiments were carried out at different time interval by withdrawing the aliquot of supernatant from the adsorption mixture until steady state reaches. The influence of nanoparticle concentration on the adsorption of arsenate and chromate was performed with a malachite concentration from 5-20 g L^{-1}. Temperature depended studies were performed in an increasing temperature range from 10-40 ^{o}C. Competitive adsorption study of these anions were performed with mixed solution containing 50 mg L^{-1} of both chromate and arsenate. Desorption of chromate and arsenate from the adsorbent surface was carried out in batch mode. After equilibrium reaches, the adsorbent containing adsorbed chromate and arsenate was separated by centrifugation and air dried. For desorption studies after drying the adsorbent was re-dispersed and the pH was raised from 9 to 12 using 0.1-0.5 M NaOH.

5.4.3 Results

5.4.3.1 Influence of solution pH

Surface properties of the adsorbent and ionic forms of metal ions in solution are largely controlled by the pH of the medium. The value of pH_{PZC} of malachite nanoparticles is around 7.5. The adsorption efficiency was found to be maximum for pH 4 in both the cases of chromate and arsenate and reduces thereafter as the pH was raised (Figure 5.2a). The presence of chromate and arsenate on the malachite surface after adsorption was confirmed by EDX analysis (Figure 5.2b and 5.2c). These results could be justified taking the pH_{PZC} of the malachite surface into account and the anionic forms of both the anions. In the pH range from 2 to 6, for Cr(VI), $HCrO_4^-$ and $Cr_2O_7^{2-}$ are predominating species in the equilibrium and in basic medium it exist as CrO_4^{2-}.[5.20] Similarly As(V) ion occurs mainly in the form of $H_2AsO_4^-$ in the pH range between 3 and 6, while a divalent anion $HAsO_4^{2-}$ dominates at higher pH values.[5.21] Therefore, at pH range 2.0-6.0, the malachite surface ($pH < pH_{PZC}$) remains positively charged and further the –OH groups in the malachite surface gets protonated to a higher extent and turns to $–OH_2^+$. This

positively charged malachite surface facilitates the electrostatic interaction with the anionic pollutants, which in turn leads to a higher adsorption capacity.[5.22,5.23] At higher pH, due to more OH^- ions on malachite surface carrying net negative charges, the repulsion between the anions (CrO_4^{2-} and $HAsO_4^{2-}$) and the nanoparticles surface increases, which results in a decreased adsorption capacity of both the anions.[5.24]

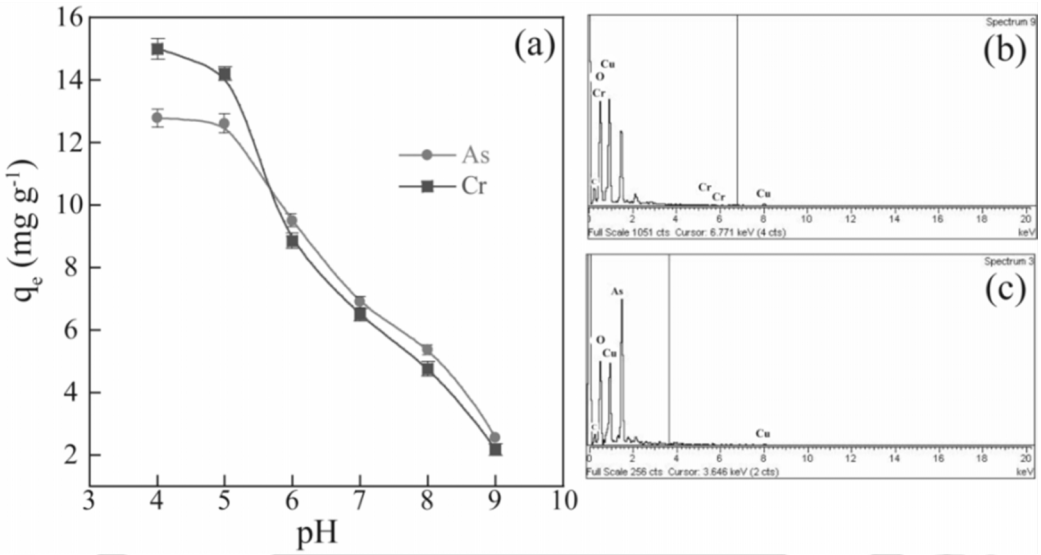

Figure 5.2. (a) Effect of initial solution pH on chromate and arsenate ions adsorption by malachite nanoparticles (chromate and arsenate concentration = 100mg L^{-1}; adsorbent dose = 5g L^{-1})and (b) EDX analysis of adsorbed (b) chromate and (c) arsenate on malachite nanoparticles.

5.4.3.2 Adsorption steady state and kinetic model

The kinetics of adsorption describes the rate of ion uptake on the nanoparticle and this rate controls the equilibrium time. The kinetics of adsorbate uptake is required for selecting optimum operating conditions for the full-scale batch process.[5.25] The kinetic parameter, which is helpful for the prediction of adsorption rate, gives important information for designing and modelling the processes. Thus, the effect of contact time was analysed from the kinetic point of view. From the equilibrium studies, it was found that steady state reaches within 12 h and 5 h for chromate and arsenate respectively irrespective of initial concentration (Figure 5.3).

The adsorption kinetics of chromate and arsenate on malachite nanoparticle was studied with respect to Lagergren first order (Eq. 5.1a) and second-order kinetic model (Eq. 5.1b).[5.26a, 5.26b]

$$\log(q_e - q_t) = \log q_e - (1 / 2.303)\, k_1 t \qquad (5.1a)$$

$$(t / q_t) = (1/ q_e^2 k_2) + (t / q_e) \quad (5.1b)$$

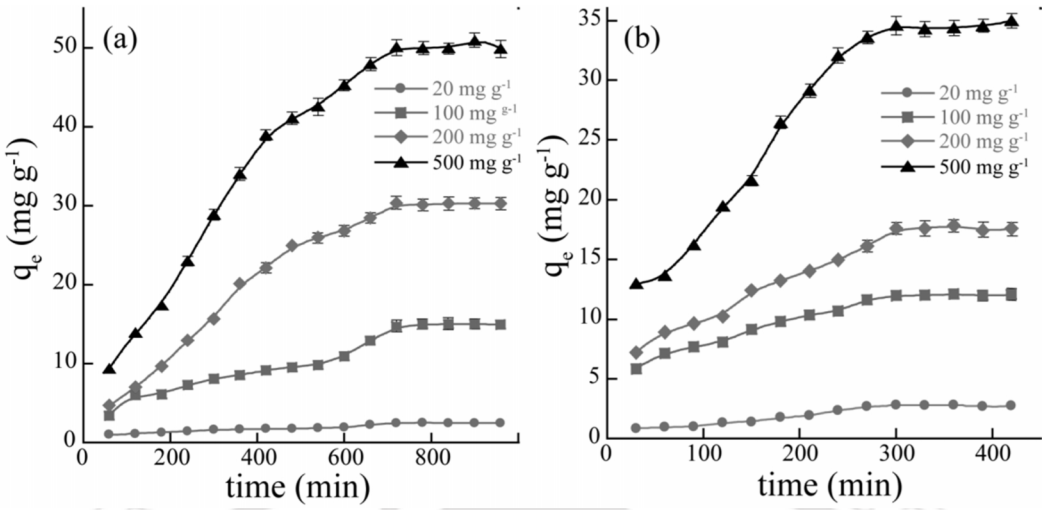

Figure 5.3. Effect of initial metal concentration and contact time on adsorption (a) for chromate and (b) for arsenate (pH 5; absorbent dosage=5g L^{-1}; temperature = 30±1◦C; stirring speed = 200 rpm for both).

Where, the q_t and q_e (mg g^{-1}) are total adsorption capacity at time t and at equilibrium respectively. k_1 and k_2 are first and second order rate constant respectively. Table 5.1 shows all the kinetic constant values. It was found that the first order rate equation showed correlation coefficient of 0.984 for chromate and 0.994 for arsenate; while the second order correlation coefficient was 0.990 for chromate and 0.995 for arsenate (Appendix, Figure A5.4). Therefore the adsorption process for both chromate and arsenate can be better described by the second order reaction kinetics.

Another empirically established functional relationship proposed by Weber and Morris, the intraparticle diffusion model was applied to fit the kinetic experimental results.[5.27] The root time dependent equation is given (Eq. 5.2c) by,

$$q_t = K_w t^{1/2} + C \quad (5.2c)$$

Where K_w is an intraparticle diffusion rate constant and C is the intercept. The slope in the linearized fitted curve using intraparticle model (Appendix. A5.4), characterizes the rate parameter corresponding to the intraparticle diffusion, whereas the intercept of this portion is proportional to the boundary layer thickness. The values of rate constant K_w and C were calculated from the fitted model and given in Table 5.1. The linearized

curve in both the cases do not pass through the origin (~1.0 mg g^{-1} for chromate and ~3.6 mg g^{-1} for arsenate) indicates that intraparticle diffusion is involved in the adsorption process but it is not the only rate-limiting mechanism and that some other mechanisms also play an important role. Surface adsorption and intraparticle diffusion were likely to take place simultaneously.

Table 5.1. Comparison of rate constants calculated based on respective first-order, second-order and intra-particle diffusion kinetic models.

	First order kinetics		Second order kinetics		Intra-particle diffusion kinetics		
	k_1 (L min^{-1})	R^2	k_2 (g mg^{-1} min^{-1})	R^2	K_w (mg g^{-1} $min^{-0.5}$)	C (mg g^{-1})	R^2
Chromate	0.0015	0.984	0.0004	0.994	0.3950	1.0	0.983
Arsenate	0.0071	0.990	0.0011	0.995	0.4507	3.6	0.982

5.4.3.3 Effect of malachite nanoparticle concentration

Concentration of malachite nanoparticles was varied from 5-20 g L^{-1} (for 100 mg L^{-1} initial chromate and arsenate) in a batch mode adsorption study at pH ~5.0. As the concentration of malachite nanoparticle was increased from 5 g L^{-1} to 20 g L^{-1} the adsorption capacity (q_e) was found to decrease (Figure 5.4). Although, the total removal efficiency (%) for chromate and arsenate is increased with the increase in malachite concentration. As the mass of the adsorbent increases, the total surface area and in turns the number of active adsorption sites increases. However the amount of anions adsorbed per unit mass/area of adsorbent decreases, resulting in reduction of the adsorption capacity (q_e).

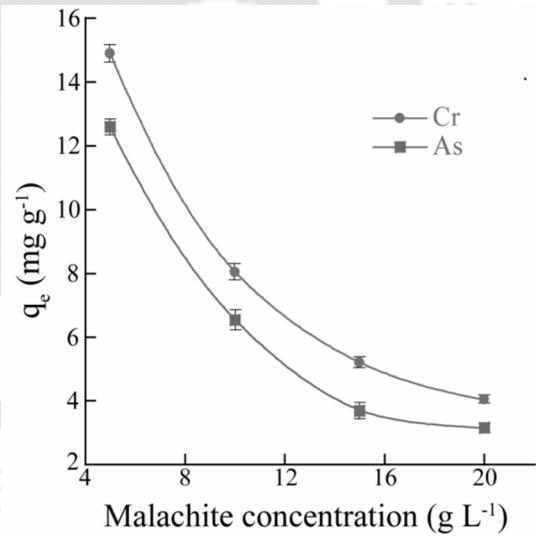

Figure 5.4. Effect of absorbent dosage on the adsorption of (a) chromate and (b) arsenate (pH 5.0; concentration = 100mg L^{-1}; temperature = 30±1 ◦C; stirring speed = 200 rpm for both).

5.4.3.4 Effect of initial ion concentration and adsorption isotherm

The equilibrium adsorption isotherm of chromate and arsenate are presented in Figure 5.5. The initial anion concentration was varied from 20 to 500 mg L^{-1} with 5 g L^{-1} of malachite at pH 5.0. According to the slope of initial portion of the curve, as seen from Figure 5.5, the adsorption isotherm may be classified as H–type of the Giles' classification.[5.28] The H–type isotherms are the most common and correspond to high affinity of adsorbate for a given adsorbent. Hence, competition from the solvent for adsorption sites was not observed. As the isotherm tends to plateau, it seems reasonable to assume that complete coverage of the adsorbent surface occurs and steady state is reached.

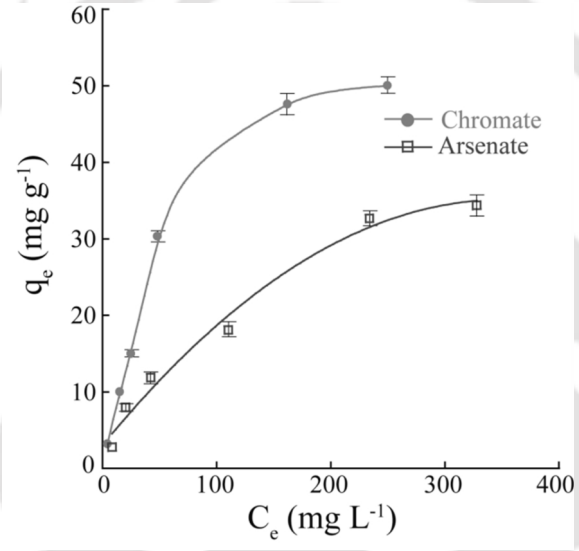

Figure 5.5. Adsorption isotherm plot of (a) chromate and (b) arsenate, on malachite nanoparticles (pH 5.0; concentration = 100mg L−1; temperature = 30±1 ◦C; stirring speed = 200 rpm for both).

The adsorption process of chromate and arsenate is analysed with Langmuir, Freundlich and Dubinin-Radushkevich isotherm model. The main consideration of Langmuir isotherm is sorption takes place at specific homogeneous sites within the adsorbent, indicating a monolayer adsorption process (constant heat of adsorption for all sites). The Langmuir isotherm is expressed as

$$q_e = Q_m b C_e/(1+bC_e) \quad (5.3)$$

where, C_e (mg L^{-1}) and q_e (mg g^{-1}) are the equilibrium metal ion concentration in aqueous and solid phase respectively.[5.29] Q_m is the maximum monolayer uptake by the adsorbent (mg g^{-1}), and b is the Langmuir binding constant of the adsorption. A constant

factor called "constant separation factor" or "equilibrium parameter", R_L is defined as

$$R_L=1/(1+bC_0) \quad (5.4)$$

The values of R_L informs about the favourability of the sorption process. For a favourable reaction process, $0< R_L<1$; whereas R=0 for the irreversible case, R=1 for the linear case and R>1 for unfavourable reaction. The Freundlich adsorption isotherm is generally based on multilayer adsorption on heterogeneous surface. This holds the assumption that the adsorption sites are distributed exponentially with respect to heat of adsorption. Freundlich isotherm is given as

$$q_e = K_f C_e \, 1/n \quad (5.5)$$

K_f is the Freundlich's uptake factor and n denotes Freundlich's intensity factor.[5.30] The value of n in the range of 1 to 10 denotes favourable adsorption, could be find out from the linearized form of Freundlich isotherm. The values of regression coefficients obtained from these models were used as the fitting criteria to find out these isotherms. It was found that the plots in both the cases depicted the linear form of the isotherms and the extremely high correlation coefficients ($R^2_{langmuir}$=0.999 for chromate and 0.992 for arsenate; $R^2_{freundlich}$=0.975 for chromate and 0.981 for arsenate), indicating both monolayer and heterogeneous surface conditions may exist. The maximum adsorption capacity (Q_m) for chromate and arsenate, obtained from Langmuir isotherm model were 82.2 mg g^{-1} and 57.1 mg g^{-1} respectively (Table 5.2). The R_L values, calculated using Eq. 5.4, were in between 0 and 1 (0.52 and 0.62 for chromate and arsenate respectively) for both the anions, indicating the favourable adsorption process.

Dubinin and Radushkevich (D–R) equation is represented in a linear form by equation:

$$\ln q_e = \ln Q_0 - K_{DR}\varepsilon^2 \quad (5.6a)$$

where, K_{DR} ($mol^2\ kJ^{-2}$) is a constant related to mean adsorption energy.[5.31] And ε is the Polanyi potential, which can be calculated from equation,[5.32]

$$\varepsilon = RT \ln [1 + (1/C_e)] \quad (5.6b)$$

The slope of the plot of ln q_e versus ε^2 gives K_{DR} ($mol^2\ kJ^{-2}$) and the intercept yields the sorption capacity, Q_0 (mg g^{-1}). T is the absolute temperature in K and R is the universal

gas constant (8.314 J mol^{-1} K^{-1}). The adsorption energy for these anions on malachite nanoparticles can be calculated using the following relationship,[5.31]

$$E = 1/(2K_{DR})^{1/2} \quad (5.6c)$$

The isotherm constants for Langmuir, Freundlich and D-R models are calculated from the isotherm equations and given in Table 5.2. The adsorption energy of chromate and arsenate worked out using Eq. 5.6c was found to be 3.38 kJ mol^{-1} and 2.89 kJ mol^{-1} respectively. In both the cases the E value are less than 16 kJ mol^{-1}, which indicate that the physical adsorption is the major process involved for adsorption of chromate and arsenate. The positive value of E indicates that the sorption process was endothermic so that higher solution temperature would favour the sorption process.

Table 5.2. Adsorption isotherm parameters of chromium and arsenate on malachite nanoparticles.

	Langmuir isotherm				Freundlich isotherm			D-R isotherm		
	Q_m	b ($L\ mg^{-1}$)	R^2	R_L	K_f ($mg\ g^{-1}$)	n	R^2	Q_0 ($mg\ g^{-1}$)	K_{DR} ($mol^2\ kJ^{-2}$)	R^2
Chromate	82.2	0.009	0.999	0.52	1.472	1.45	0.975	41.07	0.0437	0.931
Arsenate	57.1	0.006	0.992	0.62	1.559	1.85	0.981	25.028	0.0596	0.841

5.4.3.5. Effect of temperature and thermodynamic study

Temperature of the system in an adsorption process is very important regulating parameter which is associated with different thermodynamic aspect of this process. The thermodynamic favourability of a process can be obtained from this analysis. To study the thermodynamics of a process, the adsorption was carried out at different temperature from 10 ºC to 40 ºC. It was found from the results that the adsorption capacity increased from 11.4 mg g^{-1} to 15.6 mg g^{-1} for chromate and 10.1 mg g^{-1} to 12.1 mg g^{-1} in case of arsenate when temperature is increased from 10ºC to 40 ºC (Figure 5.6a). The standard Gibbs free energy change (ΔG^o) was calculated from the following equation,

$$\Delta G^o = - RT \ln (k_c) \quad (5.7a)$$

Where R is the universal gas constant (8.314 J mol^{-1} K^{-1}) and T is temperature in Kelvin. k_c is the equilibrium stability constant, which was calculated at each temperature using the relation,

$$k_c = C_s/C_e \quad (5.7b)$$

where, C_s and C_e are the equilibrium chromate and arsenate (in respective cases) concentration on adsorbent and aqueous phase respectively. The Gibbs free energy changes (ΔG^o) in this temperature range were calculated from Eq. 5.7a, and are given in Table 5.3. The negative values of ΔG^o suggest that the adsorption process is spontaneous and thermodynamically favourable.[5.33] The average standard enthalpy change (ΔH^o) and entropy change (ΔS^o) were determined from Van't Hoff equation (Eq. 5.7c),

$$\ln k_c = \Delta S^o/R - (\Delta H^o)/RT \quad (5.7c)$$

ΔH^o and ΔS^o were calculated from the slope and intercept of plot between ln (k_c) vs. (1/T) based on Van't Hoff equation (Figure 5.6b). To a certain extent, physisorption and chemisorption can be classified by the magnitude of the enthalpy change (ΔH^o). Bonding strengths of less than 84 kJ mol^{-1} are typically considered as those of physisorption bonds. Chemisorption bond strengths ranges from 84-420 kJ mol^{-1} .[5.34] From Van't Hoff curve it was found that the value of ΔH^o is about 23.3 and 9.86 kJ mol^{-1} K^{-1} respectively for chromate and arsenate. This establishes that the adsorption process takes place mainly through physisorption. This also supports the previous discussion obtained from D-R isotherm model. The value of ΔS^o was found to be positive reflecting the spontaneity of the adsorption process. The positive values of ΔH^o revealed that the adsorption process was endothermic in nature; which leads to the higher adsorption capacity at higher temperature as obtained from this experiment.

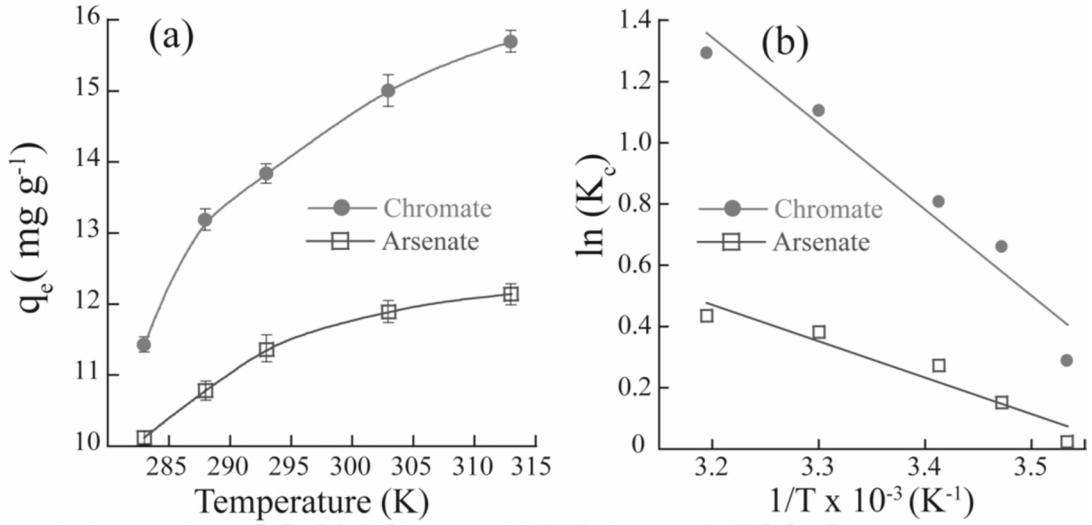

Figure 5.6. (a) Adsorption capacity of chromate and arsenate in temperature range of 10 °C to 40 °C and (b) Van't Hoff plot of chromate and arsenate adsorption on malachite nanoparticles.

Table 5.3. Thermodynamic parameters of chromate and arsenate adsorption onto malachite nanoparticles.

Temp. (K)	Chromate			Arsenate		
	ΔG° (KJ mol^{-1})	ΔS° (J mol^{-1} K^{-1})	ΔH° (KJ mol^{-1})	ΔG° (KJ mol^{-1})	ΔS° (J mol^{-1} K^{-1})	ΔH° (KJ mol^{-1})
283	-0.676			-0.056		
288	-1.580			-0.371		
293	-1.966	85.88	23.34	-0.665	35.47	9.861
303	-2.781			-0.963		
313	-3.360			-1.131		

5.4.3.6. Competitive adsorption and desorption studies

Competitive study with 50 mg L^{-1} of both chromate and arsenate reflects similar adsorption behaviour as observed in single-component study. The adsorption efficiency of chromate and arsenate from binary mixture was ~70% and ~61% respectively (Figure 5.7a). However in binary mixture, the adsorption efficiency (%) of these two pollutants decreases to some extent compared to that of in single-component study (~75% for

chromate and ~66% for arsenate). This is mainly due to the competitive binding of these two anions on malachite nanoparticles.

Moreover, in the competitive and single-component study, the binding capacity of these anions on malachite nanoparticles was analysed with the respective distribution coefficient (K_d) values of each ions. The distribution coefficient (K_d) is described as the ability of adsorbents to remove a given ion from solution and can be expressed as,

$$K_d = q_e/C_e \quad (5.8)$$

where, q_e and C_e are steady-state concentrations of a given ion on adsorbent (mg g^{-1} of adsorbent) and in solution (mg L^{-1}), respectively. The K_d value of chromate (~0.47 L g^{-1}) is slightly higher than that of arsenate (~0.31 L g^{-1}) in both single-component and competitive study (Figure 5.7b). However, the K_d values of both the anions decreases in competitive study compared to that in single-component study. In a mixed solution, the decrease in K_d value of an ion is mainly due to the competitive binding of other ion present in solution.

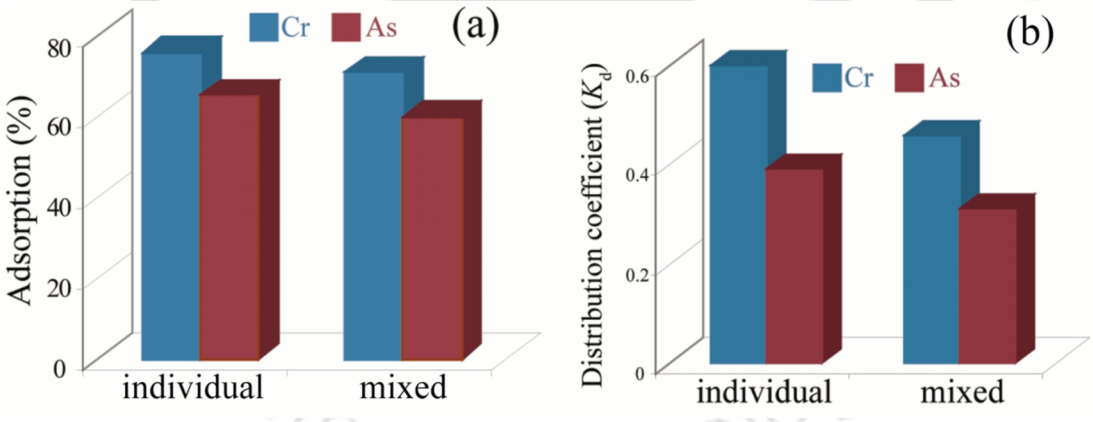

Figure 5.7. (a) Adsorption efficiency of chromate and arsenate from a mixed solution containing 50 mg L^{-1} of each anion (at pH ~5.0) and (b) Distribution coefficient (K_d) values of chromate and arsenate in individual and competitive adsorption process.

In addition, in a competitive study, the adsorption of different metal ions is mainly governed by the preferential binding affinity of the ions toward the binding site of the adsorbent. A selectivity coefficient (k) for the binding of a specific ion in the presence of other competitive ions can be obtained from equilibrium binding data (Eq. 5.9a).[5.35]

$$m_1\ (solution) + m_2\ (adsorbent) \rightleftharpoons m_1\ (adsorbent) + m_2\ (solution) \quad (5.9a)$$

$$k_1 = \{[m_1]_{adsorbent}\,[m_2]_{solution}\}/\{[m_1]_{solution}\,[m_2]_{adsorbent}\} = K_d\ (m_1)/K_d(m_2) \quad (5.9b)$$

where, K_d is the distribution coefficient of the metal ions and k_1 represents the ratio of K_d values of one ion (m_1) to another (m_2) used in the mixed solution. In the competitive study of chromate and arsenate, the selectivity coefficient of chromate ($k_{Cr/As}$ = 1.5) is higher than that of arsenate ($k_{As/Cr}$ = 0.67) (Figure 5.8a). This indicates a comparatively higher binding affinity of chromate than arsenate, which also reflects in the adsorption efficiency in competitive study (Figure 5.7a).

Desorption efficiency of chromate and arsenate loaded malachite nanoparticles in the pH range from 9.0 to 12.0 is shown in (Figure 5.8b). It has been observed that ~58% of the adsorbed anions were desorbed at pH ~9.0–10.0. However, upon increasing the pH up to ~12.0, final desorption efficiency was ~61% and ~66% for chromate and arsenate respectively. The desorption of these anionic pollutants from malachite surface at higher pH is mainly due to the electrostatic repulsion between the anionic pollutants and malachite surface. As discussed before, at pH > 7.5 the malachite surface is negatively charged and the predominant species of chromate and arsenate are CrO_4^{2-} and $HAsO_4^{2-}$ /AsO_4^{3-} in this pH range.[5.10, 5.20] Therefore the electrostatic repulsion between the negatively charged malachite surface and anionic pollutants as well as the electrostatic repulsion between these two anionic species on malachite surface lead to desorption of these pollutants from malachite surface.

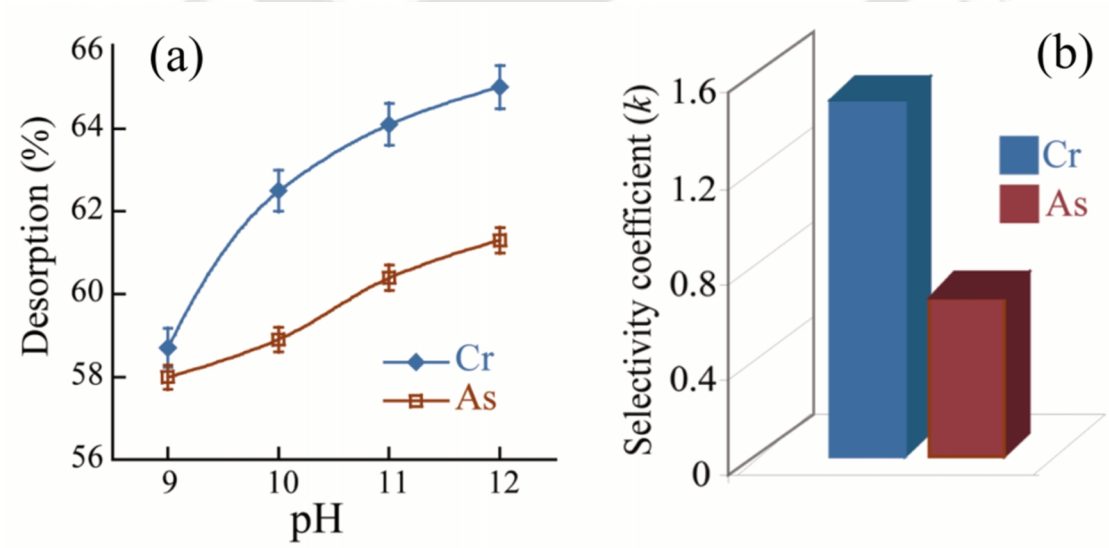

Figure 5.8. (a) Selectivity coefficient values (k) of chromate and arsenate in a competitive adsorption process; and (b) Desorption efficiency of both chromate and arsenate in higher alkaline pH.

To see the stability and any change in the characteristics of the malachite NPs the malachite after desorption were subjected to PXRD analysis (Appendix, Figure A5.7). The PXRD peaks obtained matches well with the peaks of the malachite NPs suggesting that no significant phase transformation have been occurred and this depicts the stability and usability of the malachite as NPs as a potent adsorbent.

5.4.4 Summary

In this section, we have demonstrated the efficient adsorption of toxic arsenate and chromate from wastewater on malachite nanoparticles at pH~4.0-5.0. However, the adsorption capacity decreased with the increase in pH. Kinetic models revealed that the adsorption followed second order kinetics. Intraparticle diffusion rate (K_w) indicates that intraparticle diffusion is involved in the adsorption process but it is not the only rate-limiting mechanism and surface adsorption and intraparticle diffusion were likely to take place simultaneously. The adsorption process was well fitted by the Langmuir isotherm with maximum monolayer coverage of 82.2 mg g^{-1} and 57.1 mg g^{-1} for chromate and arsenate, respectively. The positive E values calculated from the D-R model, indicates that the physical adsorption is the major process involved for adsorption of chromate and arsenate and endothermic in nature. The negative ΔG^0 and positive ΔS^0 values from thermodynamic analysis also reveals the spontaneity of the adsorption process. Competitive study with a mixed solution showed the efficient and simultaneous adsorption of both chromate and arsenate on malachite nanoparticles. However, the binding affinity of chromate with malachite surface was found comparatively higher than arsenate as calculated from selectivity coefficient analysis. Therefore, the malachite nanoparticles can be used as a potential nano-structured material for efficient removal of toxic pollutants from wastewater.

Part 2

5.5 Interaction and removal of some organic pollutants using malachite nanoparticles

5.5.1 Background

Water pollution is one of the major concerns in environmental problems due to their adverse effect in the total *biota*. Water pollution is mainly caused by the dyes and pigments which are largely used in different industries, such as textiles, plastics, paper, leather, jute, food, and cosmetic.[5.36] Discharge of these dyes in the surrounding water bodies without proper treatment can cause serious environmental and health hazards. These dyes interfere with the penetration of sunlight into water, retards photosynthesis, inhibit the growth of aquatic biota, and also interfere with gas solubility in water bodies.[5.37] Therefore, there is a significant need for the removal of these dye effluents in the water bodies for environmental benefit.

In this section we have used malachite nanoparticles (basic copper carbonate, $Cu_2(OH)_2CO_3$) for adsorption of different dyes from aqueous solution. From our previous study we have found the malachite nanoparticles were highly efficient for removal of anions such as arsenate and chromate from the aqueous solution. Malachite NPs have a high specific surface area of 20.5 ± 0.2 m^2g^{-1} with PZC (point of zero charge) value ~ 7.5. Malachite NPs have $–CO_3$ and –OH groups on the surface which facilitates adsorption.[5.38] Therefore we extended our work to see whether any organic pollutants (dyes) would also give a similar result with the Malachite surface. To further investigate the influence of nanoparticle surface properties and surface functional groups on the adsorption of dye molecules, we explored the potential of malachite NPs in adsorption of different xanthene dyes. Three different dyes viz: Fluorescein (with –COOH and –OH), Rhodamine B (with –COOH) and Rhodamine 6G each having same xanthene moiety but differing in their functionality was taken for the study. We have also studied the influence of various parameters such as the solution pH, concentration of the dye, time, temperature, NPs concentration on adsorption behaviour of dye molecules. The adsorption characteristics were evaluated from the kinetic and thermodynamic isotherm. Desorption study and the multi-cycle efficiency of the Malachite NPs were also examined.

5.5.2 Materials and methods

Adsorption of different dye was done in batch mode to procure the kinetics and equilibrium data. A dye stock solution of 500 mg L^{-1} was prepared and different desired concentrations were obtained by proper dilution with buffer solution and a volume of 2 ml was taken for the study. After addition of Malachite NPs to the dye (varying concentration of both) the vials were then kept under stirring until steady state was reached. Preliminary experiments were done to figure out the optimal conditions for various reaction parameters. The experiments were performed in duplicate for data consistency. The pH of the medium was controlled by taking acetate and phosphate buffers for the requisite pH. The ionic strength was maintained constant using 0.05M NaCl in all the cases otherwise mentioned. Desorption efficiency was calculated from the residual dye concentration of the solution and the multi-cycle efficiency of the Malachite NPs was investigated by repeating the same process with the recovered Malachite NPs.

5.5.3 Results

5.5.3.1 Adsorption properties

Malachite NPs have been found to be selective for the adsorption of xanthene dyes. The dyes we have considered for the studies are Fluorescein (Flu), Rhodamine B (RB) and Rhodamine 6G (R6G), which contains the same xanthene moiety but differs in their functionality. Flu contains the –COOH and –OH as the functional group whereas RB has only –COOH but R6G contains none of these. Although the availability and the forms at which these present are highly complex and are pH dependent. They exist as different species in the solution, from zwitterions to mono-anions and di-anions. The maximum adsorption was obtained for Flu with q_e value ~ 29.54 (mg g^{-1}) followed by RB with q_e value ~ 20.74 (mg g^{-1}). R6G was least adsorbed with q_e value ~ 6.4 (mg g^{-1}). The adsorption isotherm plot given in Figure 5.9a shows the saturation of the adsorption value with increase in the concentration of the dye concentration. The optical microscopic image of Flu adsorbed Malachite NPs given in Figure 5.9b reflects the high adsorption of the dye onto the surface of the NPs.

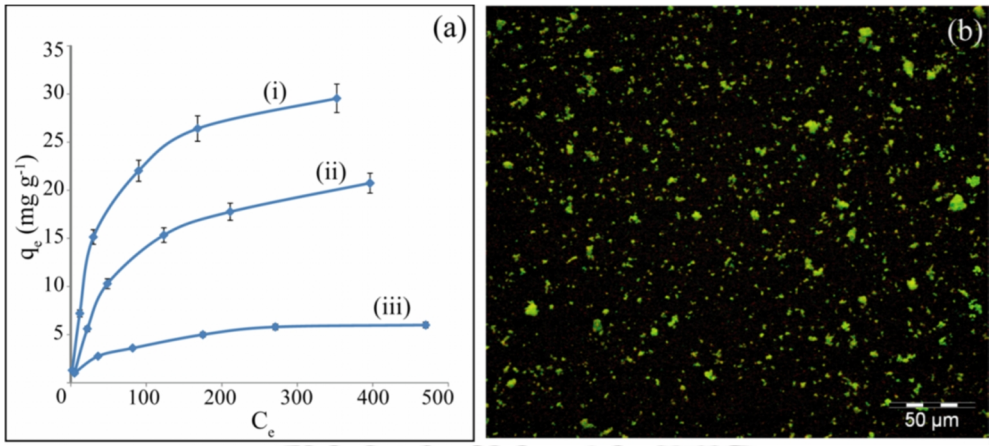

Figure 5.9. (a) Adsorption isotherm plot for Flu (i), RB (ii) and R6G (iii); (b) Optical micrograph of Flu adsorbed onto the Malachite surface.

PXRD of the Malachite NPs before and after adsorption of the dyes were taken. The PXRD spectra indicate that no significant changes were observed in the spectra which support the fact that the crystallinity of the Malachite NPs did not change after the adsorption of the dyes onto its surface.[5.39]

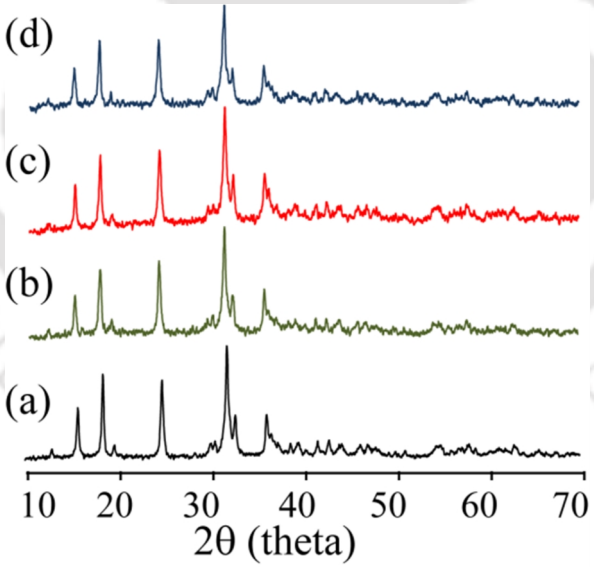

Figure 5.10. PXRD spectra of (a) only malachite NPs and malachite after desorption of dye (b) Flu, (c) RB (d) R6G.

5.5.3.2 Adsorption isotherm

Adsorption isotherm can give an insight into important parameters involved the adsorbate/adsorbent interaction and help in the designing of a preferred sorption

system.[5.40] Therefore, we have fitted our experimental data into the Langmuir and Freundlich adsorption isotherms to describe the relationship between the amounts of adsorbate adsorbed on adsorbent and its equilibrium concentration in aqueous solution. The linearized form of Langmuir and Freundlich adsorption isotherms can be expressed according to Eq. (5.10a) and Eq. (5.10b) respectively.[5.29,5.30]

$$C_e/q_e = C_e/Q_m + 1/Q_m b \quad (5.10a)$$

$$\log q_e = \log K_f + (1/n) \log C_e \quad (5.10b)$$

Where, C_e (mg L^{-1}) and q_e (mg g^{-1}) are the equilibrium dye concentration in aqueous and solid phase respectively. Q_m is the maximum monolayer uptake by the adsorbent (mg g^{-1}), and b is the Langmuir binding constant of the adsorption. K_f is the Freundlich's uptake factor and n is the Freundlich constant (index of adsorption intensity or surface heterogeneity) which denotes favourability of the adsorption if the value lies between 1 and 10.[5.41] The experimental data were fitted well with Langmuir isotherm showing high correlation coefficient (R^2_{Flu} = 0.9986, R^2_{RB} = 0.9936, R^2_{R6G} = 0.9951) as compared to the Freundlich isotherm fitting (R^2_{Flu} = 0.9119, R^2_{RB} = 0.974, R^2_{R6G} = 0.9592) for all the three cases (Figure 5.10). The high correlation of the experimental data with the Langmuir isotherm indicates that the adsorption follows preferentially the Langmuir isotherm with monolayer adsorption of dyes onto the Malachite NPs surface.[5.42] The maximum monolayer uptake value was calculated from the straight line equation of the linearized Langmuir isotherm and found to be ~ 32.47 mg g^{-1}, ~ 23.47 mg g^{-1} and 8.40 mg g^{-1} for Flu, RB and R6G respectively. The experimental values for the maximum monolayer uptake as obtained from the plateau region in Figure 5.10a were in well accordance with the calculated values favouring the Langmuir model over the Freundlich model. The plot of q_e (experimental) data overlay well with the q_e calculated from the Langmuir isotherm than the Freundlich isotherm (Appendix, A5.8). The other values obtained from the isotherms are listed in the table (Table 5.4).

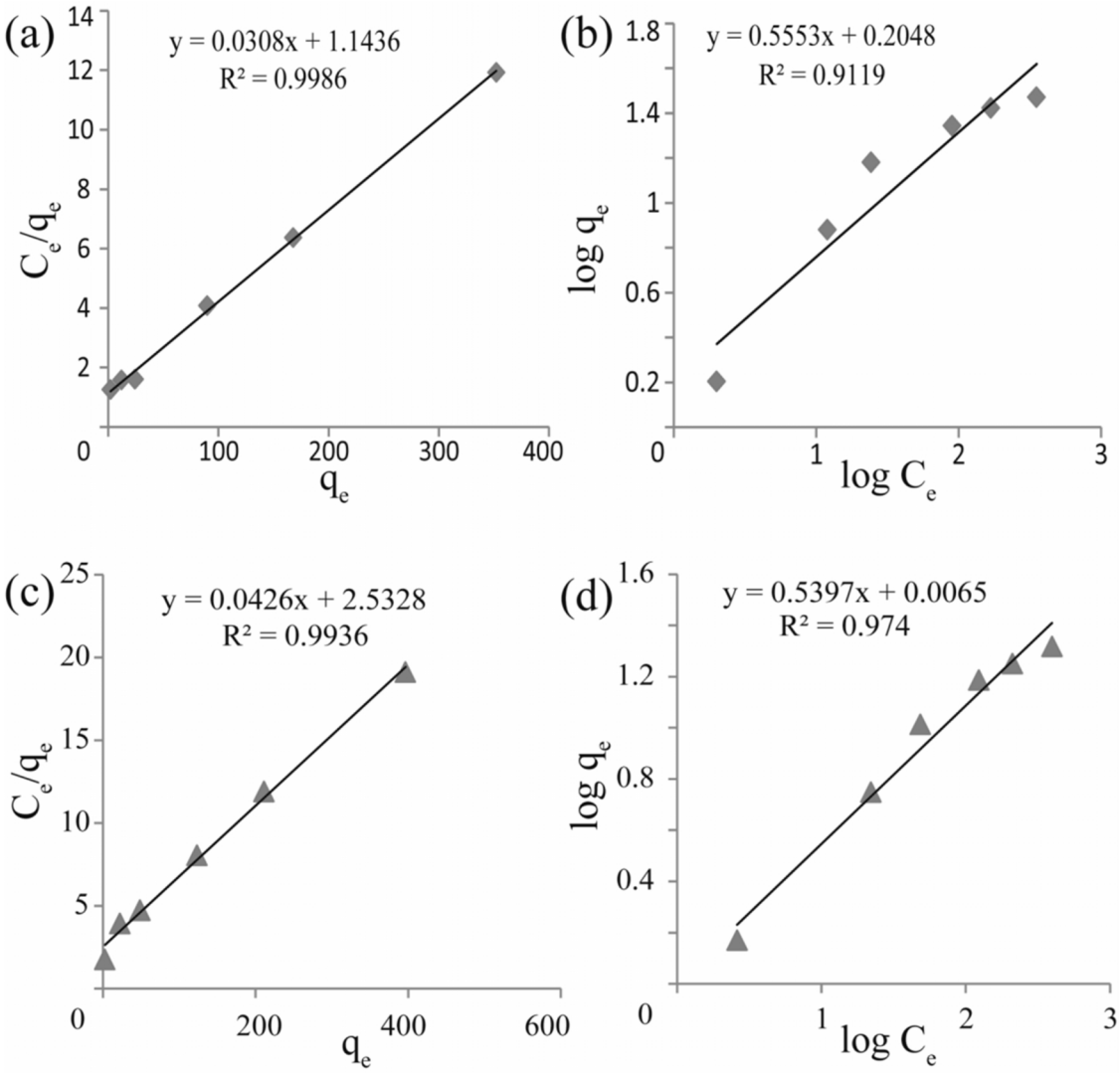

Figure 5.10. Langmuir plot (a) and (d) for Flu and RB and Freundlich isotherm plot (b) and (c) for Flu and RB respectively at 100 mg L^{-1} dye concentration and Malachite NPs concentration of 5 g L^{-1}.

Furthermore the feasibility of the sorption can also be elucidated using a dimensionless constant called "constant separation factor" or "equilibrium parameter", R_L is defined as

$$R_L = 1/ (1+ b C_0) \quad (5.10c)$$

Where b is the Langmuir coefficient and C_0 is the initial dye concentration. For a favourable reaction process, $0< R_L<1$; whereas R=0 for the irreversible case, R=1 for the linear case and R>1 for unfavourable reaction. The R_L values were 0.36, 0.50 and 0.63 for Flu, RB and R6G respectively which lies well within the favourable range.

Table 5.4. Adsorption isotherm parameters of dyes on Malachite NPs.

	Langmuir isotherm				Freundlich isotherm		
	Q_m(mg g^{-1})	b (L mg^{-1})	R^2	R_L	K_f(mg g^{-1})	n	R^2
Flu	32.46	0.0269	0.998	0.36	1.529	1.80	0.911
RB	23.47	0.0130	0.993	0.50	1.852	1.01	0.974
R6G	8.40	0.0074	0.995	0.63	1.480	0.12	0.959

5.5.3.3 Adsorption kinetics

To determine the contact time required for the optimal adsorption and equilibrium attainment of the dye and NPs system, we have taken an initial concentration of 100 mg L^{-1} and NPs concentration of 5 g L^{-1} for the study. The adsorption increased with time until a steady state was achieved at ~ 6h after which the adsorption seemed constant for all the three dyes (Figure 5.11). The kinetic data obtained could be well utilized for deducing the kinetic mechanism for the adsorption and was studied with respect to Lagergren first order (Eq. 5.11a) and second order kinetic model (Eq. 5.11b),[5.26a, 5.26b]

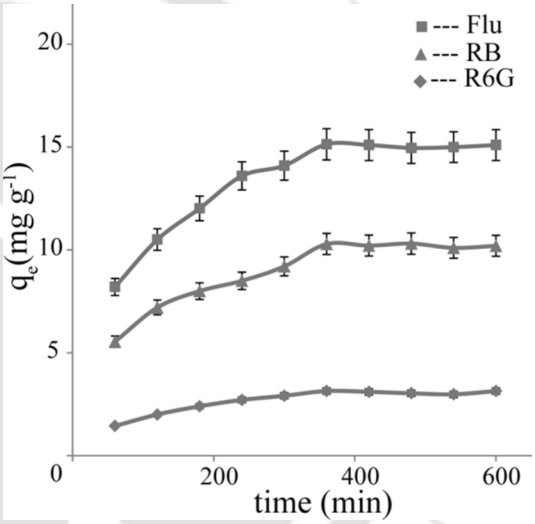

Figure 5.11. Effect of contact time on adsorption of dyes onto Malachite NPs (100 mg L^{-1} dye concentration and Malachite NPs concentration of 5 g L^{-1} at room temperature).

$$\log (q_e - q_t) = \log q_e - (1 / 2.303)\, k_1 t \quad (5.11a)$$

$$(t / q_t) = (1/ q_e^2 k_2) + (t / q_e) \quad (5.11b)$$

Where, q_t and q_e are total adsorption capacity (mg g^{-1}) at time t and at equilibrium respectively. The first and second order rate constants are k_1(min^{-1}) and k_2 (g mg^{-1} min^{-1}) respectively. Putting the data in both the above mentioned model and after calculation, it was found that the second order kinetic model was more favoured having high correlation co-efficient values of R^2=0.9954, R^2=0.9972 and R^2=0.9967 for Flu, RB and R6G respectively (Figure 5.12). The values for k_1 and k_2 obtained from the

equation are summarized in the table (Table 5.5).

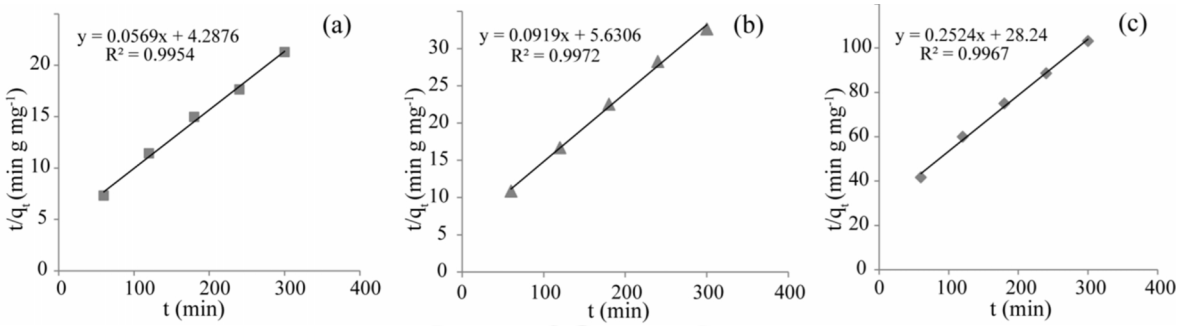

Figure 5.12. Second order kinetics plot (a) Flu, (b) RB and (c) R6G respectively, dye concentration 100 mg L^{-1} and Malachite NPs concentration of 5 g L^{-1} concentration.

The kinetic data were also fitted into the intra-particle diffusion model, an empirical model which gives us the information of the steps within the adsorption process. Initial adsorption always takes place in the exterior of the surface and then diffusion of adsorbate from the exterior surface to the pores of adsorbent happens. The intra-particle diffusion is described by (Eq. 5.11c),[5.27]

$$q_t = K_w t^{1/2} + C \qquad (5.11c)$$

Where K_w is an intra-particle diffusion rate constant and C is the intercept. The high correlation coefficient values ($R^2 > 0.98$) for all the three dye indicates the involvement of the intra-particle diffusion model but then the linearized curve in all the cases do not pass through the origin (Appendix, Figure A5.9) indicating that the intra-particle diffusion is not the only rate limiting factor. Adsorption onto the external surface and intra-particle diffusion are probably working simultaneously.

Table 5.5. Kinetic parameters of the rate of adsorption of the dye on to Malachite NPs.

	First order kinetics		Second order kinetics		Intra-particle diffusion kinetics		
	k_1 (L min^{-1})	R^2	k_2 (g mg^{-1} min^{-1})	R^2	K_w (mg $g^{-1}min^{-0.5}$)	C(mg g^{-1})	R^2
Flu	0.008	0.988	0.076	0.995	0.63	3.4	0.988
RB	0.005	0.987	0.10	0.997	0.36	2.8	0.982
R6G	0.008	0.990	0.40	0.996	0.15	0.27	0.994

5.5.3.4 Effect of solution pH

The surface property of Malachite NPs is highly governed by the pH of the medium. The species distribution of the dye molecules in solution are also greatly influenced by the pH of the solution. With the change in solution pH the protonation/de-protonation equilibrium of the system containing the Malachite NPs and dyes changes which facilitates the adsorption. To see the effect of pH in the adsorption we have studied a pH range of 4 to 9 and tried to carve out a plausible mechanism based on the results obtained and relating with the reported literature. The maximum adsorption was found in the neutral pH regime as evident from the pH dependence plot (Figure 5.13). Flu had the maximum adsorption at pH ~ 7 with q_e value of (15.14 mg g^{-1}) followed by RB with q_e value of (10.28 mg g^{-1}). To get an insight of the mechanism we have considered the surface active groups of the Malachite NPs and species availability of the dye at different pH. These dyes exist in different ionic forms in the solution in different pH. These ionic species of dyes can establish some sort of electrostatic interaction with the groups available on the Malachite NPs surface and regulate the adsorption equilibrium. Flu exists as neutral, monoanionic (carboxylic acid deprotonated species) and dianionic (both carboxyl and hydroxyl group deprotonated species) in solution and the protolytic equilibrium between these three species is expected to be around pH ~ 2, 4.3 and 6.3 respectively.[5.43, 5.44] The first deprotonation takes place at around pH ~ 4.3 which leads to the increment of the monoanionic species in the solution and with the increase in the pH to around ~ 6.3 the dianionic species prevails (Figure 5.14). Furthermore the PZC (point of zero charge) of the Malachite NPs was found to be around pH ~ 7.5 and from the study we have found that the maximum adsorption was found in the pH ~ 7. At pH < PZC of Malachite NPs the strong

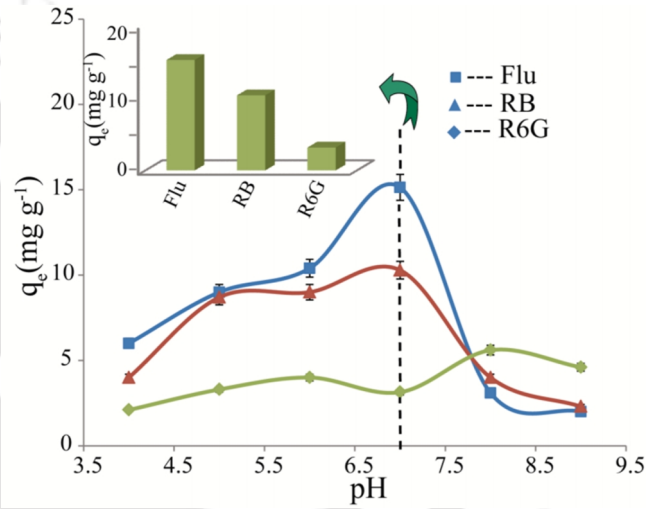

Figure 5.13. Variation of adsorption value q_e (mg g^{-1}) with pH, dye concentration 100 mg L^{-1} and Malachite NPs concentration of 5 g L^{-1} concentration. (Inset q_e values at pH 7).

electrostatic interaction between the positive surface of the Malachite NPs and the highly negative, fully deprotonated species of the Flu might be responsible for this outcome. Both the carboxylate and the phenolate moiety are readily available to facilitate the adsorption by the electrostatic attraction leading to high q_e value. Adsorption value was also found to be higher for the pH ~ 5-6 but was less than that of pH ~ 7. The probable reason behind this might be, though the possibility of electrostatic interaction is there, only one group can assist the attraction (mono-anionic) with the positive Malachite NPs surface. Further with the increase in the pH (pH ~ 8-9) the surface of both the NPs and the Flu dye were both negative and electrostatic repulsion leads to the drastic reduction in the adsorption value. For the case of RB although the carboxyl group gets deprotonated above pH ~ 4 it re-arrange to give the predominant zwitterionic form (Appendix, Figure A5.10).[5.45] Electrostatic interactions between this carboxylate group and the xanthene moiety lead to aggregation for dimers and can hinder the adsorption process.[5.46] This might be the reason for the observed lower adsorption for RB compared to Flu. The adsorption value further decreases as pH increases (8–9) due to the availability of the OH^- in the solution which competes for the $-N^+$ rendering the $-COO^-$ free.[5.47] The surface of the Malachite NPs is also negative at this pH (pH >PZC) and the repulsion of these negative charges further reduces the adsorption quantity. On the other hand R6G is a cationic dye.[5.48] Thus in our study the electrostatic repulsion between the dye and the Malachite surface leads to the reduced adsorptions of the dye. Above pH > PZC of Malachite the surface starts to acquire negative charge and thus adsorption increases to some extent due to the interaction with the cationic dye and also the $-N^+$ group of the R6G can facilitate hydrogen bonding with the hydroxyl group of the malachite which results in an increase in the adsorption value.[5.49]

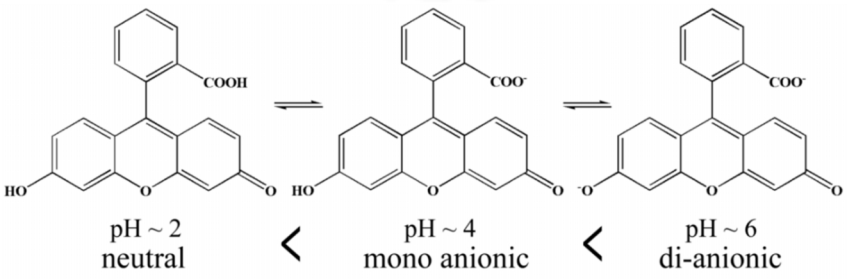

Figure 5.14. Species of Flu that prevails in the solution in our study range.

5.5.3.5 Effect of malachite nanoparticle concentration

The influence of concentration of Malachite NPs on adsorption of the dyes were done in batch mode at pH ~ 7 by varying the Malachite NPs concentration in the range of (0.5 – 3.0) g L^{-1} and the dye concentration was kept constant at 100 mg L^{-1}. With the decrease in the dye to NPs ratio the q_e (mg g^{-1}) was found to decrease (Appendix, Figure A5.11). For the change in the ratio from 0.2 to 0.006 the q_e (mg g^{-1}) was 6.26, 4.93 and 1.47 for Flu, RB and R6G respectively. The total adsorption of the dye was increased with the increase in the concentration of Malachite NPs as the availability of the surface area and the number of sites increased but this amount of increment in the adsorption could not compensate the decrease in the q_e (mg g^{-1}) value (the amount of dye adsorbed per unit mass of adsorbent).

5.5.3.6 Thermodynamics of adsorption

Adsorption at different temperature can give the overview of the favourability of the adsorption system. To study this thermodynamic aspect of the adsorption process, we carried out the study at different temperature from 10 ºC to 40 ºC. The adsorption was found to increase with the increase in temperature for all the cases of the dyes. At 10 ºC the q_e (mg g^{-1}) value was found to be 14.12 (Flu), 9.1 (RB) and 2.88 (R6G) which increased to 15.26 (Flu), 10.89 (RB) and 3.4 (R6G) at 40 ºC (Figure 5.15a). The parameters such as standard Gibbs free energy change (ΔG^o), enthalpy change (ΔH^o) and entropy change (ΔS^o) were also calculated from the following equations,

$$\Delta G^o = - RT \ln (k_c) \quad (5.12a)$$

Where R is the universal gas constant (8.314 J mol^{-1} K^{-1}) and T is temperature in Kelvin. k_c is the equilibrium stability constant, which was calculated at each temperature using the relation,

$$k_c = C_s/C_e \quad (5.12b)$$

Where C_s and C_e are the equilibrium concentration on the adsorbent and the aqueous phase respectively. ΔH^o and ΔS^o were calculated from the slope and intercept of plot between ln (k_c) vs. (1/T) based on Van't Hoff equation (Eq. 5.12c).[5.50]

$$\ln (kc) = (\Delta S^o/R) – (\Delta H^o/R)1/T \quad (5.12c)$$

Van't Hoff plot for Flu adsorption on Malachite surface is given in Figure 5.15b. From the value of ΔH^o, we could ascertain the adsorption as physisorption or chemisorption. The typical value for physisorption usually lies below 84 kJ mol^{-1}, whereas for chemisorption bond strengths lie between 84–420 kJ mol^{-1}.[5.34] The value for ΔH^o obtained from the slope of the straight line equation conform the physisorption of the dyes on to the Malachite NPs with values 7.729, 8.303 and 4.419 kJ mol^{-1} for Flu, RB and R6G respectively (Appendix, Table A5.1). The positive values for enthalpy change (ΔH^o) reflect the endothermic nature of the adsorption process. The ΔS^o value was also found to be positive for all the dyes indicating the affinity of the Malachite NPs towards the dye molecules (Appendix, Table A5.1).[5.51] The spontaneity of the adsorption process was also calculated from the thermodynamic data. The ΔG^o value for all the three dyes was calculated to be negative suggesting the spontaneity of the adsorption process.

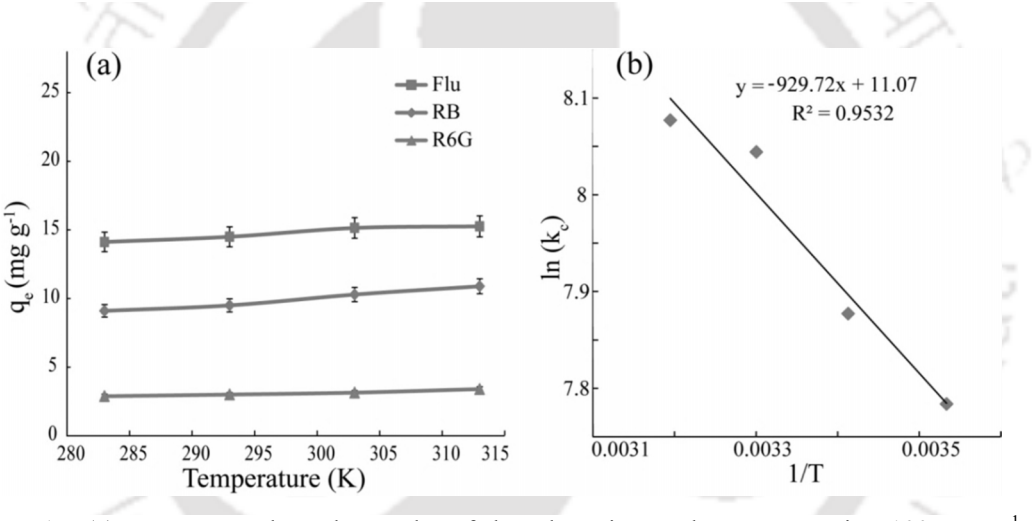

Figure 5.15. (a)Temperature dependence plot of the adsorption at dye concentration 100 mg L^{-1} and Malachite NPs concentration of 5 g L^{-1} concentration; (b) Van't Hoff plot for Flu adsorption on Malachite surface.

5.5.3.7 Desorption and multi-cycle efficiency

After the loading of the dye onto the NPs, their elimination from the surface of the NPs is also imperative for the practical re-usability of the NPs. The desorption phenomena also plays a pivotal role alike the adsorption process. The desorption efficiency determines the usability of the dye through a repeated times without prior decrease in the adsorption properties. For the desorption study, we have used a 20% and 50% ethanol solution todesorb the dye adsorbed onto the Malachite NPs. The 50% ethanol solution gave a better result, as the extraction of the dyes was more profound than the

20% ethanol solution. Flu was desorbed to ~ 99.5% whereas complete extraction of RB and R6G were obtained (Figure 5.16a). The high solubility of the dye in ethanol might be the driving force behind the efficient extraction of the dyes. The re-usability of the NPs was also tested up to three cycles of continuous adsorption and desorption. The adsorption efficiency was found to decrease with the subsequent cycle. After third cycle the relative adsorption (q_e) value decreased to ~95%, ~97% and ~98.1 % for Flu, RB and R6G respectively, considering the adsorption efficiency of first cycle as ~100% (Figure 5.16b).

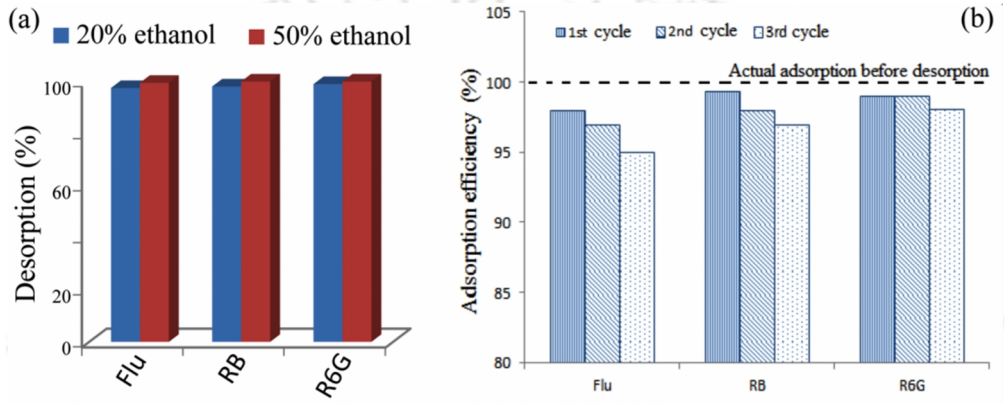

Figure 5.16. (a) Desorption study at 20% and 50% ethanol solution as extractant; (b) Multi-cycle efficiency plot showing the decrease in the efficiency with the number of cycle.

5.6.4 Summary

The result obtained in this study reveals the potentiality of the Malachite NPs as an effective and preferential adsorbent for the removal of organic pollutants. In our earlier work we have established Malachite NPs as an efficient adsorbent for the removal of Arsenate and Chromate. Organic pollutants: Fluorescein (Flu), Rhodamine B (RB) and Rhodamine 6G (R6G) were taken for the study. Flu was favourably adsorbed the most with q_e value ~29.54 (mg g^{-1}) compared to the other two dyes RB q_e value ~ 20.74 (mg g^{-1}) and R6G q_e value~ 6.4 (mg g^{-1}).The maximum adsorption was observed at pH ~7. The dianionic functionality (–COOH and –OH) of Flu seems to play the crucial role in providing the favourable electrostatic interaction compared to the other two dyes RB (–OH) and R6G respectively. The adsorption followed the 2nd order kinetics with external adsorption by monolayer formation which was well accompanied by intra-particle diffusion. Moreover, the proficient desorption was carried out using 50% ethanol solution and the muticycle efficiency of the recovered NPs was well accounted up to

three continuous cycles. Thus the above findings encourage us to explore the Malachite NPs surface further for removal of various pollutants based on their physiochemical diversities and properties.

References

[5.1] (a) C. S. Hurlbut, C. Klein, Manual of Mineralogy, 20th ed.; John Wiley and Sons: New York, 1985. (b) R. L. Frost, Z. Ding, J. T. Kloprogge, W. N. Martens, Thermochimica Acta, 390 (2002) 133-144. (c) N. Salvado, T. Pradell, E. Pantos, M.Z. Papiz, J. Molera, M. Seco, M. Vendrell-Saz, J. Synch. Rad. 9 (2002) 215-222. (d) B. Gilbert, S. Denoel, G. Weberc, D. Allart, Analyst 128 (2003) 1213-1217.

[5.2] I. S. Molchan, G.E. Thompson, P. Skeldon, R. Andriessen, J. Colloid Interface Sci. 323 (2008) 282-285.

[5.3] B. Saha, G. Das, J. Phys. Chem. C. 113 (2009) 15667-15675.

[5.4] G. Gonzaletz, Laskowski, J. Electroanal. Chem. Int. Electrochem. 53 (1974) 452.

[5.5] (a) M.M. Hassan, Health Policy, 74 (2005) 247-260. (b) J. Iqbal, H. J. Kim, J. S. Yang, K. Baek, J. W. Yang, Chemosphere. 66 (2007) 970-976. (c) H. Gecol, E. Ergican and A. Fuchs, J. Membr. Sci. 241 (2004) 105-119. (d) M. Costa, Toxicol. Appl. Pharmacol. 188 (2003) 1-5.

[5.6] G. Bayramoğlu, M.Y. Arica, Chem. Eng. J. 139 (2008) 20-28.

[5.7] C. Raji, T.S. Anirudhan, Water Res. 32 (1998) 3772-3780.

[5.8] A.E. Sikaily, A.E. Nemr, A. Khaled, O. Abdelwehab, J. Hazard. Mater. 148 (2007) 216-228.

[5.9] H. Li, Z. Li, T. Liu, X. Xiao, Z. Peng, L. Deng, Bioresour. Technol. 99 (2008) 6271-6279.

[5.10] D. Mohan and C. U. Pittman, J. Hazard. Mater.142 (2007) 1-53.

[5.11] N. N. Greenwood, A. Earnshaw, Chemistry of Elements, Pergamon Press, Oxford, 1984 (Chapter 13).

[5.12] C. K. Jain, I. Ali, Water Res. 34 (2000) 4304-4312.

[5.13] WHO (World Health Organisation), Environmental Health Criteria, 18: Arsenic, World Health Organisation, Geneva, 1981.

[5.14] M. D. Kiping, J. Lenihan, W. W. Fletcher (Eds.), Arsenic, the Chemical Environment, Environment and Man, vol. 6, Glasgow, 1997, pp. 93-110.

[5.15] N. Kongsricharoern, C. Polprasert, Water Sci. Technol. 34 (1996) 109-116.

[5.16] J. C. Seaman, P. M. Bertsch, L. Schwallie, Environ. Sci. Technol. 33 (1999) 938- 944.

[5.17] J. Hu, G. Chen, I. M.C. Lo, Water Res. 39 (2005) 4528-4536.

[5.18] S. E. Bailey, T. J. Olin, R. M. Bricka, D. D. Adrian, Water Res. 33 (1999) 2469-2479.

[5.19] B. Saha, S. Chakraborty, G. Das, J. Phys. Chem. C. 114 (2010) 9817-9825.

[5.20] A. Agrawal, C. Pal, K. K. Sahu, J. Hazard. Mater. 159 (2008) 458-464.

[5.21] A. I. Zouboulis, K. A. Kydros, K. A. Matis, Sep. Sci. Technol. 28 (1993) 2449-2463.

[5.22] M. Uysal, I. Ar, J. Hazard. Mater. 149 (2007) 482-491.

[5.23] M. Dakiky, M. Khamis, A. Manassra, M. Mer'eb, Adv. Environ. Res. 6 (2002) 533-540.

[5.24] B.M.W.P.K. Amarasinghe, R.A. Williams, Chem. Eng. J. 132 (2007) 299-309.

[5.25] M. H. Kalavathy, T. Karthikeyan, S. Rajgopal, L. R. Miranda, J. Colloid Interface Sci. 292 (2005) 354-362.

[5.26] (a) S. Lagergren, Handlingar, 24 (1898) 1-39. (b) Y. S. Ho, G. McKay, Process Biochem. 34 (1999) 451–465.

[5.27] W. J. Weber, J. C. Morris, J. Sanit. Eng. Div. Am. Soc. Civ. Eng, 89 (1963) 31-60.

[5.28] C. H. Giles, T. H. McEvan, S. N. Nakhwa, D. Smith, J. Chem. Soc. 4 (1960) 3973-3993.

[5.29] I. Langmuir, J. Am. Chem. Soc. 38 (1916) 2221-2295.

[5.30] H. M. F. Freundlich, Z. Phys. Chem. 57 (1906) 385-470.

[5.31] (a) M. M. Dubinin, V. L. Radushkevich, Dokl. Akad. Nauk SSSR, 55 (1947) 331-333. (b) M. Polanyi, Trans. Faraday Soc. 28 (1932) 316-333.

[5.32] S. Hong, C. Wen, J. He, F. Gan, Y-S. Ho, J. Hazard. Mater. 167 (2009) 630-633.

[5.33] S. Chen, Q. Yue, B. Gao, X. Xu, J. Colloid Interface Sci. 349 (2010) 256-264.

[5.34] C.Y. Kuo, C.H. Wu, J.Y. Wu, J. Colloid Interface Sci. 327 (2008) 308-315.

[5.35] S. Dai, M. C Burleigh, Y Shin, C. C Morrow, C. E. Barnes, Z. Xue, Angew. Chem. Int. Ed. 38 (1999) 1235-1239.

[5.36] P. P. Selvam, S. Preethi, P. Basakaralingam, N.Thinakaran, A. Sivasamy, S. Sivanesan, J. Hazard. Mater., 155 (2008) 39-44.

[5.37] S. R. Couto, Biotechnol. Adv. 27 (2009) 227-235.

[5.38] C. K. Huang and P. F. Kerr, The American mineralogist, 4.5 (1960) 311-324.

[5.39] D. Mahanta, G. Madras, S. Radhakrishnan, S. Patil, J. Phys. Chem. B, 113 (2009) 2293-2299.

[5.40] Q. H. Hu, S. Z. Qiao, F. Haghseresht, M. A. Wilson, G. Q. Liu, Ind. Eng. Chem. Res. 45 (2006) 733-738.

[5.41] A. Mittal, L. Kurup, J. Mittal, J. Hazard. Mater. 146 (2007) 243-248.

[5.42] V. K. Gupta, I. Ali, V. K. Saini, Ind. Eng. Chem. Res. 43 (2004) 1740-1747.

[5.43] V. G. Omelyanenko, W. Jiskoot, J. N. Herron, Biochemistry, 32 (1993) 10423-10429.

[5.44] L. D. Lavis, T. J. Rutkoski, R. T. Raines, Anal. Chem. 79 (2007) 6775-6782.

[5.45] K. Shakir, A. F. Elkafrawy, H. F. Ghoneimy, S. G. E. Beheir, M. Refaat, Water Res. 44 (2010) 1449-1461.

[5.46] M. Mohammadi, A. J. Hassani, A. R. Mohamed, G. D. Najafpour, J. Chem. Eng. Data, 55 (2010) 5777-5785.

[5.47] Y. Guo, J. Zhao, H. Zhang, S. Yang, J. Qi, Z. Wang, H. Xu, Dyes Pigments, 66 (2005) 123-128.

[5.48] A. Cvetkovic, A. J. J. Straathof, R. Krishna, L. A. M. van der Wielen, Langmuir, 21 (2005) 1475-1480.

[5.49] S. A. El-Safty , A. Shahat, Md. R. Awual, J. Colloid Interface Sci. 359 (2011) 9-18.

[5.50] S. Pal, S. Ghorai, C. Das, S. Samrat, A. Ghosh, A. B. Panda, Ind. Eng. Chem. Res. 51 (2012) 15546-15556.

[5.51] H. M. H. Gad, A. A. El-Sayed, J. Hazard. Mater. 168 (2009) 1070-1081.

Appendix

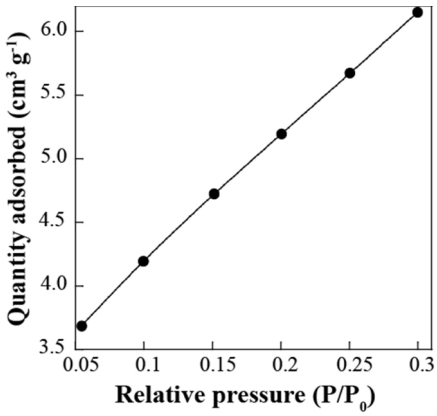

Figure A4.2. N_2 adsorption/desorption isotherms of malachite NPs measured from BET analysis.

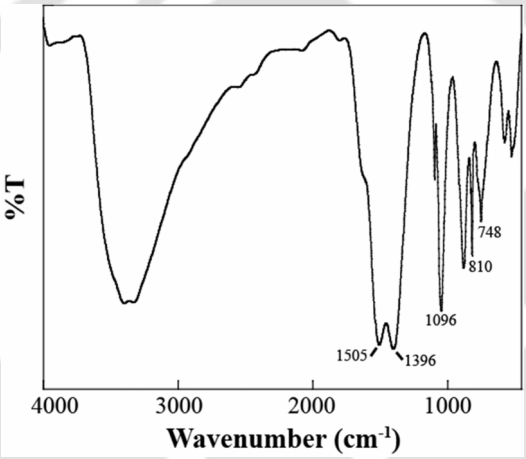

Figure A5.2. FT-IR spectra supporting the formation of malachite nanoparticles.

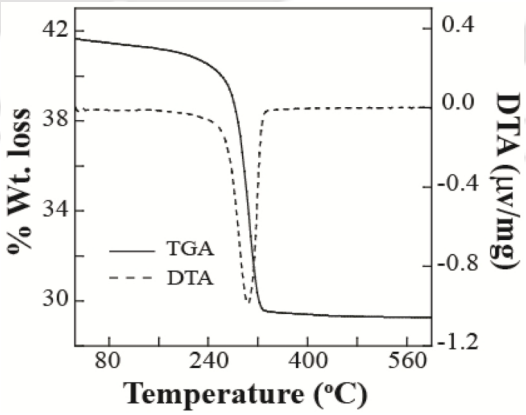

Figure A5.3. Thermogravimetric analysis of the malachite nanoparticles.

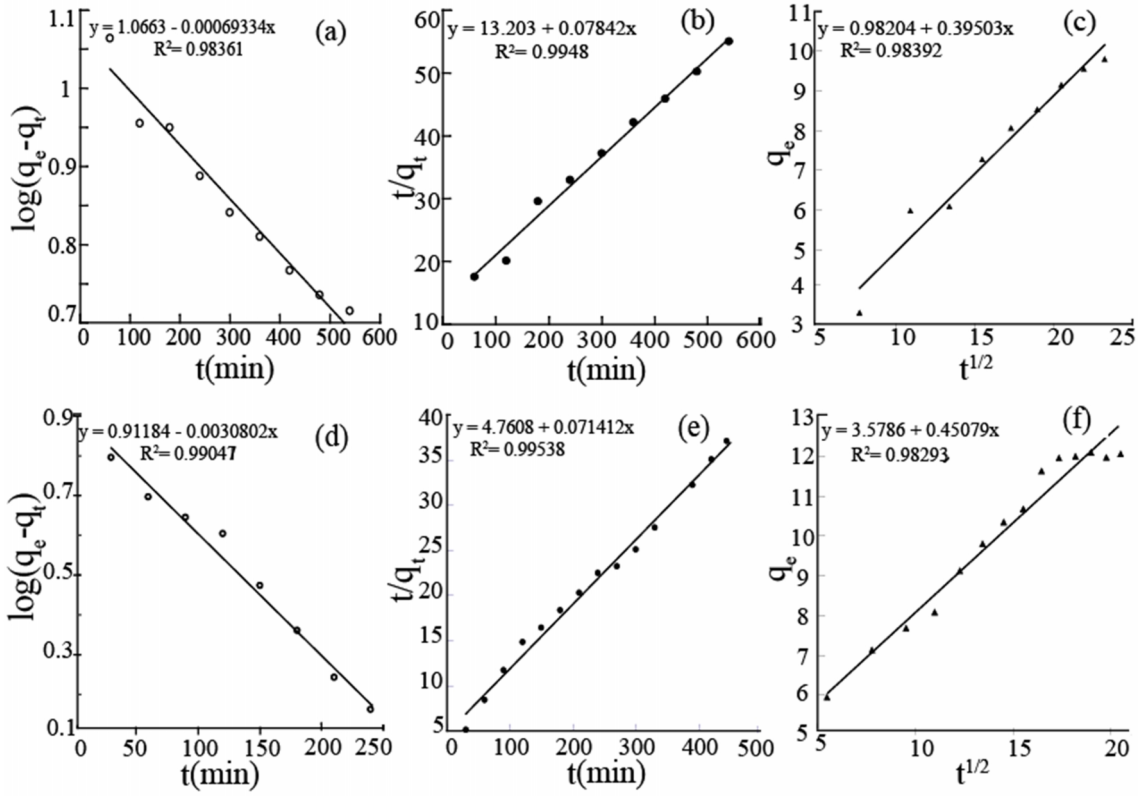

Figure A5.4. Adsorption kinetic plots for adsorption; pseudo-first-order kinetics plot (a) for chromate and (d) for arsenate; Pseudo-second-order kinetics plot (b) for chromate and (e) for arsenate; Intra-particle diffusion kinetics plot (c) and (f) for chromate and arsenate respectively (pH 5; absorbent dosage = 5g L^{-1}; temperature = 30±1 °C; stirring speed = 200 rpm for both).

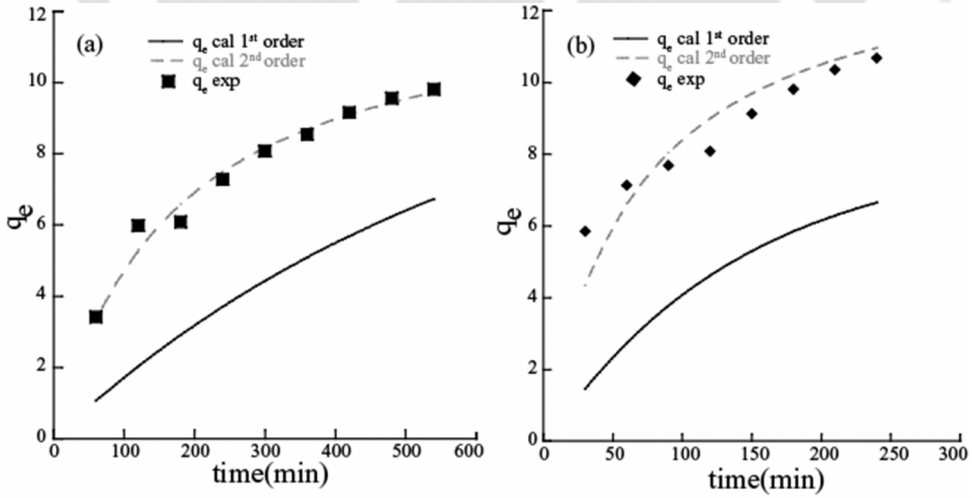

Figure A5.5. Comparison of the q_e values, experimental and calculated from 1st order and 2nd order kinetics.(a) for chromate and (b) for arsenate. From the plot it can be considered that both chromate and arsenate preferentially follow 2nd order kinetics.

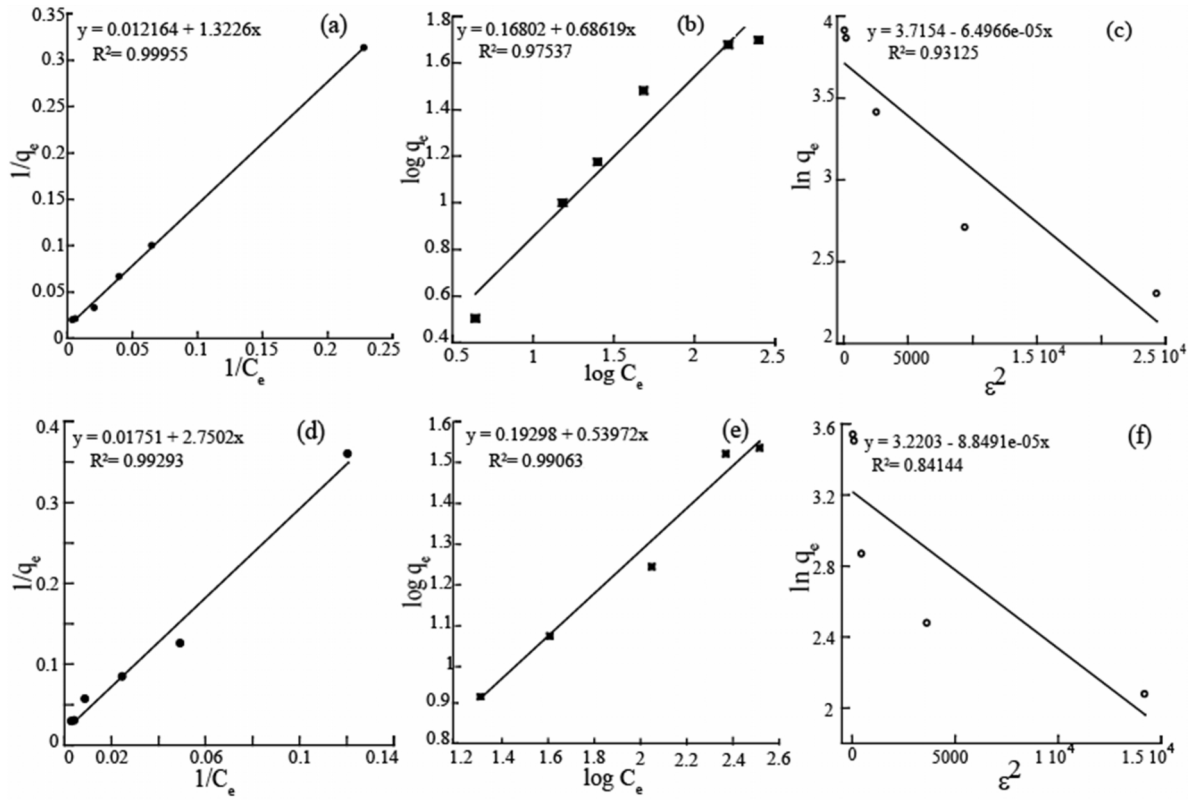

Figure A5.6. Adsorption isotherms plots, Langmuir model (a) for chromate and (d) for arsenate; Freundlich model (b) for chromate and (e) for arsenate; D-R model (c) and (f) for chromate and arsenate respectively (pH 5; absorbent dosage = 5g L^{-1}; temperature = 30±1 ˚C; stirring speed = 200 rpm for both).

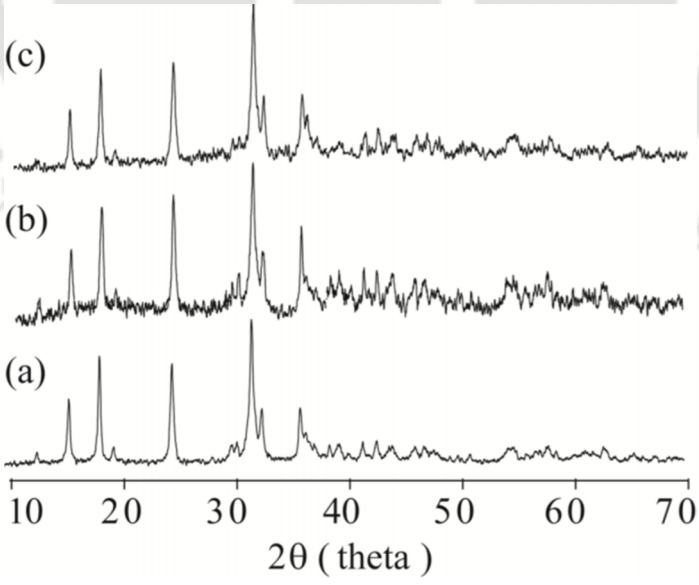

Figure A5.7. PXRD spectra of (a) only malachite NPs and malachite NPs after desorption of (b) arsenate, (c) chromate.

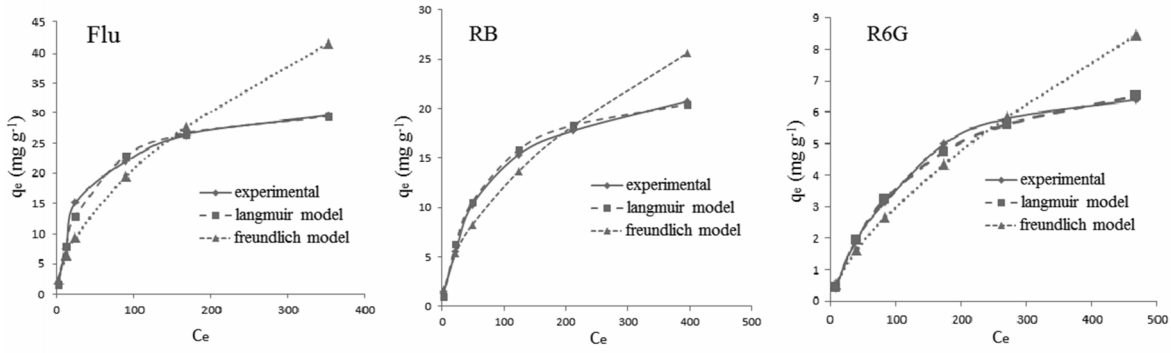

Figure A5.8. Plot for the eperimental and calculated value (from Langmuir and Freundlich isotherm) of q_e for Flu, RB and R6G. [100 mg L^{-1} dye concentration and Malachite NPs concentration of 5 g L^{-1}].

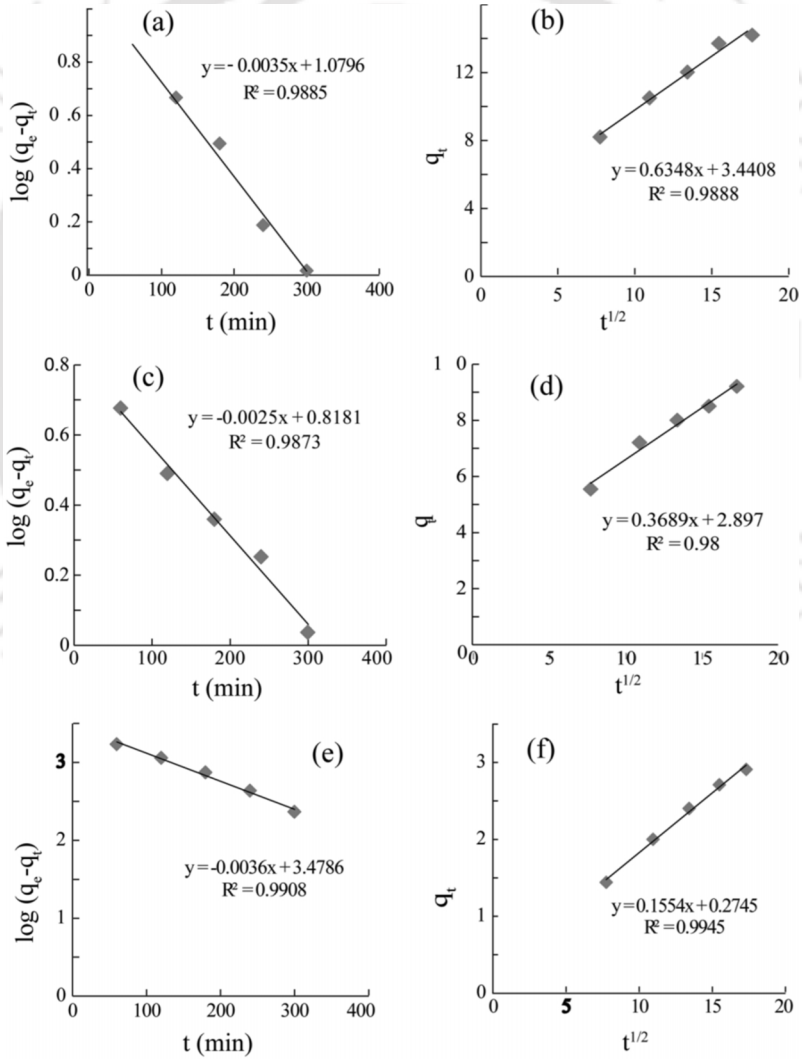

Figure A5.9. First order kinetic plot for (a) Flu, (c) RB, (e) R6G and Intra-particle diffusion plot (b) Flu, (d) RB and (f) R6G respectively.

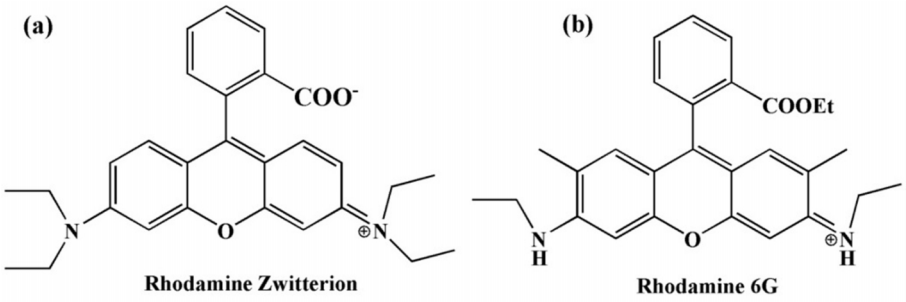

Figure A5.10. Species prevalent in the solution at ~ pH 7 (a) RB and (b) R6G.

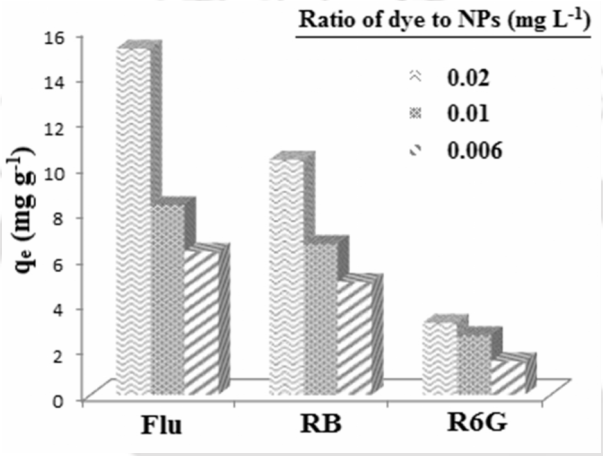

Figure A5.11. Variation of adsorption value with the increase in Malachite NPs concentration [dye concentration was kept constant at 100 mg $L^{-1}$and Malachite NPs was varied to 5, 10 and 15 g L^{-1}respectively].

Table A5.1. Thermodynamic parameters of dye adsorption onto Malachite nanoparticles.

Temp.(K)	Flu			RB			R6G		
	ΔG^o (KJmol^{-1})	ΔS^o (J mol^{-1} K^{-1})	ΔH^o (KJ mol^{-1})	ΔG^o (KJmol^{-1})	ΔS^o (J mol^{-1} K^{-1})	ΔH^o (KJ mol^{-1})	ΔG^o (KJmol^{-1})	ΔS^o (J mol^{-1} K^{-1})	ΔH^o (KJ mol^{-1})
283	-18.31			-16.29			-12.05		
293	-19.18	92.03	7.729	-17.04	0.42	8.303	-12.60	59.12	4.419
303	-20.26			-17.99			-13.16		
313	-21.01			-18.87			-13.84		

Chapter 6

Vaterite-Pollutant interaction

Chapter 6

6.1 Introduction

After studying the interaction of pollutants onto malachite surface this chapter deals with the study of pollutants with another basic 'hard' potential inorganic surface for pollutant removal from aqueous solution which is bio-compatible in nature, calcium carbonate ($CaCO_3$). Three anhydrous crystalline polymorphs of $CaCO_3$ are known viz. Calcite, Aragonite, and Vaterite. Calcite is thermodynamically the most stable species and abundant in nature followed by aragonite and vaterite is the least stable. However, vaterite is a material of high potential application because of its high specific surface area, high solubility, high dispersion, and small specific gravity compared with calcite and aragonite.[6.1] But the formation and stabilization of the vaterite phase is intricate.

Quite a lot of approaches have been taken to deal with synthesis and stabilization of the polymorph, such as initial super saturation, mixing and stirring conditions, temperature, pH, solvents and the presence of organic or inorganic additives.[6.2] In the absence of any additives calcium and carbonate ions precipitates in the aqueous solution to give rhombohedral calcite crystals.[6.3] Whereas vaterite particles could be fabricated using specific additives in a controlled environment. Anionic dendrimer could induce the formation of spherical vaterite particles, double hydrophilic block copolymers were used in the precipitation of spherical or hollow shell vaterite particles in solution.[6.4] Vogel *et al*. synthesized vaterite microspheres using a seeded growth method.[6.5] Microwave-assisted synthesis of vaterite has been reported by Qui *et al*.[6.6] Walsh *et al*. reported a water-in-oil system with SDS for morphosynthesis of vaterite microsponges.[6.7] Amino acids such as glutamic acid and aspartic acid has also been used as an additive for selective vaterite synthesis.[6.8,6.9] Synthetic polypeptides have also been used for the stabilization of the vaterite phase.[6.4] The principle behind this stabilization is arresting the metastable phase by delaying the transformation into the more stable calcite form. Electrostatic interaction of the surface calcium ions of the crystal and the anionic site of the additive is sought to be responsible for the stability of the thermodynamically unfavorable vaterite polymorph. Therefore molecules having suitable site for the calcium ion interaction is a potential additive for stabilizing the

vaterite phase. Organic dye molecule, having carboxylic moiety might prove to be a good candidate in this regard. Our literature survey reveals that not much work have been reported in the synthesis of stable vaterite microspheres using organic dyes. We have used a salicylic acid-aniline dye as an additive in the morphosynthesis of $CaCO_3$ (vaterite). The formation and the lifespan of the metastable vaterite phase were increased upon addition of the dye.

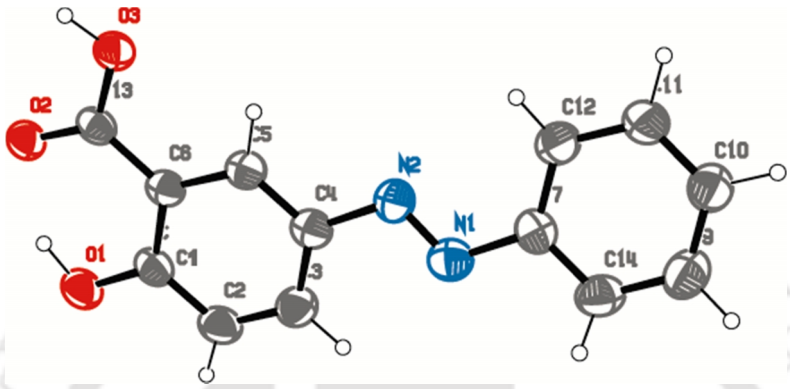

Figure 6.1. ORTEP representation of the dye (**E-2-hydroxy-5-(phenyldiazenyl)benzoic acid**) used for the synthesis of the vaterite.

6.2 Synthesis and characterization of vaterite

A simple co-precipitation method was used for the synthesis of $CaCO_3$ as reported earlier.[6.10] Precipitation was carried out by mixing $CaCl_2$ (20 mM) and Na_2CO_3 (20 mM) in presence of 10 mM dye solution. The dye was added to the Na_2CO_3 solution and then $CaCl_2$ solution was added drop-wise at a flow rate of 5 ml/min with constant stirring. White precipitates appear instantaneously which was then allowed to stir for 30 minutes. The white precipitates were then centrifuged and separated. The obtained precipitates were washed with ethanol and dried prior to characterization.

Synthesized ($CaCO_3$) vaterite were characterized using various analytical techniques. Framboidal vaterite spheres of size ranging 0.5 to 4 μm were the major components of the mineralized $CaCO_3$ precipitates as evident from the SEM micrographs (Figure 6.2a). The FTIR data in Figure 6.2b shows the peak at 1433 cm^{-1} and the characteristic vaterite peak at 746 cm^{-1} and 1089 cm^{-1} corresponding to the occurrence of the vaterite. The PXRD data also reveals the occurrence of pure vaterite phase with almost absence of the other two phases (Figure 6.2c). The BET surface area analysis reveals that the vaterite has specific surface area of 12.266 m^2 gm^{-1} (Appendix, Figure A6.1a). The point of zero charge (PZC) value of vaterite was found to be around pH~8.2 and given in Appendix section of this chapter (Appendix, Figure A6.1b).

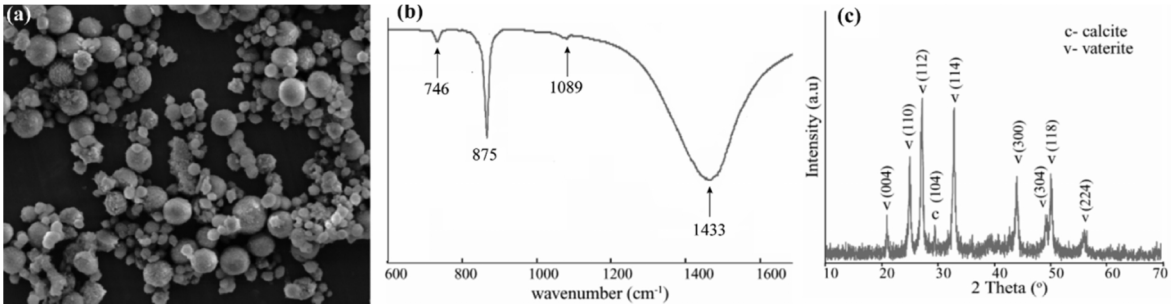

Figure 6.2. (a) SEM micrograph images, (b) FT-IR spectra and (c) PXRD spectra of vaterite.

The stability of the synthesized vaterite was also investigated and the dynamics of the phase transformation was monitored. The vaterite was further allowed to incubate in the reaction mixture and precipitates were drawn out at different time scale. The stability of the vaterite microspheres formed was dominant as observed after incubation for over a week in solution, as apparent from the SEM images in Figure 6.3a. The existence of the peak at 746 cm^{-1} and non occurrence of the calcite peak (712 cm^{-1}) even after incubation of ~4 days support the perseverance of the vaterite phase in presence of the dye (Figure 6.3b). A small calcite peak emerged in the FTIR spectrum only after ~8 days of incubation (Figure 6.3a), which was due to the commencement of the formation of calcite by dissolution of the vaterite microspheres. The detailed analysis of the TEM images (Appendix, Figure A6.2) confirmed that the vaterite microspheres formed were actually aggregates of vaterite nanocrystals. These findings are similar to the findings reported by Ganguli *et al*.[6.11] These nano-vaterites of sizes 20-50 nm self assembles to for larger microspheres of vaterite crystals.

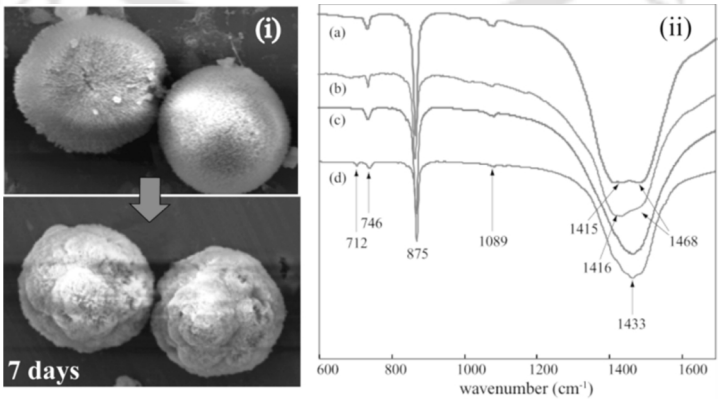

Figure 6.3. (i) SEM images of vaterite microspheres after incubation period of 7 days and (ii) FTIR spectra of $CaCO_3$ taken after (a) 15 mins; (b) 1day; (c) 4 days; (d) 8 days; of incubation respectively.

This chapter has also been divided into two sections:

Part 1: Interaction and removal of inorganic pollutants using vaterite microparticles.

Part 2: Interaction and removal of organic pollutants using vaterite microparticles.

Part 1

6.3 Interaction and removal of inorganic pollutants using vaterite microparticles

6.3.1 Background

The negative impact of arsenate and chromate in the environment has been plenty. We have already discussed the water pollution caused by theses inorganic pollutants. Presence of chromate and arsenate are posing a threat to human health and it sheer removal from water bodies is crucial. Waste water remediation using the method of adsorption has been very effective due to its ease of operational utilities. In the previous chapter, we have used malachite mineral surface for the interaction and removal of these two pollutants from the solution. Malachite was found to be effective in the removal of theses pollutant. As we all know the physio-chemical nature of every surface governs the adsorption interaction nature of the system. So, now we proceed to study another mineral of vast interest and importance for the adsorption interaction and removal study. $CaCO_3$ is a mineral of great choice due to its vast applicability and low cost. Three anhydrous crystalline polymorphs of $CaCO_3$ are known viz. calcite, aragonite, and vaterite. Amongst these, calcite is the thermodynamically the most stable and vaterite is the least. However, vaterite is a material of high potential application because of its high specific surface area, high solubility, high dispersion, and small specific gravity compared with calcite and aragonite.[6.1] In this section, we have elaborated the use of framboidal vaterite microparticles for the removal of arsenate and chromate from the solution. In depth analysis of the adsorption of arsenate and chromate onto vaterite surface has been done.

6.3.2 Materials and method

A stock solution of 500 mg L^{-1} for both the pollutants was taken, from which the concentration of 10-500 mg L^{-1} was made for the adsorption analysis study. Adsorption

study was carried out with 2 ml of the adsorbate and addition of vaterite (1.5 mg ml^{-1}) onto it. Preliminary experiments were done to figure out the optimal conditions for various reaction parameters and also the time to attain the steady state. The experiments were performed in duplicate for data consistency. The pH was maintained using 0.1 M NaOH and 0.1 M HCl solution. The ionic strength was maintained constant using 0.05 M NaCl in all the cases otherwise mentioned. Also to see the effect of the pH in the adsorption profile we have considered the range of pH 5-9. Desorption efficiency was also monitored at higher pH range of 10-12.

6.3.3 Results and Discussion

6.3.3.1 Adsorption properties

The vaterite surface was found to be effective for the interaction and removal of arsenate and chromate from solution. Both arsenate and chromate shows a high degree of adsorption. The adsorption amount of chromate was higher than that of arsenate as obtained from individual system of study. The q_e (mg g^{-1}) values were found to be 34.29 mg g^{-1} for arsenate and 58.56 mg g^{-1} for chromate at pH~6. The adsorption profile is given in Figure 6.4a. The EDX spectra confirm the presence of arsenate and chromate onto the vaterite surface after adsorption (Figure 6.4b).

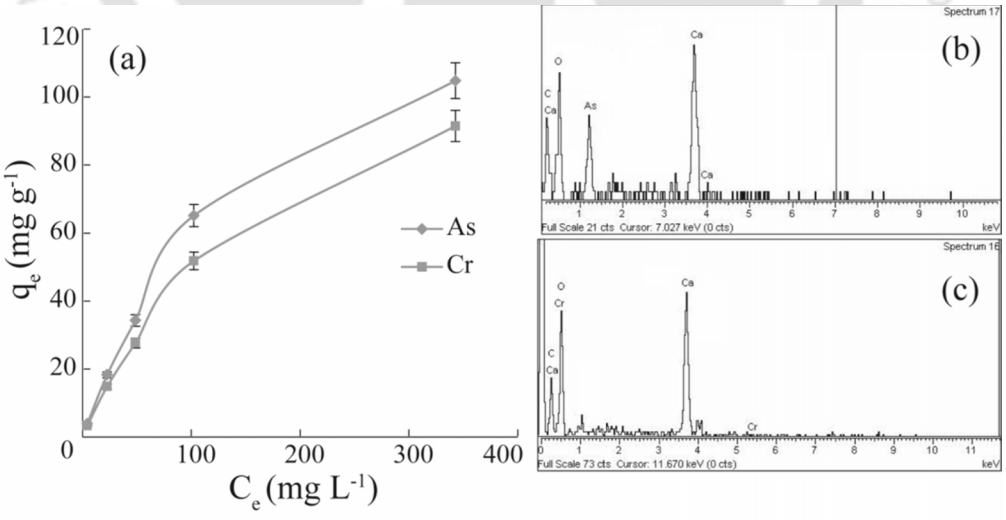

Figure 6.4. (a) Adsorption isotherm of the adsorption of arsenate and chromate onto vaterite surface. EDX spectra confirming the presence of (b) arsenate and (c) chromate after adsorption onto vaterite.

6.3.3.2 Effect of pH

The pH of the solution affects the surface charge of the adsorbents as well as the degree of ionization of different pollutants. The hydrogen ion and hydroxyl ions are adsorbed quite strongly and therefore the adsorption of other ions is affected by the pH of the solution. Change of pH affects the adsorptive process through dissociation of functional groups on the adsorbent surface active sites. This subsequently leads to a shift in reaction equilibrium characteristics of adsorption process. Therefore it is very crucial to monitor the adsorption at different pH and draw a plausible interplaying mechanism out of it. From the data obtained for adsorption in the pH range of 5-9 it was quite evident that the adsorption was more profound in the acidic range (Figure 6.5). Both arsenate and chromate shows an elevated adsorption profile in the acidic range. The q_e value was found to be maximum with 34.29 mg g^{-1} for arsenate and 58.56 mg g^{-1} for chromate at pH~6 onto vaterite surface. A drastic decrease in the adsorption capacity value was observed above the pH > $PZC_{vaterite}$ (pH~9) for both the adsorbents. The negative surface of vaterite above its PZC could hinder the adsorption of these anionic pollutants at that pH.

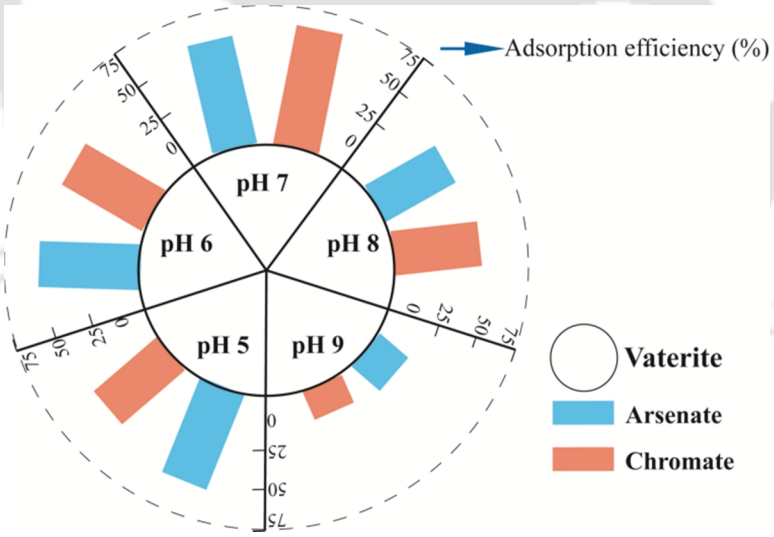

Figure 6.5. Adsorption profile of arsenate and chromate on vaterite surface at different pH.

The adsorption was found to be high in the acidic pH regime whereas with the increase in pH a declination in the adsorption profile was observed. To ascertain a plausible mechanism undergoing in the adsorption process it is necessary to consider the physio-chemical properties of the adsorbate and the adsorbent at that given pH. It is obvious

that arsenate and chromate adsorption on vaterite shows a maximum of arsenate removal in a pH range 5-8, and thereafter decreases as the pH increases above 8 (Figure 6.5). From the species availability of arsenate and chromate and the PZC of vaterite a plausible interaction mechanism can be carved out. Arsenate and chromate are anionic pollutants and exists in different ionic forms at different pH in solution. As(V) ion occurs mainly in the form of $H_2AsO_4^-$ in the pH range between 3 and 6, while a divalent anion $HAsO_4^{2-}$ dominates at higher pH values and for Cr(VI), $HCrO_4^-$ and $Cr_2O_7^{2-}$ are the prevalent species in the pH range 3-6 and CrO_4^{2-} predominate at higher pH.[6.12] At a pH value lower than pH_{PZC} of vaterite (i.e. at pH<8.21) the surface of vaterite are protonated and positively charged surface are more susceptible for arsenate and chromate species available in the solution. Above the pH_{PZC} of vaterite the surface acquires negative charge and the anionic species ($HAsO_4^{2-}$ and CrO_4^{2-}) encounters electrostatic repulsion and hence reduction in the adsorption capacity was observed.

6.3.3.3 Adsorption steady state and kinetic model

In order to get insight into the mechanism of adsorption, as well as potential rate controlling steps, different kinetic models were used for fitting kinetic data. Figure 6.6 shows the adsorption profile of arsenate and chromate versus time. The steep slope at the earlier phase indicates a rapid adsorption onto the surface which became steady after time. The steady state equilibrium time for both arsenate and chromate was different. Arsenate equilibrium time was found to be ~90 minutes whereas the steady state equilibrium for chromate was attained after ~105 minutes.

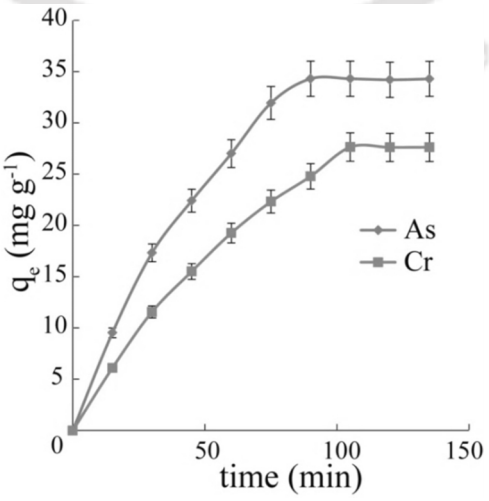

Figure 6.6. Effect of contact time on adsorption of arsenate and chromate onto vaterite surface.

The dynamics of the adsorption can be studied by the kinetics of adsorption in terms of the order of the rate constant.[6.13] The adsorption rate is an important factor for a better choice of material to be used as an adsorbent; where the adsorbent should have a large adsorption capacity and a fast adsorption rate. Most of adsorption studies used pseudo-first-order and pseudo-second-order models to study the adsorption kinetics. An additional model that considers the intraparticle diffusion into account is also considered. The pseudo-first-order or Lagergren first order (Eq. 6.2a) and pseudo-second-order or Ho–McKay kinetic model (Eq. 6.2b) was used to deduce the kinetic mechanism for the adsorption.[6.14]

$$\log (q_e - q_t) = \log q_e - (1 / 2.303)\, k_1 t \qquad (6.2a)$$

$$(t / q_t) = (1/ q_e^2 k_2) + (t / q_e) \qquad (6.2b)$$

Where, the q_t and q_e (mg g^{-1}) are total adsorption capacity at time t and at equilibrium respectively. k_1 and k_2 are first and second order rate constant respectively. The experimental data fitted to these equations gave the rate constant value. The obtained values are summarized in Table 6.1. Usually the best-fit model can be selected based on the linear regression correlation coefficient R^2 values and from the plot it was established that the pseudo-second-order was more followed compared to the pseudo-first-order rate kinetics model. The R^2 values for the pseudo-first-order model were found to be $R^2_{Arsenate}$=0.929 and $R^2_{Chromate}$=0.974, while the values of R^2 for the pseudo-order-second order model were $R^2_{Arsenate}$=0.992 and $R^2_{Chromate}$=0.997, indicating the conformity of pseudo-second-order model for both the cases (Figure 6.7).

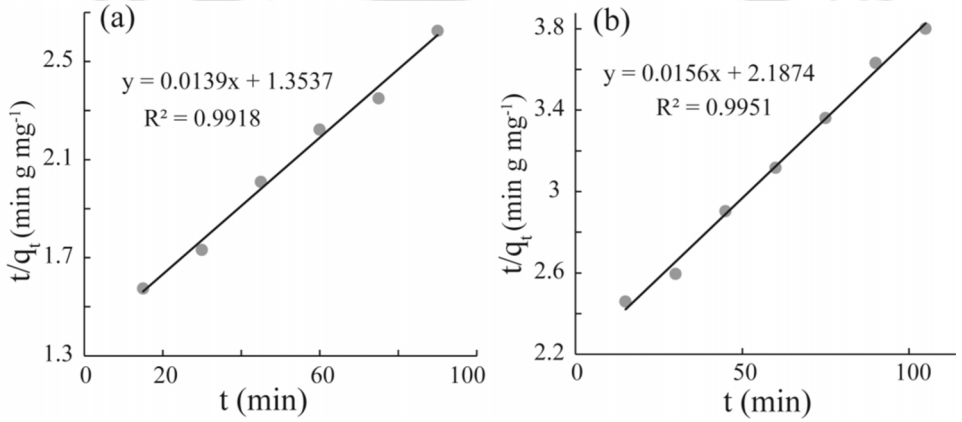

Figure 6.7. Kinetic 2nd order plot showing high fitting values of linear regression correlation coefficient R^2 (a) arsenate and (b) chromate.

However, the pseudo-second-order equation describes kinetics data through generalized approach, and observes process as one rate-controlling step which could not identify the contribution of diffusional processes. Thus, to predict the actual rate-controlling step involved in the adsorption process of arsenate and chromate onto vaterite, the intra-particle Weber–Morris diffusion model was also applied. The intra-particle diffusion is described by (Eq. 6.2c).[6.15]

$$q_t = K_w t^{1/2} + C \qquad (6.2c)$$

Where K_w is an intra-particle diffusion rate constant and C is the intercept. Results of intra-particle Weber–Morris diffusion model showed a linear plot for both arsenate and chromate. The R^2 values for both the pollutants was found to be high suggesting the involvement of the intra-particle diffusion mechanism. The linear plot does not pass through the origin suggesting that intra-particle diffusion is not the sole rate-limiting step (Appendix, Figure A6.3). Compilation of the results obtained from the above models suggests that the adsorption on to the surface and the intraparticle diffusion are occuring simultaneously.

Table 6.1. Kinetic parameters of the rate of adsorption of the dye onto vaterite surface.

	First order kinetics		Second order kinetics		Intra-particle diffusion kinetics		
	k_1 (L min^{-1})	R^2	k_2 (g mg^{-1} min^{-1})	R^2	K_w (mg $g^{-1}min^{-0.5}$)	C(mg g^{-1})	R^2
Arsenate	0.036	0.929	1.4×10^{-4}	0.992	4.70	9.37	0.988
Chromate	0.026	0.974	1.2×10^{-4}	0.997	3.35	6.84	0.999

6.3.3.4 Adsorption isotherm

Adsorption isotherms are important for the description of how molecules of adsorbate interact with adsorbent surface. Hence, the adsorption of arsenate and chromate onto vaterite is determined as a function of equilibrium pollutant concentration (C_e) and the corresponding adsorption isotherm (Figure 6.4).The adsorption process is normally described by the Langmuir and the Freundlich isotherms.[6.16,6.17] The Langmuir equation assumes that there is no interaction between the adsorbate molecules and that the

sorption is localized in a monolayer. It is then assumed that once a pollutant molecule occupies a site, no further adsorption can take place at that site. The Langmuir equation is expressed as,

$$q_e = Q_m b C_e/(1+bC_e) \quad (6.3a)$$

where C_e is the equilibrium concentration of dye solution (mg L^{-1}), q_e is the equilibrium capacity of dye on the adsorbent (mg g^{-1}), q_m is the monolayer adsorption capacity of the adsorbent (mg g^{-1}), and b is the Langmuir adsorption constant (L mg^{-1}) and related to the free energy of adsorption. The Freundlich adsorption model assumes that adsorption takes place on heterogeneous surface and can be written as,

$$q_e = K_f C_e \, 1/n \quad (6.3b)$$

where K_f and *n* (dimensionless) are the Freundlich adsorption isotherm constants, indicated the capacity and intensity of the adsorption, respectively. The experimental data were fitted to the above equations. The isotherm constants and correlation coefficients were calculated and listed in Table 6.2.

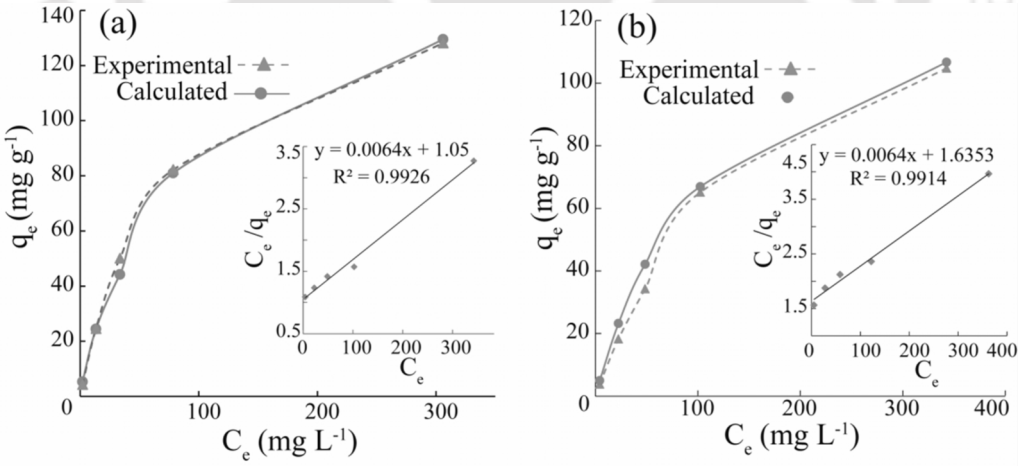

Figure 6.8. Adsorption isotherm plot for (a) arsenate and (b) chromate onto vaterite, q_e values compared were obtained from Langmuir isotherm and experimental finding; (inset: Langmuir plot for (a) arsenate and (b) chromate respectively).

By comparing the correlation coefficients R^2, it can be deduced that the experimental equilibrium adsorption data are well described by the Langmuir equation compared to Freundlich model for both the cases. This suggests the monolayer coverage of the

surface of vaterite microparticles by arsenate and chromate molecules. The maximum adsorption capacity of vaterite for arsenate and chromate was found to be 154.1 and 156.3 mg g^{-1} respectively.

Another important parameter, a dimensionless constant called "constant separation factor" or "equilibrium parameter", R_L defined as

$$R_L = 1/ (1+ b C_0) \quad (6.3c)$$

where, b is the Langmuir coefficient and C_0 is the initial dye concentration, can give some indication of the feasibility of the adsorption process. For a favourable reaction process, $0< R_L<1$; whereas R=0 for the irreversible case, R=1 for the linear case and R>1 for unfavourable reaction. The values for arsenate and chromate adsorption onto vaterite was found to be 0.60 and 0.49 respectively which indicates the favorability of the adsorption process (Table 6.2).

Table 6.2. Adsorption isotherm parameters of arsenate and chromate adsorption onto Vaterite.

	Langmuir isotherm				Freundlich isotherm		
	Q_m (mg g^{-1})	b (L mg^{-1})	R^2	R_L	K_f (mg g^{-1})	n	R^2
Arsenate	154.1	0.006	0.993	0.60	2.07	1.39	0.968
Chromate	156.3	0.004	0.992	0.49	1.01	1.26	0.989

6.3.3.5 Thermodynamic of the adsorption

To determine the temperature effect of the arsenate and chromate adsorption onto vaterite, adsorption experiments were performed at 283, 293, 303 and 313 K. Adsorption isotherms do not have any intrinsic thermodynamic definition, and its significance depends on conditions of the system under study. Anyway, empirical approach, applied for calculation of thermodynamic data, provides the data necessary for understanding of adsorption process. The adsorption values were found to increase with the rise in temperature for both arsenate and chromate (Figure 6.9a). The standard Gibbs free energy change (ΔG^o) was calculated from the following equation,

$$\Delta G^o = – RT \ln (k_c) \quad (6.4a)$$

Where R is the universal gas constant (8.314 J mol^{-1} K^{-1}) and T is temperature in Kelvin. k_c is the equilibrium stability constant, which was calculated at each temperature using the relation,

$$k_c = C_s/C_e \quad (6.4b)$$

where, C_s and C_e is the equilibrium chromate and arsenate (in respective cases) concentration on adsorbent and aqueous phase, respectively. The Gibbs free energy changes (ΔG^o) in this temperature range were calculated from Eq. 6.4a, and are given in Table 6.3. The negative values of ΔG^o suggest that the adsorption process is spontaneous and thermodynamically favourable.[6.18] The average standard enthalpy change (ΔH^o) and entropy (ΔS^o) were determined from Van't Hoff equation (Eq. 6.4c),

$$\ln k_c = \Delta S^o/R - (\Delta H^o)/RT \quad (4c)$$

ΔH^o and ΔS^o was calculated from the slope and intercept of plot between ln (k_c) vs. (1/T) based on Van't Hoff equation. Figure 6.9b is the Van't Hoff plot for arsenate and chromate adsorption onto vaterite.

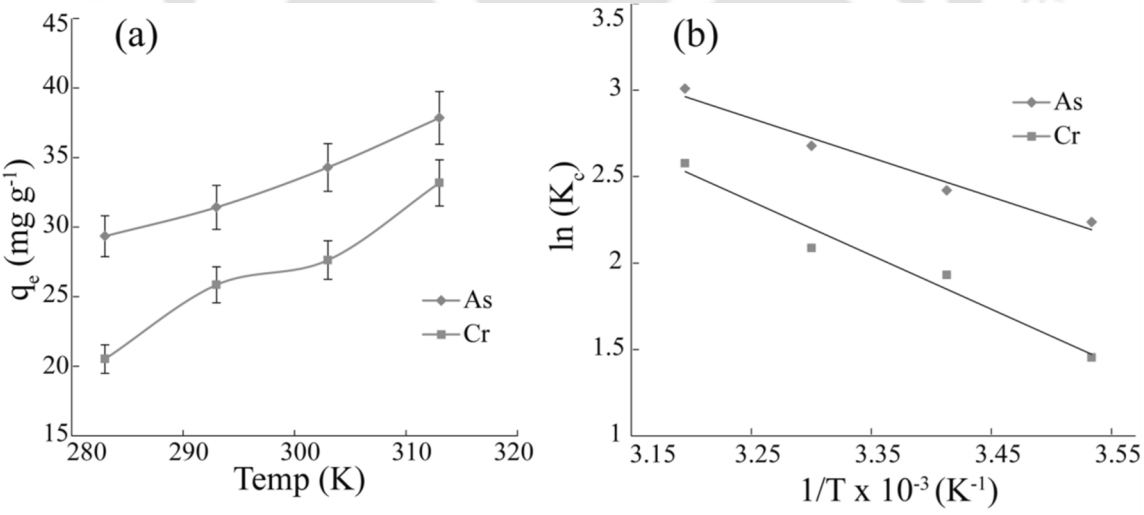

Figure 6.9. (a)Temperature dependence plot of the adsorption of arsenate and chromate. (b) Van't Hoff plot for the adsorption at different temperatures.

Calculated thermodynamic parameters are presented in Table 6.3. The negative values of Gibbs free energy and positive standard entropy changes indicate exothermic and

spontaneous nature of adsorption process on vaterite, and spontaneity of adsorption increases at higher temperature for both the pollutant. The positive values of ΔH^o for both arsenate and chromate indicate the endothermic nature of the adsorption process with more preferable adsorption at higher temperature. The changes in entropy values were positive, indicating an increase in randomness of the system, i.e. arsenate and chromate adsorptions are entropy-driven process.

Table 6.3. Thermodynamic parameters of arsenate and chromate adsorption onto vaterite micro-particles.

Temp. (K)	Arsenate			Chromate		
	ΔG^o (KJ mol^{-1})	ΔS^o (J mol^{-1} K^{-1})	ΔH^o (KJ mol^{-1})	ΔG^o (KJ mol^{-1})	ΔS^o (J mol^{-1} K^{-1})	ΔH^o (KJ mol^{-1})
283	-5.263	18.851	84.844	-3420	25.926	103.85
293	-5.893			-4703		
303	-6.744			-5256		
313	-7.828			-6704		

6.3.3.6 Desorption

Desorption studies help to elucidate the mechanism of adsorption and recovery of the adsorbate and adsorbent. Regeneration of adsorbent makes the treatment process economical. The trend in the desorption process at different pH values is just converse to that of the adsorption process in the pH effect. It was expected that increased concentration of OH^- ions should compete with the already present arsenate and chromate on vaterite surface, hence sodium hydroxide solution has been used as desorbing agent. We have used three different pH range of 10-12 for the desorption study of these pollutants. Desorption was found to be more efficient at higher pH. The desorption efficiency for arsenate was found to be ~57%, ~63%, 69% and for chromate ~51%, ~59%, ~70.2 at pH 10, 11 and 12 respectively (Figure 6.10). The probable reason behind this increased desorption at basic pH range is due to the electrostatic repulsion of the surface (pH > PZC) with these anionic pollutants and also the increased OH^- ions are available for competition with these pollutants for the available interacting sites.

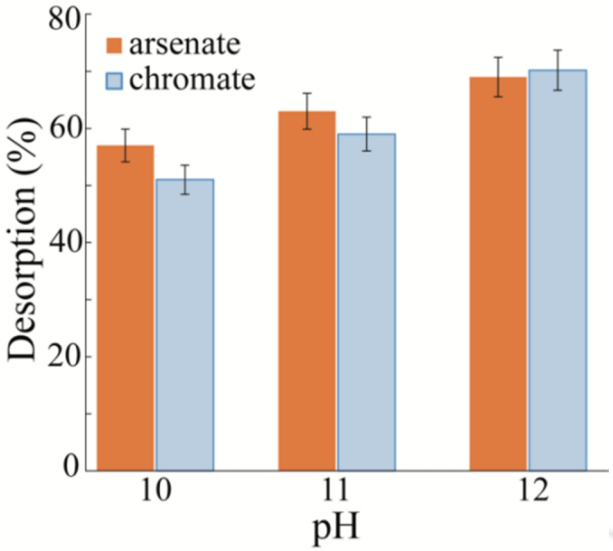

Figure 6.10. Desorption plot of arsenate and chromate showing different desorption behavior at different pH**.**

To monitor whether the adsorption has brought about any changes to the surface of vaterite PXRD spectra of the vaterite after desorption of the pollutants was taken. Desorption experiments have been discussed in details in the next section. A minute change in the PXRD spectra was observed for both the cases of arsenate and chromate adsorption as shown in Figure 6.11. Emergence of a small calcite fragment has been observed for both the cases. Although our as-synthesized vaterite micro-particles were stable in solution (as reported in synthesis and characterization section) but a probable interaction between the arsenate and chromate with the vaterite could trigger the transformation of small fraction of vaterite into calcite.

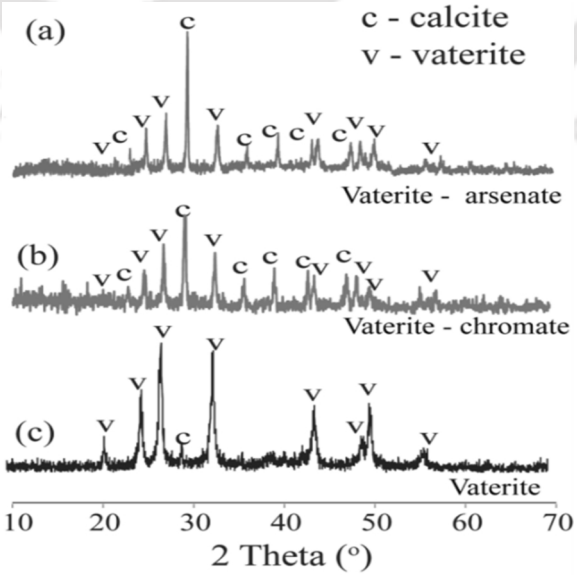

Figure 6.11. PXRD spectra after of the vaterite particles taken after the desorption of arsenate and chromate.

6.3.4 Summary

The summary from this section clearly indicates the possible use of framboidal vaterite microspheres for anionic pollutant removal. Another inorganic surface vaterite has been explored in this regard and was found to be effective in removing arsenate and chromate from aqueous solution. The adsorption phenomenon was governed by the pH of the medium. The adsorption was higher at pH 6-7, for both arsenate and chromate. The adsorption capacity increases with the increase in initial pollutant concentration. The kinetic of the adsorption followed the pseudo-second-order model. A good agreement between Langmuir isotherm and experimental data suggest monolayer coverage of arsenate and chromate upon adsorption onto the vaterite surface. The maximum adsorption capacity (Q_m) was calculated to be 154.1 and 156.3 mg g^{-1} for arsenate and chromate respectively. The pollutant adsorption has been found to be thermodynamically favourable. Desorption was efficiency was found to be moderately good.

Part 2

6.4 Interaction and removal of organic pollutants from aqueous solution using framboidal vaterite as adsorbent

6.4.1 Background

Water pollution is one of the major causes of concern in the present era and various anthropogenic factors have led to the major exhaustion of the water system as a whole. We have already discussed the factors leading to the contamination of the water bodies and its adverse effect on human health in the previous chapter. We have also reported the promising facet of adsorption for dye removal from aqueous solution. We have given some examples of application of various inorganic surfaces for dye removal. To add a few are, for example activated carbon is used and is found to have a good adsorption capacity for the dyes but the high cost effectiveness of the compound makes it reluctant for application in large scale.[6.19] Many inorganic mineral surfaces have also been exploited for the same purpose. Silica was used as adsorbent for the removal of cationic dye by McKay *et al.*[6.20] Perlite was used for the removal of Methylene Blue.[6.21] Natural phosphate, hydroxyapatite and titania was also applied for the removal study of waste water dyes.[6.22-6.24] Clay minerals like bentionite, montmorillonite, smectite,

kaolinite, sepiolite, and zeolite etc. were also employed for removing the dyes from waste water.[6.25] Boujaady *et al.* reported the use of synthetic calcium phosphate for the removal of textile dye.[6.26] Different inorganic mineral surfaces behave differently when introduced with different dyes. It is therefore necessary to know the in-depth detail of the mechanism which is the outcome of the surface characteristics and the physio-chemical properties of the adsorbate and the adsorbent. In the earlier chapter we have studied the malachite surface for the removal of dyes from aqueous solution. In this section we are exploring another inorganic surface, vaterite (a polymorph of $CaCO_3$), for the removal study of dyes from solution.

This present study focuses the use of framboidal vaterite particles for the effective removal of dyes from aqueous medium. The as-synthesized vaterite particles are highly porous and have high surface area. Furthermore the point of zero charge (PZC) value for the vaterite was calculated to be pH~8.21. Therefore, this surface might prove to be a potential candidate for the anionic dye removal via electrostatic attraction. Keeping this in mind, we have considered to study the adsorption of anionic and cationic dyes onto vaterite and to see how the adsorption profile behaves. Eriochrome Black T (EBT), Congo Red (CR) as anionic dyes, Methylene Blue (MB) and Rhodamine 6G (R6G) as cationic dyes were taken for the study. Batch experimental studies were carried out under various parameters such as pH, adsorbent dosage, contact time, initial dye concentration and temperature. The kinetic data obtained from experimental result was tested by the pseudo-first-order and the pseudo-second-order kinetic models. The equilibrium data were evaluated using Langmuir, Freundlich isotherm models and the thermodynamics of the adsorption was also calculated to get the details of the adsorption process.

6.4.2 Materials and methods

Dye stock solution of 500 mg L^{-1} was prepared and different desired concentration (10, 50 100 and 200) was done by proper dilution and a volume of 2 ml was taken for the study. After addition of vaterite (1.5 mg L^{-1}) to the dye of varied concentration, the vials were then kept under stirring until steady state was reached. Preliminary experiments were done to figure out the optimal conditions for various reaction parameters. The experiments were performed in duplicate for data consistency. The pH of was maintained using 0.1 M NaOH and 0.1 M HCl solution. The ionic strength was

maintained constant using 0.05 M NaCl in all the cases otherwise mentioned. The pH in the range 5-9 was monitored to see the effect of pH on the adsorption process. To see desorption efficiency of the framboidal vaterite microspheres we have incubated the dye loaded vaterite particles in 50% ethanolic solution.

6.4.3 Results and Discussion

6.4.3.1 Effect of pH

The pH of the medium highly influences the surface properties and the physio-chemical behavior of the adsorbate which controls the adsorption capacity of any substrate in that medium. To study the effect of pH we have considered a pH range of 5-9. The adsorption profile was different for different dyes. The anionic dye showed a higher adsorption in the acidic range and the cationic dyes were comparatively less adsorbed in the lower pH range. Figure 6.12 gives the statistical overview of the q_e value with the pH of the medium. EBT and CR showed the highest adsorption value of 72.2% and 81% at pH~5 respectively. MB showed the least adsorption value of 16% and R6G was adsorbed only 14% of the total value. With the increase in the pH the adsorption pattern of the anionic dyes showed a downhill curve. Above the PZC of vaterite at pH~9 the adsorption profile was found to be inversed.

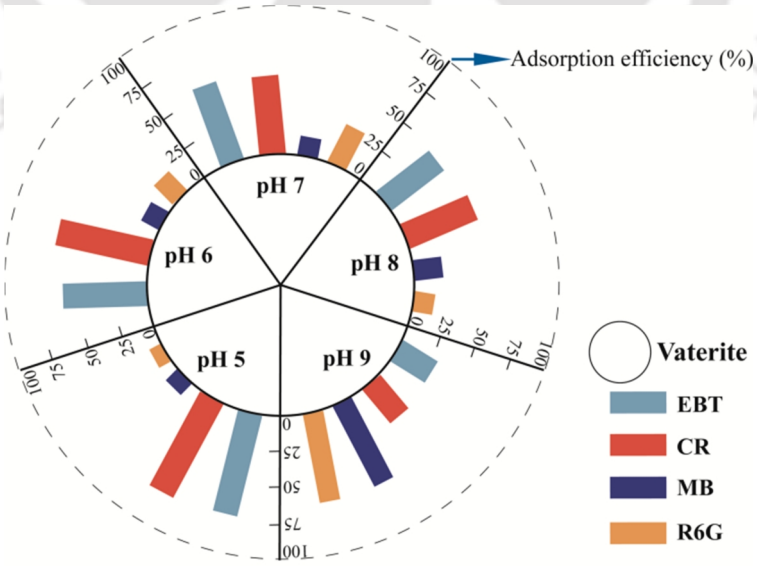

Figure 6.12. pH adsorption profile of various dye onto vaterite surface.

The plausible mechanism for adsorption could be drawn out from the respective species of dyes available in the solution at definite pH. Considering the pH_{PZC} value of the vaterite an overview of the probable mechanism can be figured out. The PZC of vaterite was found to be around pH~8.2 and above which the surface will be negative and below this pH the surface shall behave positively. Considering the anionic dyes, EBT contains sulphonic group which remains ionized in all of the pH ranges studied here. AT lower pH, hydrogen bonding and surface complexation via sulfonic acid group of EBT with the positive surface of the vaterite is responsible for the observed adsorption value. With the increase in pH (~6.3) and above the first deprotonation (pk_a 1) of one of the hydroxyl group occurs.[6.27] Thus surface through hydrogen bonding as well as electrostatic interaction through its partially charged hydroxyl groups with the positive surface of the vaterite favors the increased adsorption in this pH range. As the pH of the system was increased to 9 the surface of the vaterite becomes negative and thus leads to the decreased in the adsorption value due to the repulsion from the negative surface of vaterite and the negative species of the dye. Similar sort of adsorption interaction was also justified for the case of CR. At lower pH of our study range the surface of CR was negative as the pK_a value was around 4.5-5.5.[6.28] The vaterite surface was positive below the $PZC_{vaterite}$ which facilitates the favorable electrostatic interaction for the adsorption. For the cationic dyes MB and R6G at lower pH range they remains positive and the surface of the vaterite also remains positive which promotes the electrostatic repulsion between them and thus hinders the adsorption.[6.29,6.30]

6.4.3.2 Adsorption steady state and kinetic model

The rate of uptake of the adsorbate onto the adsorbent surface controls the equilibrium time for the adsorption of the system. This rate of kinetics is required for selecting optimum operating conditions for the full-scale batch process.[6.31] Figure 6.13 shows the plot of dye adsorption versus contact time. The plot indicates that the adsorption was rapid at the early phase of the process which then slowed with further increase in contact time until a steady state was achieved. The equilibrium time varied for the dyes. The steady state for EBT was achieved within ~105 minutes while for CR, MB and R6G it took ~120 minutes to achieve the steady state of the adsorption.

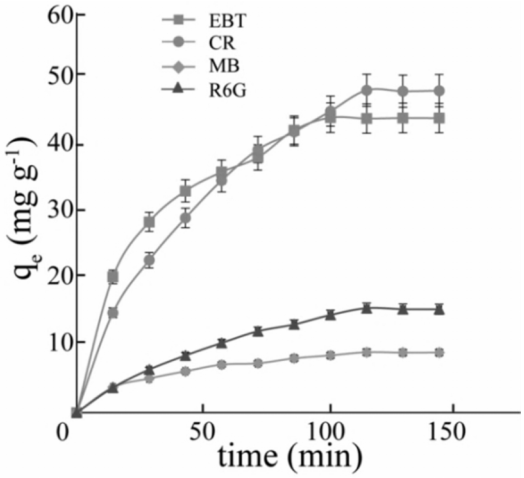

Figure 6.13. Plot for the adsorption efficiency (q_e) with time.

The kinetic data obtained was incorporated into Lagergren first order (Eq. 6.5a) and second order kinetic model (Eq. 6.5b) to deduce the kinetic mechanism for the adsorption.[6.14]

$$\log (q_e - q_t) = \log q_e - (1 / 2.303)\, k_1 t \qquad (6.5a)$$

$$(t / q_t) = (1/ q_e^2 k_2) + (t / q_e) \qquad (6.5b)$$

Where, the q_t and q_e (mg g^{-1}) are total adsorption capacity at time t and at equilibrium respectively. k_1 and k_2 are first and second order rate constant respectively. The calculation results indicate that the adsorption kinetics of EBT, CR, MB and R6G on vaterite microspheres can be well explained by the pseudo-second-order adsorption model with higher correlation coefficients (R^2) and are given in Table 6.4. The values obtained for k_1 and k_2 are also summarized in Table 6.4. Figure 6.14 represents the pseudo-second-order plot for all the dyes.

Table 6.4. Kinetic parameters of the rate of adsorption of the dye on to Vaterite.

	First order kinetics		Second order kinetics		Intra-particle diffusion kinetics		
	k_1 (L min^{-1})	R^2	k_2 (g mg^{-1} min^{-1})	R^2	K_w (mg $g^{-1}min^{-0.5}$)	C(mg g^{-1})	R^2
EBT	0.030	0.924	0.0007	0.992	3.62	7.7	0.986
CR	0.025	0.977	0.002	0.993	4.73	2.8	0.996
MB	0.026	0.966	0.002	0.991	0.74	1.1	0.990
R6G	0.273	0.979	0.0003	0.995	1.69	2.7	0.991

Adsorption onto the surface of the adsorbent is often accompanied by diffusion of the adsorbate from the exterior surface to the pores of adsorbent. To see this effect the kinetic data were also fitted into the intra-particle diffusion model, an empirical model which gives us the information of the steps within the adsorption process. The intra-particle diffusion is described by Eq. (6.5c),[6.15]

$$q_t = K_w t^{1/2} + C \qquad (6.5c)$$

Where K_w is an intra-particle diffusion rate constant and C is the intercept. From the results it was obtained that the intra-particle diffusion model also demonstrated a high R^2 value for all the dyes, (Table 6.4) which indicates that pore diffusion also affects the rate of dye adsorption. However, since the intercept of the line (for the dyes) do not pass through origin suggests that this mechanism does not solely limit the overall adsorption process. The rate-limiting step may be a complex combination of adsorption onto the external surface and intra-particle diffusion working hand in hand.[6.31]

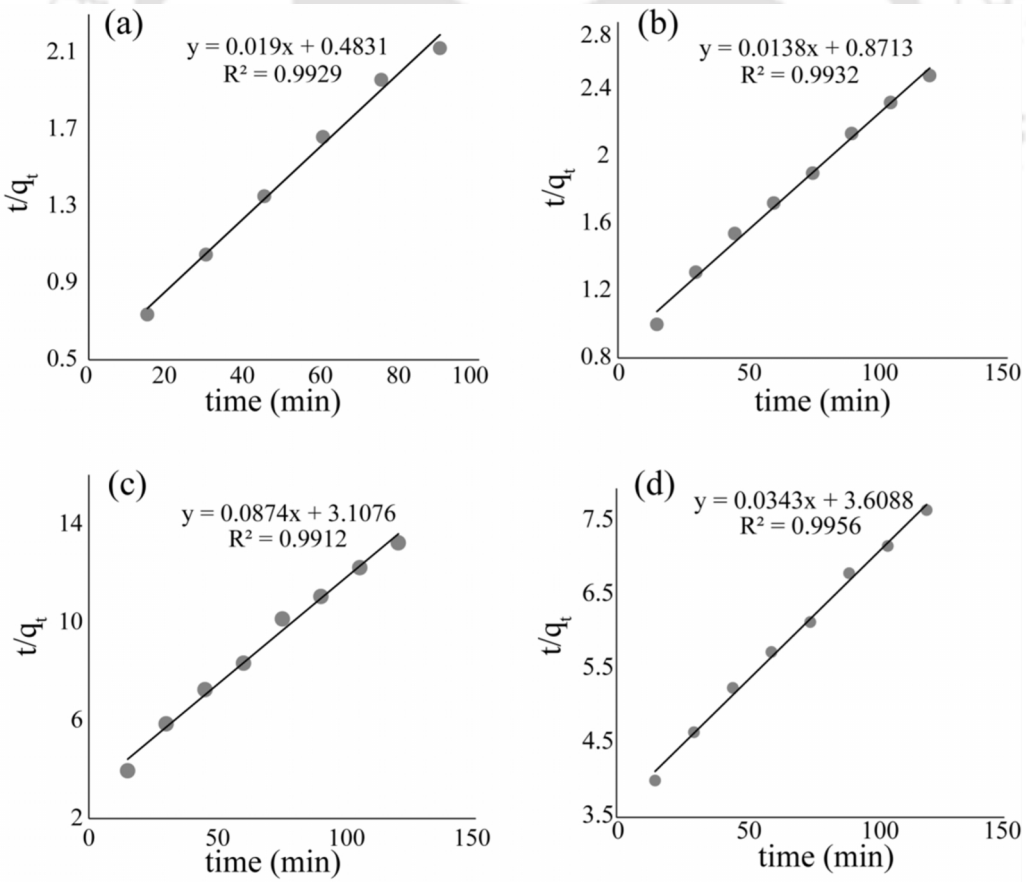

Figure 6.14. Second order kinetics plot of dyes (a) EBT, (b) CR, (c) MB and (d) R6G onto vaterite surface.

6.4.3.3 Adsorption isotherm

For designing a preferred sorption system it is very necessary to know the parameters involved in the adsorbate-adsorbent interaction.[6.32] The adsorption isotherm can throw some light into these requisite parameters. The Langmuir and Freundlich adsorption isotherms were utilized to describe the relationship between the amounts of adsorbed adsorbate and its equilibrium concentration in aqueous solution. The linearized form of Langmuir and Freundlich adsorption isotherms can be expressed according to Eq. (6.6a) and Eq. (6.6b) respectively,[6.16,6.17]

$$C_e/q_e = C_e/Q_m + 1/Q_m b \quad (6.6a)$$

$$\log q_e = \log K_f + (1/n) \log C_e \quad (6.6b)$$

Where, C_e (mg L^{-1}) and q_e (mg g^{-1}) is the equilibrium dye concentration in aqueous and solid phase respectively. Q_m is the maximum monolayer uptake by the adsorbent (mg g^{-1}), and b is the Langmuir binding constant of the adsorption. K_f is the Freundlich's uptake factor and n is the Freundlich constant (index of adsorption intensity or surface heterogeneity) which denotes favorability of the adsorption if the value lies between 1 and 10. The data obtained were analyzed for the best fit in the isotherm models. The results are enlisted in the Table 6.5 with their respective correlation coefficients (R^2). The q_e values were calculated from both the isotherm and the q_e value calculated out from the Langmuir isotherm were found to be proximate to the experimental q_e value. Figure 6.15 shows the adsorption fit for EBT and CR with the experimental and calculated using the Freundlich model. The R^2 value for the Langmuir isotherm was also better compared to the Freundlich isotherm suggesting that the adsorption was monolayer. The plateau formation in the adsorption isotherm curve also indicates this sort of mechanism to occur (Figure 6.4a). The experimental values for the maximum monolayer (Q_m) uptake as obtained from the plateau region were also in well accordance with the calculated values favoring the Langmuir model over the Freundlich model.

Table 6.5. Adsorption isotherm parameters of dyes on Vaterite.

	Langmuir isotherm				Freundlich isotherm		
	Q_m(mg g^{-1})	b (L mg^{-1})	R^2	R_L	K_f(mg g^{-1})	n	R^2
EBT	158.73	0.0063	0.993	0.412	4.03	1.54	0.967
CR	102.04	0.0098	0.999	0.519	6.56	1.94	0.932
MB	27.39	0.0064	0.996	0.597	2.54	1.47	0.968
R6G	31.45	0.0148	0.995	0.443	1.38	1.90	0.942

Another important parameter, a dimensionless constant called "constant separation factor" or "equilibrium parameter", R_L defined as

$$R_L = 1/ (1+ b C_0) \quad (6.6c)$$

where, b is the Langmuir coefficient and C_0 is the initial dye concentration, can give some indication of the feasibility of the adsorption process. For a favourable reaction process, $0< R_L<1$; whereas R=0 for the irreversible case, R=1 for the linear case and R>1 for unfavourable reaction. The values for EBT, CR, MB and R6G were calculated to be 0.412, 0.519, 0.597 and 0.443 respectively which falls well within the favourable regime (Table 6.5).

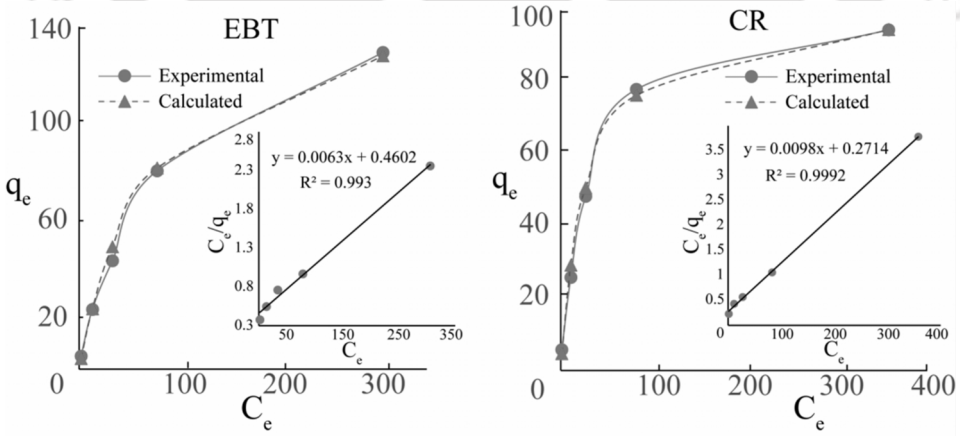

Figure 6.16. Adsorption isotherm plot for (a) EBT and (b) CR onto vaterite, q_e values compared were obtained from Langmuir isotherm and experimental finding; (inset: Langmuir plot for (a) EBT and (b) CR respectively).

6.4.3.4 Effect of temperature and thermodynamics

The extent of adsorption is also dependent on the temperature of the solid–liquid interface. Therefore, we have chosen to study the adsorption at different temperature ranging from 283–313K. Adsorption at different temperature can also give the overview of the favorability of the adsorption system which reveals the thermodynamic aspect for the adsorption. With the rise in temperature the adsorption value was found to increase for all the cases of the dyes. The adsorption values, q_e (mg g^{-1}) for EBT, CR, MB and R6G were 40.51, 47.15, 6.43 and 15.63 at 283K which increased to 46.51, 49.36, 10.96 and 18.45 respectively.

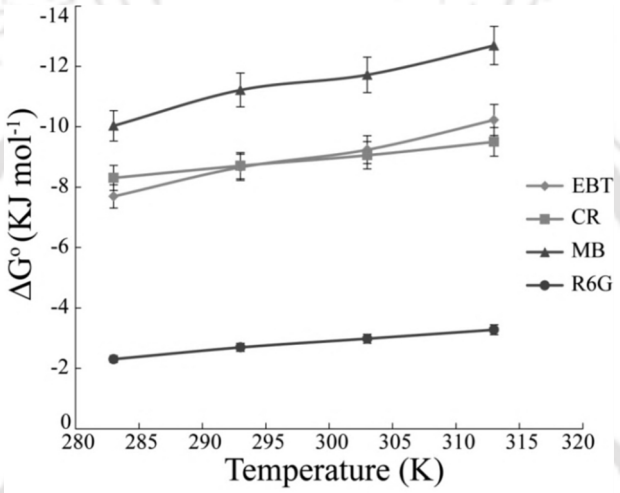

Figure 6.17. Plot for ΔG^o with temperature for the adsorption of the dyes.

To get the details of the thermodynamic parameters we have incorporated the standard Gibbs energy equation which relates the Gibbs free energy change (ΔG^o), enthalpy change (ΔH^o) and entropy change (ΔS^o) by the following,`

$$\Delta G^o = - RT \ln (k_c) \quad (6.7a)$$

Where R is the universal gas constant (8.314 J mol^{-1} K^{-1}) and T is temperature in Kelvin. k_c is the equilibrium stability constant, which was calculated at each temperature using the relation,

$$k_c = C_s/C_e \quad (6.7b)$$

Where, C_s and C_e are the equilibrium concentration on the adsorbent and the aqueous phase respectively.[6.33] The enthalpy ΔH^o and the entropy ΔS^o of adsorption were estimated from the following equation:

$$\Delta G^o = \Delta H^o - T\Delta S^o \quad (6.7c)$$

The combination of Eqs. (4a) and (4c) gives:

$$\ln k_c = -\Delta H^o/RT + \Delta S^o/R \quad (6.7d)$$

The slope and intercept of the plot between ln k_c versus 1/T give the values of ΔH^o and ΔS^o. The (ΔG^o), (ΔH^o) and (ΔS^o) values obtained for EBT, CR, MB and R6G are summarized in Table 3. The negative values for ΔG^o in all the cases at different temperatures (Table 6.6) indicate that the adsorption is thermodynamically feasible and is spontaneous in nature. The increase in ΔG^o values with increase in temperature shows an increase in feasibility of the adsorption at higher temperatures. The ΔH^o of a system gives the information about the endothermic/exothermic nature of the adsorption process and also ascertains the adsorption as physisorption or chemisorption. The typical value for physisorption usually lies below 84 kJ mol^{-1}, whereas for chemisorption bond strengths lie between 84–420 kJ mol^{-1}.[6.34] The values for ΔH^o lie well below 84 kJ mol^{-1} which favors the physisoprtion of the dyes onto vaterite surface. Entropy has been defined as the degree of chaos of a system. The positive value of $\Delta S°$ suggests that some structural changes occur on the adsorbent, and the randomness at the solid/liquid interface in the adsorption system increases with increase in temperature. Figure 6.17 shows the variation of Gibbs free energy change (ΔG^o) with temperature.

Table 6.6. Thermodynamic parameters of dye adsorption onto Vaterite.

	T(K)	**283**	**293**	**303**	**313**
EBT	ΔG^o (K J mol^{-1})	-7.69	-8.65	-9.23	-10.22
	ΔS^o (J mol^{-1} K^{-1})	81.73			
	ΔH^o (K J mol^{-1})	15.40			
CR	ΔG^o (K J mol^{-1})	-8.30	-8.70	-9.05	-9.50
	ΔS^o (J mol^{-1} K^{-1})	39.07			
	ΔH^o (K J mol^{-1})	2.79			
MB	ΔG^o (K J mol^{-1})	-10.03	-11.21	-11.72	-12.68
	ΔS^o (J mol^{-1} K^{-1})	85.03			
	ΔH^o (KJ mol^{-1})	13.92			
R6G	ΔG^o (KJmol^{-1})	-2.30	-2.69	-2.98	-3.27
	ΔS^o (J mol^{-1} K^{-1})	32.18			
	ΔH^o (KJ mol^{-1})	6.77			

6.4.3.5 Desorption

The practical reusability of any adsorbent depends on desorption of the adsorbed materials from the adsorbent surface. To see desorption efficiency of the framboidal vaterite microspheres we have incubated the dye loaded vaterite particles in 50% ethanolic solution and separated by centrifugation. The desorption values were found to be 70%, 67%, 86% and 71% for EBT, CR, MB and R6G respectively (Figure 6.18a). But these values of desorption efficiency are less compared to our earlier study case of Malachite nanoparticles and dye (in chapter 5), where desorption efficiency were greater than ~97% for all the cases. This might be due to the fact that some fraction of the dye might get trapped into the interior of the calcite that has been formed by the transformation of the vaterite during the adsorption process. As a result these trapped dyes were not released from the vaterite entity. Although, these vaterite-dye composites could be further reused and has potential as the raw material of caustic lime making or as a colour additive used in building materials, rubber and plastics industries.[6.35] This adds to another potential benefit of using the vaterite micro-particles for dye removal.

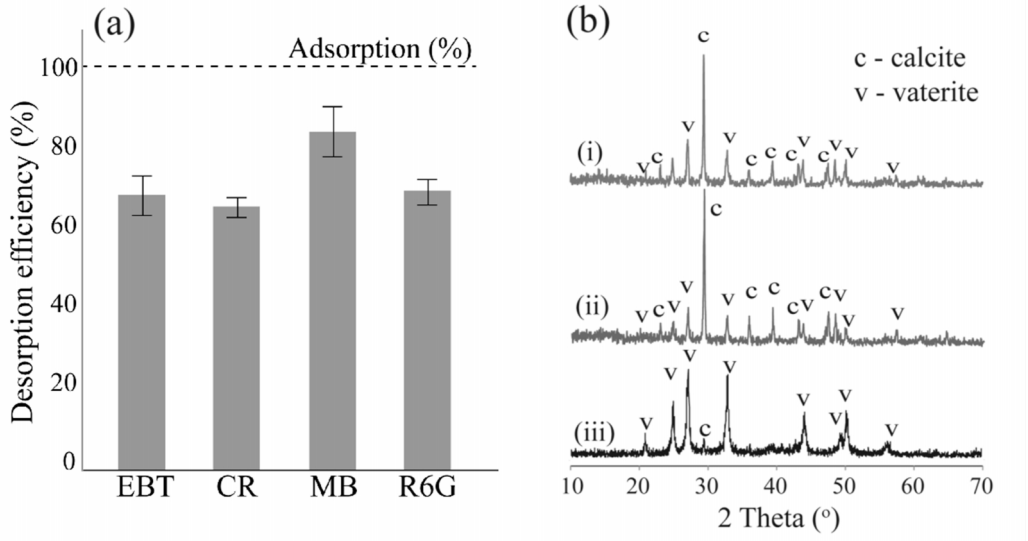

Figure 6.18. (a) Desorption efficiency of the vaterite surface after the adsorption of the dyes. (b) PXRD spectra of vaterite after desorption of dyes from the vaterite surface.

The dye-vaterite composite after desorption was subjected to PXRD analysis to see any change in the properties of adsorbent during the adsorption process. Figure 6.18b represents the PXRD spectra taken after desorption of the vaterite particles for EBT and

CR. The PXRD spectra for MB and R6G are given in the supporting section (Appendix, Figure A6.5). A subtle change in the PXRD peak was seen in the spectra for all the cases. Characteristic calcite peaks were found to be present in the PXRD spectra. The FTIR spectra also support the formation of calcite with the emergence of calcite peak at 712 cm^{-1} for the cases (Appendix, Figure A6.6). The presence of the calcite peak in the dye-vaterite composite could be justified by the fact that a small fraction of vaterite has been transformed to calcite during the adsorption process. Although these vaterite were shown to be stable in solution up to ~4 days, but the interaction forces leading to the adsorption might be aiding this transformation of vaterite to calcite. The color of the dye-vaterite composites are given in the Figure 6.19, which also supports the incorporation of the dyes onto the vaterite surface.

Figure 6.19. Image of the dye loaded vaterite particles, (a) EBT loaded vaterite, (b) CR loaded vaterite, (c) MB loaded vaterite and (d) R6G loaded vaterite.

6.4.4 Summary

In summary, vaterite microspheres are found to be very effective in the removal of dyes from aqueous solution. Vaterite, a relatively unstable polymorph of $CaCO_3$ and having high surface area was found to be efficient container for the loading of anionic dyes compared to the cationic dyes. EBT, CR was adsorbed more compared to the cationic dyes such as MB and R6G. The adsorption profile was highly pH dependent and was

sought to be electrostatic in nature. The positive surface of the vaterite ($pH < PZC_{vaterite}$) and the negative functional groups of the EBT and CR ($pH > pK_a$) facilitates the requisite electrostatic interaction that leads to the increased adsorption of these dyes onto vaterite surface. Whereas the electrostatic repulsion of the cationic MB and R6G ($pH < pK_a$) with the positive ($pH < PZC_{vaterite}$) surface justifies the observed lower value of adsorption onto vaterite surface. The adsorption followed the second order kinetics for all the dyes with simultaneous occurrence of the intra particle diffusion of the dyes. Langmuir isotherm was preferably more matched with the obtained data for all the cases of the dye. The adsorption was spontaneous in nature. The desorption efficiency and the practical reusability of the vaterite-dye composite was addressed efficiently. These findings together suggest the potential applicability of vaterite for waste water treatment.

Reference

[6.1] K. Naka, Y. Tanaka, Y. Chujo, Langmuir, 18 (2002) 3655-3658.

[6.2] (a) L. Zhang, L. H. Yue, F. Wang, Q. Wang, J. Phys. Chem. B, 112 (2008) 10668-10674. (b) Z. Nan, B. Yan, X. Wang, R. Guo, W. Hou, Cryst. Growth Des. 8 (2008) 4026-4030. (c) S. F. Chen, S. H. Yu, J. J. F. Li, Y. Liu, Chem. Mater. 18 (2006) 115-122. (d) Q. Shen, L. Wang, X. Li, F. Liu, Cryst. Growth Des. 8 (2008) 3560-3565. (e) Q. Shen, L. Wang, Y. Huang, J. Sun, H. Wang, Y. Zhou, D. Wang, J. Phys. Chem. B, 110 (2006) 23148-23153. (f) Z. Nan, X. Chen, Q. Yang, X. Wang, Z. Shi, W. Hou, J. Colloid Interface Sci. 325 (2008) 331-336.

[6.3] J. Yu, X. Zhao, B. Cheng, Q. Zhang, J. Solid State Chem. 178 (2005) 861-867.

[6.4] H. Cölfen, M. Antonietti, Langmuir, 14 (1998) 582-589.

[6.5] R. Vogel, M. Persson, C. Feng, S. J. Parkin, T. A. Nieminen, B. Wood, N. R. Heckenberg, H. Rubinsztein-Dunlop, Langmuir, 25 (2009) 11672-11679.

[6.6] R. J. Qi, Y. J. Zhu, J. Phys. Chem. B, 110 (2006) 8302-8306.

[6.7] D. Walsh, B. Lebeau, S. Mann, AdV. Mater. 11 (1999) 324-328.

[6.8] F. Manoli, E. Dalas, J. Cryst. Growth, 222 (2001) 293-297.

[6.9] P. Malkaj, E. Dalas, Cryst. Growth Des. 4 (2004) 721-723.

[6.10] Q. Shen, H. Wei, Y. Zhou, Y. P. Huang, H. R. Yang, D. J. Wang, D. F. Xu, J. Phys. Chem. B, 110 (2006) 2994-3000.

[6.11] J. Ahmed, Menaka, A. K. Ganguli, Cryst. Eng. Comm. 11 (2009) 927-932.

[6.12] (a) A. Agrawal, C. Pal, K. K. Sahu, J. Hazard. Mater. 159 (2008) 458-464. (b) A. I. Zouboulis, K. A. Kydros, K. A. Matis, Sep. Sci. Technol. 28 (1993) 2449-2463.

[6.13] V. Gómez, M. S. Larrechi, M. P. Callao, Chemosphere, 69 (2007) 1151-1158.

[6.14] (a) S. Lagergren, Handlingar, 24 (1898) 1-39. (b) Y. S. Ho, G. McKay, Process Biochem. 34 (1999) 451-465.

[6.15] W. J. Weber, J. C. Morris, J. Sanit. Eng. Div. Am. Soc. Civ. Eng, 89 (1963) 31-60.

[6.16] I. Langmuir, J. Am. Chem. Soc. 38 (1916) 2221-2295.

[6.17] H. M. F. Freundlich, Z. Phys. Chem. 57 (1906) 385-470.

[6.18] S. Chen, Q. Yue, B. Gao, X. Xu, J. Colloid Interface Sci. 349 (2010) 256-264.

[6.19] N. Barka, M. Abdennouri, M. E. Makhfouk, J. Taiwan Inst. Chem. E, 42 (2011) 320-326.

[6.20] G. McKay, AIChE J. 30 (1984) 692-697.

[6.21] M. Doğan, M. Alkan, Y. Onganer, Water Air Soil Pollut. 120 (2000) 229-248.

[6.22] N. Barka, A. Assabbane, A. Nounah, L. Laanab, Y. Aît-Ichou, Desalination, 235 (2009) 264-275.

[6.23] N. Barka, S. Qourzal, A. Assabbane, A. Nounah, Y. Aît-Ichou, J. Environ. Sci. 20 (2008) 1268-1272.

[6.24] D. V. Bavykin, K. E. Redmond, B. P. Nias, A. N. Kulak, F. C. Walsh, Aust. J. Chem. 63 (2010) 270-275.

[6.25] H. Chen, J. Zhao, Adsorption 15 (2009) 381-389.

[6.26] H. El Boujaady, A. El Rhilassi, M. Bennani-Ziatni, R. El Hamri, A. Taitai, J.L. Lacout, Desalination, 275 (2011) 10-16.

[6.27] B. Saha, S. Das, J. Saikia, G. Das, J. Phys. Chem. C, 115 (2011) 8024-8033.

[6.28] A. Roy, S. Chakraborty, S. P. Kundu, B. Adhikari, S. B. Majumder, Ind. Eng. Chem. Res. 51 (2012) 12095-12106.

[6.29] V. M. Vučurović, R. N. Razmovski, M. N. Tekić, J. Taiwan Inst. Chem. E, 43 (2012) 108-111.

[6.30] S.A. El-Safty, A. Shahat, Md. R. Awual, J. Colloid Interface Sci. 359 (2011) 9-18.

[6.31] M. D. G. de Luna, E. D. Flores, D. A. D. Genuino, C. M. Futalan, M. W. Wan, J. Taiwan Inst. Chem. E, 44 (2013) 646-653.

[6.32] J. He, S. Hong, L. Zhang, F. Gan, Y. S. Ho, Fresen. Environ. Bull. 19 (2010) 2651-2656.

[6.33] H. Y Zhu, R. Jiang, Y. Q. Fu, J. H. Jiang, L. Xiao, G. M. Zeng, Appl. Surf. Sci. 258 (2011) 1337-1344.

[6.34] C. Y. Kuo, C. H. Wu, J. Y. Wu, J. Colloid Interface Sci. 327 (2008) 308-315.

[6.35] V. M. Vučurović, R. N. Razmovski, M. N. Tekić, J. Taiwan Inst. Chem. E, 43 (2012) 108-111.

Appendix

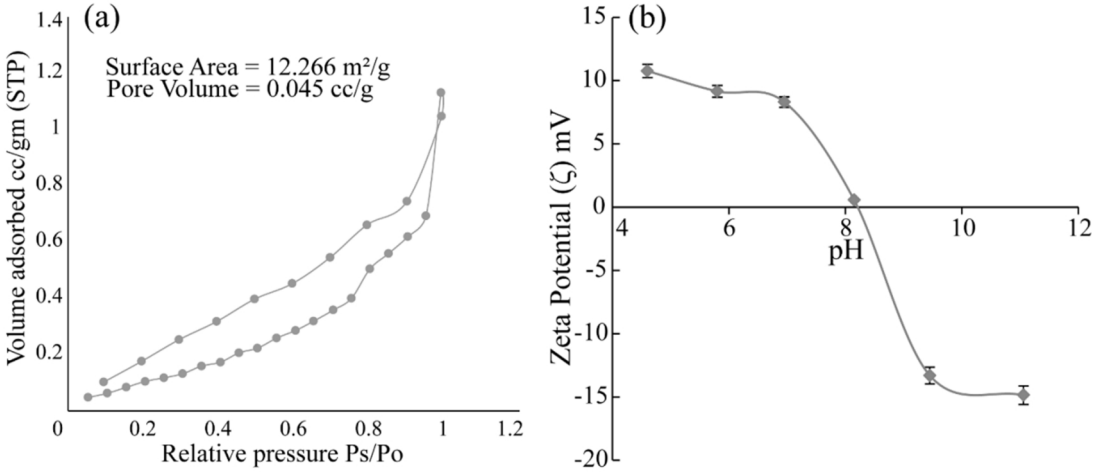

Figure A6.1. (a) BET surface area plot and (b) ζ-potential plot of vaterite.

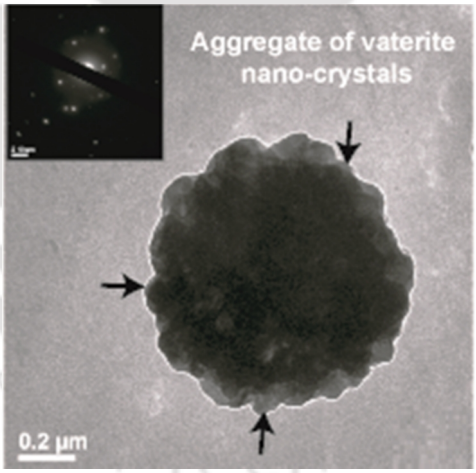

Figure A6.2. TEM image showing nano vaterite aggregation to form large vaterite microsphere. (inset): SAED of the corresponding particle

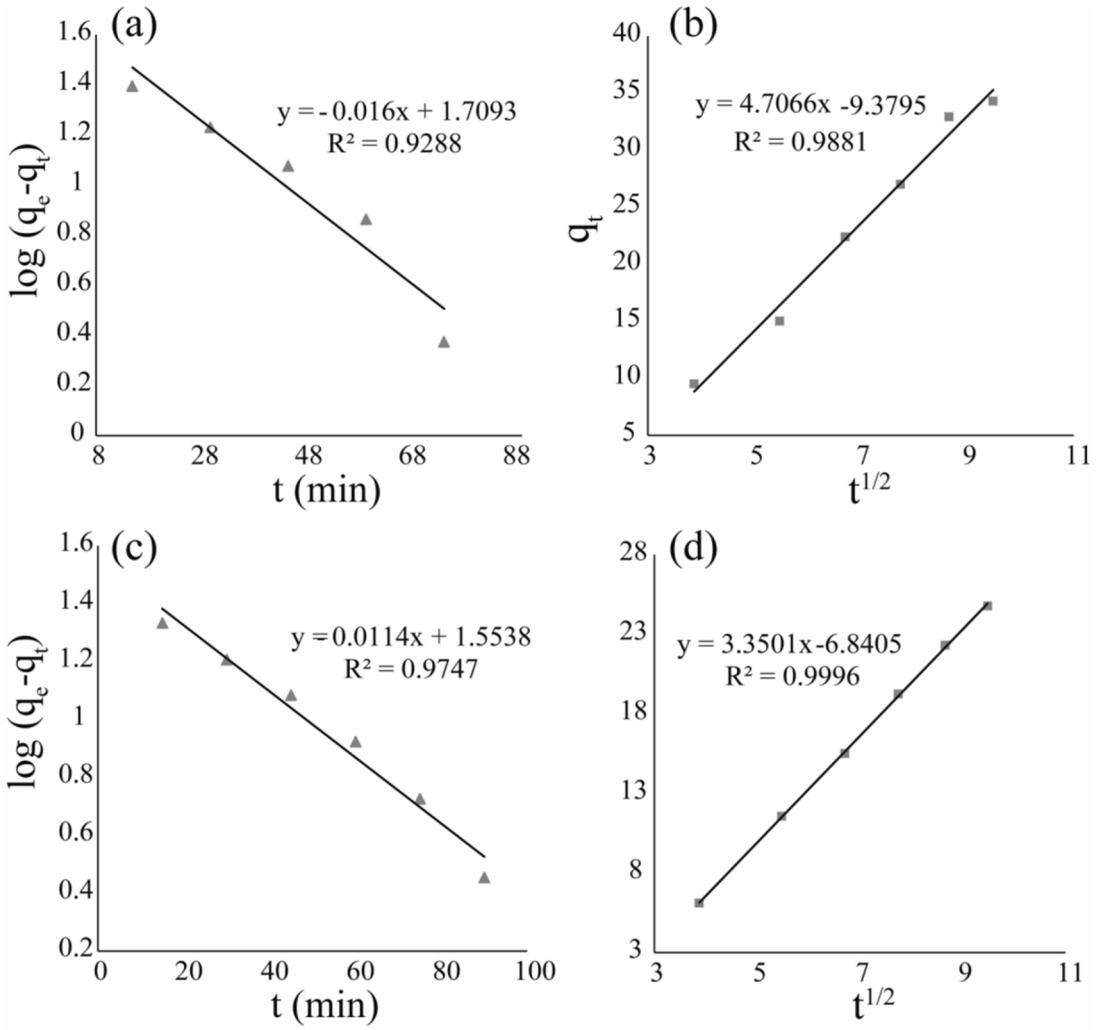

Figure A6.3. First order kinetics plot of (a) arsenate and (c) chromate; Intra-particle diffusion plot (b) aresenate and (d) chromate adsorption onto vaterite particles.

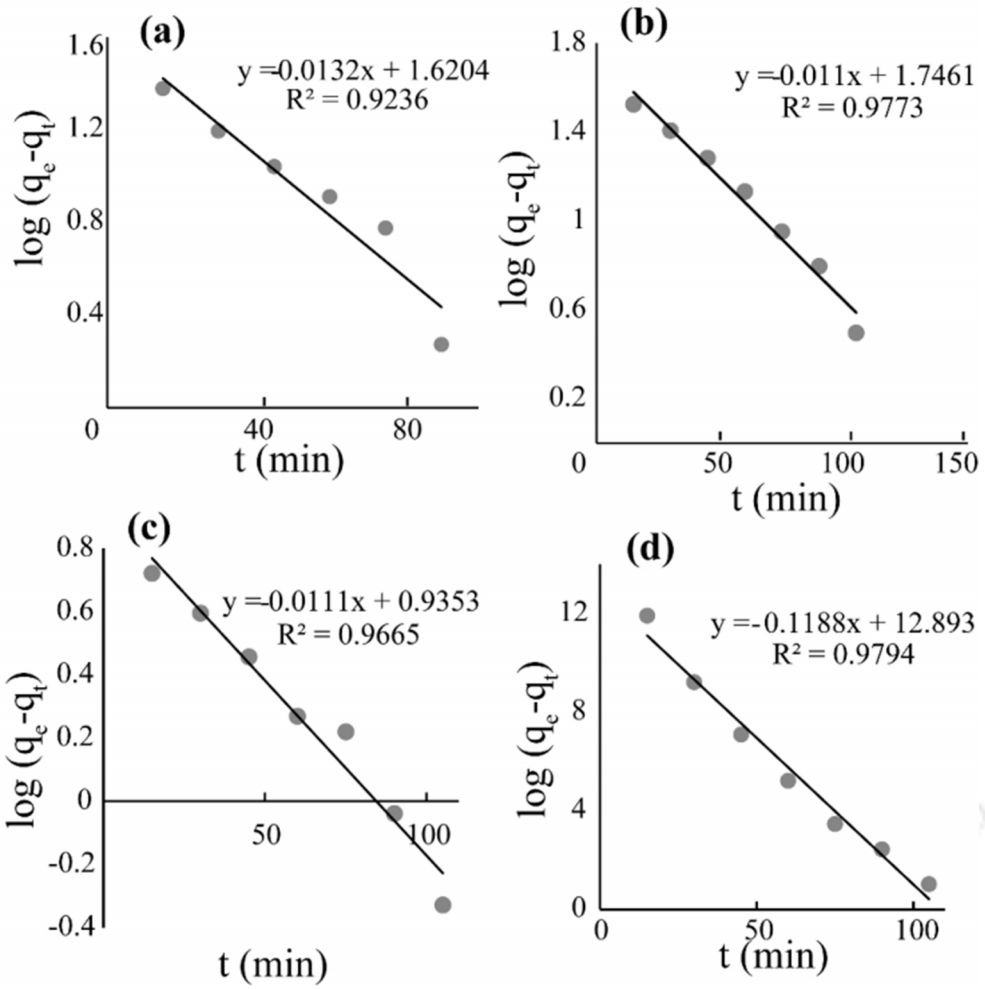

Figure A6.4. First order kinetic spectra of the adsorption of dyes (a) EBT, (b) CR, (c) MB and (d) R6G, on to vaterite.

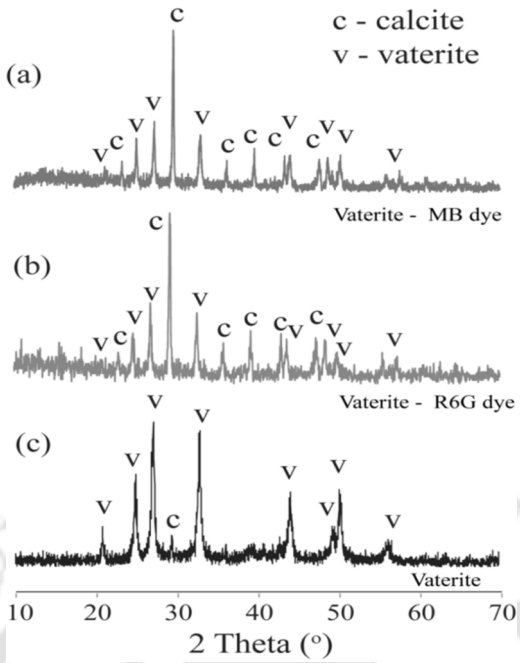

Figure A6.5. PXRD spectra of vaterite after desorption of dyes from the vaterite surface.

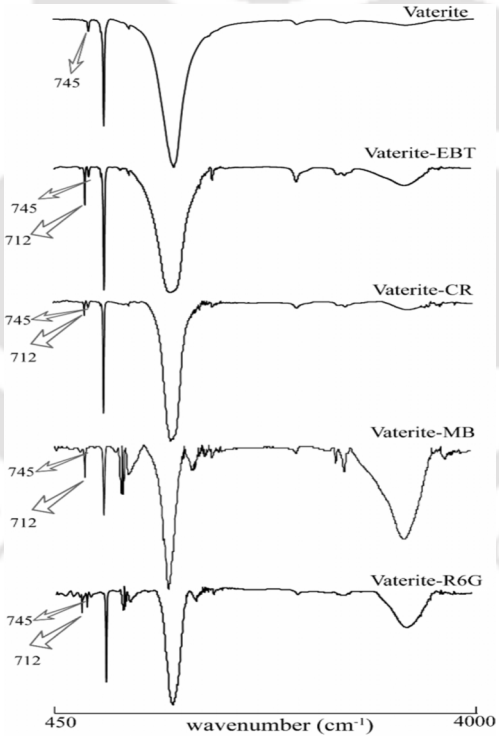

Figure A6.6. FTIR spectra showing the emergence of calcite peak at 712 cm^{-1} after adsorption of various dyes onto vaterite.

Conclusion and Future Direction

In conclusion, this thesis represents the interaction study of proteins and pollutants onto various inorganic surfaces and their dependence on the surface properties. Different inorganic mineral based micro-to-nano structured materials have been prepared and used for these interaction studies. Of the studied inorganic surfaces, different surface properties were established with different inorganic materials which in turn interact with different proteins and pollutants. The 'hard' and 'soft' nature of the inorganic surface alongside the 'acidic' and 'basic' nature controls the fate of interaction of these inorganic surfaces with other entity. Nevertheless, other important regulating parameter such as pH, temperature, concentration etc. also governs the fate of the adsorption. These were the major findings put forward in the thesis.

The basic hard surface of ZnO interacts with the protein BLG with possible electrostatic interaction with no significant changes in the protein secondary element. The adsorption was found to be maximized at near the IEP of the protein. But the observation with the ZnS, which is a soft and acidic surface, was evidently different. ZnS interacts differently with the proteins (BSA and BLG). The negative surface of ZnS also facilitated the adsorption of negatively charged BSA and BLG onto its surface. The secondary structure of BSA was altered to accommodate this adsorption whereas the rigid BLG was more stable whilst the probable interaction took place with the oppositely charged local regimes (patches). This also supported the assumption of conformational flexibility and conformational rigidity of BSA and BLG respectively. Furthermore, the interaction and removal studies of pollutants (both inorganic and organic) from solution using inorganic mineral based surface were also found to be dependent on various factors. The basic hard surface of malachite was found to be efficient for the removal of anionic pollutants and preferential removal of Flu compared to RB and R6G. On the other hand, the more basic surface of the vaterite could also be efficiently used for the interaction/removal of arsenate and chromate from solution. The advantage of the basic surface of the vaterite was well utilized for selective removal of anionic dyes (EBT and CR) over cationic dyes (MB and R6G).

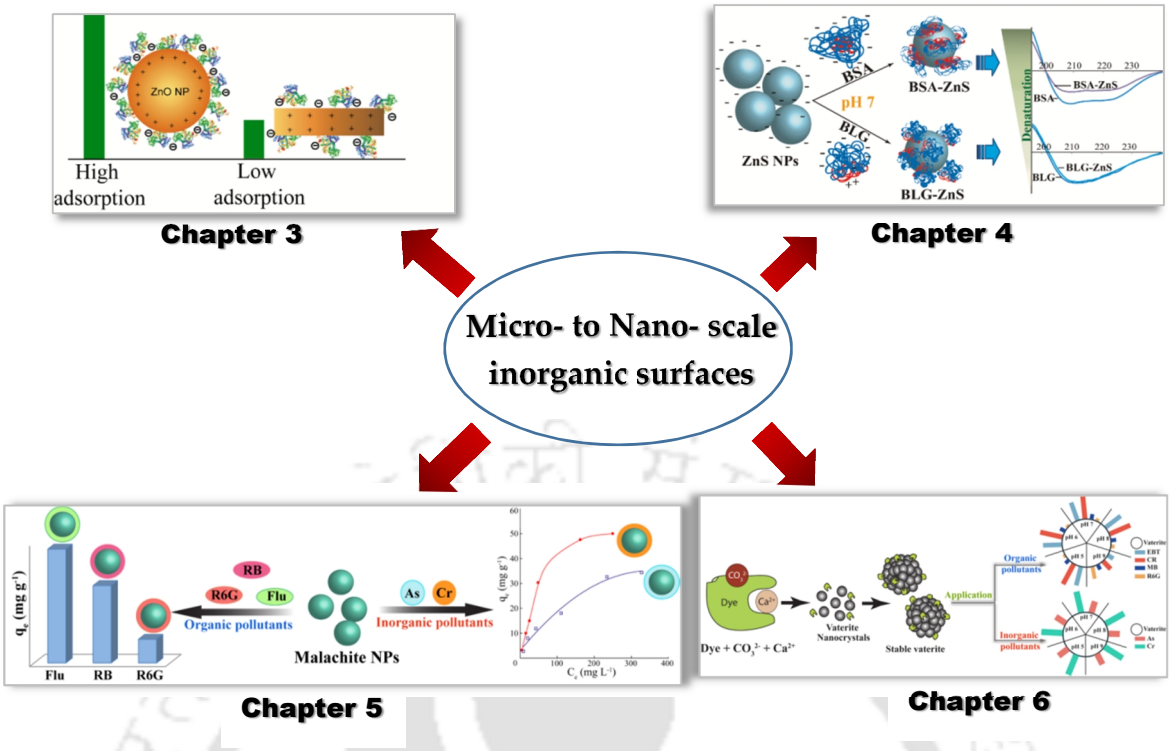

Scheme: A general outline of the present work of this thesis.

Overall, the work reported in this thesis, gives an in-sight to the interaction of protein and pollutants onto inorganic surfaces. Surface dependence of such interaction and the suitable parameters to control such interactions at the interface are presented. These findings could help to augment the better understanding of protein-nano construct for practical usability. Furthermore, the potential applicability of these inorganic surfaces for waste water remediation (ionic pollutants or dyes) is substantial. A plenty of information of surface specific interaction, and various parameters controlling such interaction at the molecular level could be gathered which could be fabricated to gain more control over such interactions.

List of publication

[1] **Jiban Saikia,** Bedabrata Saha, Gopal Das, Efficient removal of chromate and arsenate from individual and mixed system by malachite nanoparticles, *Journal of Hazardous Materials* 2011, Vol-186, Pg-575-582.

[2] **Jiban Saikia,** Bedabrata Saha, Gopal Das, Controlling the morphological evolution of ZnO NPs from single precursor source and its application for beta-lactoglobulin adsorption, *Journal of Nanoparticle Research*, 2012, Vol-14, Pg-1226-1239.

[3] **Jiban Saikia,** Bedabrata Saha, Gopal Das, Morphosynthesis of framboidal stable vaterite using a salicylic acid-aniline dye as an additive. *RSC Advances*, 2012, Vol-2, Pg-10015-10019.

[4] **Jiban Saikia,** Yeasin Sikdar, Bedabrata Saha, Gopal Das, Malachite nanoparticle: A potent surface for the adsorption of xanthene dyes, *Journal of Environmental Chemical Engineering*, 2013, Vol-1, Pg-1166–1173.

[5] **Jiban Saikia,** Bedabrata Saha, Gopal Das, Interpreting the adsorption of serum albumin and lactoglobulin onto ZnS nanopaticles: Effect of conformational rigidity of the proteins, *Journal of Colloid and Interface Science*, 2014, Vol-416, 235–242.

[6] Bedabrata Saha, Sourav Das, **Jiban Saikia**, Gopal Das, Preferential and enhanced adsorption of different dyes on iron oxide nanoparticles: A comparative study, *The Journal of Physical Chemistry C,* 2011, Vol-115, Pg-8024-8033.

[7] Bedabrata Saha, **Jiban Saikia,** Gopal Das, Tuning the selective interaction of lysozyme and serum albumin on a carboxylate modified surface, *RSC Advances*, 2013, Vol-3, Pg-7867-7879.

[8] Manab Dev Adhikari, Sandipan Mukherjee, **Jiban Saikia**, Gopal Das, Aiyagari Ramesh, Magnetic nanoparticles for selective capture and purification of an antimicrobial peptide secreted by food-grade lactic acid bacteria, *Journal of Material Chemistry B,* (2014), Vol-2, Pg-1432-1438

[9] **Jiban Saikia**, Gopal Das, Framboidal vaterite for efficient removal of anionic dyes over cationic dyes, *Journal of Environmental Chemical Engineering*, 2014, Vol-2, Pg-1165-1173.

[10] **Jiban Saikia**, Gopal Das, Arsenate and chromate removal using framboidal vaterite micro-spheres. (*Manuscript under Preparation*).

[11] Bedabrata Saha, **Jiban Saikia,** Saswati Chakraborty, Gopal Das, Influence of surface crowding on enzymatic activity of trypsin immobilized on ultrafine CuS nanoparticles, (*Manuscript under Submission*).